University of Nevada, Reno

Plasma flow control in the ablation and implosion phases in nested cylindrical and star wire array Z-pinches

A dissertation submitted in partial fulfillment of the

requirements for the degree of Doctor of Philosophy in

Physics

by

Daniel Papp

Dr. Vladimir Ivanov/Dissertation Advisor

August 2013

THE GRADUATE SCHOOL

We recommend that the dissertation
prepared under our supervision by

DANIEL PAPP

entitled

Plasma flow control in the ablation and implosion phases in nested cylindrical and star wire array Z-pinches

be accepted in partial fulfillment of the
requirements for the degree of

DOCTOR OF PHILOSOPHY

Vladimir V. Ivanov, Advisor

Radu Presura, Committee Member

Roberto C. Mancini, Committee Member

Indira Chatterjee, Committee Member

Normand Leblanc, Graduate School Representative

Marsha H. Read, Ph. D., Dean, Graduate School

August, 2013

ABSTRACT

Wire array Z-pinches are the most powerful laboratory x-ray sources, and the optimization of the x-ray radiation output requires the understanding of diverse phenomena. During the wire array implosion in such arrays, the **j**×**B** forces ablate plasma from the wires to the center, before the whole array mass implodes. We studied the ablation and implosion dynamics in nested cylindrical and star wire array Z-pinches. The two implosion modes of nested arrays were simulated by Al star wire arrays with "gates". Arrays with regular-length gate wires imploded in the "nontransparent regime". Arrays with long, higher-Z gate wires imploded in the "transparent" regime. A two-frame end-on UV laser probing diagnostics was developed for the Zebra generator.

Modified nested cylindrical arrays, called closely spaced arrays, were designed to implode without a precursor. Low-wire number arrays imploded accordingly. Precursor plasma was observed in higher wire-number arrays, despite outward **j**×**B** forces on the inner wires. The Al K-shell yield was highest for low wire-number nested arrays, which also imploded earlier. The presence of precursor in star wire arrays was determined by the direction of the **j**×**B** forces. Star wire array pairs were designed such that precursor and non-precursor arrays would have minimal differences. The presence of precursor decreased the x-ray yield parameters by 3-15%. Plasma flow control was achieved in these loads by varying the array configuration.

Radiative properties of multicomponent Z-pinches and laser produced plasmas were studied. When high-Z element (W, Au) was mixed with Al plasma in a wire array, a

decrease of the electron temperature was observed. The cooling effect was not present in laser-produced Al-Au plasmas, which may be explained by different heating mechanisms.

ACKNOWLEDGEMENT

First I need to thank my advisor, Dr. Vladimir V. Ivanov, for providing guidance and example for my research. I would also thank the members of my Dissertation Committee, Dr. Indira Chatterjee, Dr. Normand Leblanc, Dr. Roberto C. Mancini, and Dr. Radu Presura, for revising my dissertation and providing valuable support and advice. Last but not least, I also thank Dr. Aaron Covington, who recruited me from the Department of Physics at University of Nevada, Reno.

I would like to thank my fellow student colleagues, Dr. Abdelmoulah Haboub, Sara D. Altemara, Austin A. Anderson, and Bjorn R. Talbot for their helpful comments, and their contributions to collecting and analyzing the data during experiments. I also need to thank the help of the Nevada Terawatt Facility staff for support during the experiments, especially Alexey Astanovitskiy for designing and building experimental hardware.

TABLE OF CONTENTS

LIST OF TABLES

LIST OF FIGURES

1. INTRODUCTION

Z-pinches are self-constricted plasma configurations, that is, the electric current flowing in the axial ('Z') direction in the plasma provides the confinement. The current creates an azimuthal magnetic field, and resulting $\mathbf{j}\times\mathbf{B}$ forces compress the plasma, which is referred to as the pinch effect. Z-pinches are a candidate driver for an inertial confinement thermonuclear fusion (ICF) power-source, and are also the most powerful and intense laboratory x-ray sources.

While there were some similar experiments earlier [Ryutov2000, Liberman1999, Haines2011], the first main result about Z-pinches was the Bennett equilibrium [Bennett1934], describing the balance of magnetic and kinetic pressures in "magnetically self-focusing streams". In 1950s, neutron production was observed in Z-pinches, but later that was proved to be of non-thermal origin, reducing the scientific interest in the field [Haines2011]. In the 1970s, rapid improvements in pulsed-power generator technology, allowed voltages of several MV and MA-scale currents, revived scientific research in the area. New configurations, like the gas-puff and fiber pinch were invented. In the fiber (or single wire) Z-pinch, a fiber is placed between the electrodes. The fiber load can be conductor, plastic or even cryogenic deuterium ice. In the gas puff Z-pinch, the current is driven through an annular gas between two electrodes.

The behavior of Z-pinches is strongly influenced by several types of plasma instabilities that are present throughout the implosion process.

Wire array Z-pinches are the most intense laboratory x-ray sources. Wire array loads at the Z accelerator at Sandia National Lab produced x-ray pulses over 2MJ energy and 280TW power at 20MA drive current, with a very high 15% wallplug-to-x-ray efficiency [Sanford1996, Deeney1998]. Large-diameter nested cylindrical arrays were developed as K-shell x-ray sources [Jones2008, Coverdale2010]. Using wires of mid-atomic elements (Mg, Al, Ti, Fe, Cu wires and Ar gas puff) the pinch can produce line and free-bound recombination radiation in the 1-9keV range depending on the plasma components, with a total radiated energy of 350kJ down to 20kJ, at a nominal 20MA drive current. Further optimization of wire arrays for x-ray radiation would allow reaching higher x-ray yields using existing facilities.

This lead to the proposals of using Z-pinches for indirect drive fusion scheme, where the x-rays generated would heat up the fusion fuel [Cuneo2001]. Such a scheme would require 60MA drive current. While direct-drive fusion scheme involving wire array or fiber z-pinches would be advantageous due to the high energy conversion efficiency, such schemes are unfeasible due to the chaotic nature of the pinch.

The more recent MagLIF direct-drive concept implodes a cylindrical Be capsule, which compresses a pre-heated and pre-magnetized DT fuel mixture [Slutz2010]. The latter scheme may allow reaching scientific break-even on the Z accelerator.

1.1. Wire array Z-pinches

In a wire array Z-pinch, thin metal wires of 4-25 μm diameters are stretched between electrodes that are 1-2 cm from each other. The linear mass of these loads is usually in

the 20 µg/cm to mg/cm range. Wire array loads are classified by the configuration of the wires. Figure 1 shows different wire array configurations. The most common and most studied configuration is the simple cylindrical array [fig. 1(a)]. Nested cylindrical arrays [fig.1(b)] produce short, high-power x-ray pulses. Star-like arrays are multi-nested wire arrays with wires arranged in reduced number of rays [fig.1(c),(d),(e)]. Planar ('linear') and multi-planar wire arrays produced the highest x-ray energies on the ZEBRA

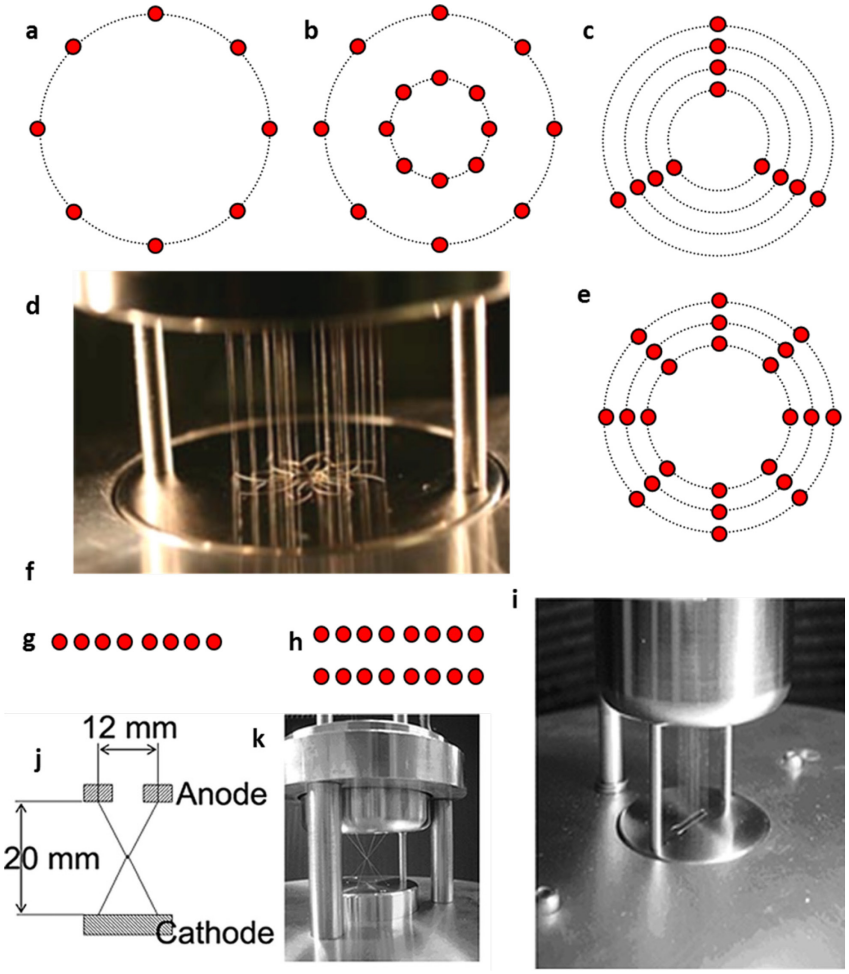

Figure 1. Schematic wire array configurations. 8-wire (regular) cylindrical array (a); 16-wire nested cylindrical array (b); 3-ray 12-wire star array (c); photo (d) and schematic configuration (e) of triple-nested 8-ray 24-wire star array (d); planar (linear) array (g); double planar array (h) and photo (i), x-pinch(j,k). Images (I,j,k) are taken from [Kantsyrev2006]

generator [fig.1(h),(j)]. Conical [Ampleford2007], radial wire arrays [Lebedev2005a] and radial foils [Gourdain2010] can produce axial plasma jets, allowing "laboratory astrophysics" experiments. While not strictly considered a wire array z-pinch, an x-pinch [fig 1(j),(k)] is a similar array. Two or more wires cross at the same point, and this crossing point very high (over 1keV) electron temperatures can be reached in near-solid density plasma, even in sub-1MA generators [Pikuz2004].

1.2. Basic stability criteria

1.2.1. Bennett equation

The Bennett relation [Bennett1934] describes the radial pressure balance of an axial current distribution in a plasma column – the magnetic pressure is balanced by the kinetic pressure. The kinetic pressure can be expressed as

$$p_{kin} = n_i e(T_i + ZT_e), \tag{1-1}$$

where the ion and electron temperatures T_i and T_e are expressed in eV, and Z is the average ionization of the plasma. The magnetic pressure for a linear conductor can be written as

$$p_{mag} = \frac{1}{2\mu_0} B^2 = \frac{\mu_0}{8\pi^2}\frac{I^2}{r^2}. \tag{1-2}$$

Substituting in the linear plasma density $N_i = n_i \pi r^2$, equating eqns. (1-1),(1-2) and rearranging gives

$$8\pi N_i e(T_i + ZT_e) = \mu_0 I^2, \tag{1-3}$$

i.e. the average pressure in the pinch can be calculated knowing only the linear density of the pinch and the total current. As T_e can be known from spectroscopy, T_i can also be determined. In Z-pinches ion temperatures can be several times higher than electron temperatures as the kinetic energy is mostly carried by the ions, and it is thermalized first within the species.

1.2.2. Pease-Braginskii current

An ideal Z-pinch pressure equilibrium has a critical current value, where the Brehmstrahlung losses and the ohmic (Spitzer) heating balance, referred as the Pease-Braginskii current [Pease1957]. In case of a parabolic density profile and uniform current, the critical current is $I_{PB} = 0.433\ (ln\ \Lambda)^{1/2}$ MA, where $ln\ \Lambda$ stands for the Coulomb logarithm. As $ln\ \Lambda \sim 5 - 10$ for typical Z-pinch plasmas, the critical current is in the I_{PB} ~1-1.5 MA range. If the current is above this limit, 0D calculations predict a radiative collapse of the plasma column [Haines2011], i.e. the pinch radius would drop and the density would increase by several magnitudes. Such collapse, however, is prevented, by the conversion of kinetic energy to ion thermal energy, viscous dissipation and Joule heating [Ryutov2000, Haines2011].

1.3. 0-D models of implosion

1.3.1. Thin shell

A cylindrical wire array can be approximated as a thin, uniform annular plasma shell, leading to a zero-dimensional (0D) approximation [Ryutov]. The magnetic field of a

cylindrical wire array, with N wires of uniform spacing, at the position of a (removed) wire, can be summed up vectorially and simplified to get the equation

$$B_\theta = -\frac{\mu_0}{4\pi}\frac{N-1}{N}\frac{I}{r} \quad . \tag{1-4}$$

Here the term with the wire number goes to unity as the wire number increases. With this, the equation of motion for the plasma shell of linear mass $\hat{m}$ can be written as

$$\frac{\hat{m}}{2\pi r}\ddot{r} = -\frac{\mu_0 I^2(t)}{8\pi^2 r^2} \quad . \tag{1-5}$$

With the introduction of dimensionless variables, the equation can be reduced to contain only a single scaling parameter:

$$\rho\ddot{\rho} = -\Pi J^2 \quad . \tag{1-6}$$

With

$$\Pi = \frac{\mu_0 I_{max}^2 t_0^2}{4\pi\hat{m}r_0^2}, \tag{1-7}$$

where $\rho = r/r_0$, $\tau = t/t_0$, $J = I/I_{max}$, t_0 is the current rise-time, I_{max} is the maximum current, and r_0 is the initial array radius. Note the quadratic dependence on current, radius and implosion time. For an array of double radius, the mass must be cut to one-fourth to implode at the same time. Furthermore, as the current is time-dependent, the equation of motion must be solved numerically for a pulse shape $I(t)$, either given or calculated from

a circuit equation [Katzenstein1981]. The rising current for pulsed-power generators can be approximated as a $\sin^2$ waveform:

$$I = I_{max}\sin^2\left(\frac{\pi t}{2t_0}\right)^2. \tag{1-8}$$

A series solution for such waveform can also be derived [Haines2011]. In the first order of the scaling parameter Π, at the start of the implosion, the radial change can be rewritten as

$$\frac{r - r_0}{r_0} = \frac{\pi^4 \Pi}{480} \cdot \left(\frac{t}{t_0}\right)^6 , \tag{1-9}$$

giving the same results as substituting (eqn. 1-8) into (eqn. 1-5) in the r = 0 limit. This equation shows that the implosion of the shell starts slowly. If the implosion is timed to happen at t_0, at $0.66t_0$ the pinch radius is decreased only by 10%. Solving the equation of motion numerically so that the implosion happen at t_0 (ρ=0 at t/t_0 = 1), gives the value for the scaling parameter Π=5.1. For 1MA maximum current at 100ns implosion time, a 12mm diameter array would have a mass of 55μg/cm. While this equation does not describe real implosions well, it still can be used to estimate the implosion time of a Z-pinch load.

The kinetic energy (per unit length) W_{kin} at time t^* of the load can be found from integrating the equation of motion (eqn. 1-5), giving

$$W_{kin} = \frac{\mu}{4\pi}\int_0^{t^*} \frac{dI^2}{dt} ln\left(\frac{r}{r_{min}}\right) dt = \frac{a}{2}\frac{\mu I^2(t^*)}{4\pi} ln\, C, \tag{1-10}$$

where $C = r_0/r_{min}$ is the convergence ratio and a is a generator-specific parameter dependent on the current pulse shape, $a \sim 0.6$ for most generators and $a = 0.68$ for ZEBRA [Ivanov2009]. This kinetic energy would be converted into the radiation of the pinch. To maximize radiation, the maximum convergence ratio should be high, and coincident with the current maximum.

1.3.2. Snowplow models

The snowplow model is another 0D approximation [Haines2011, Ryutov2000]. The main assumption is a cylindrical volume filled with uniform plasma, representing a gas-puff pinch. In wire arrays, a similar situation occurs with the pre-fill of the array center during the ablation phase. The current is assumed to flow in an infinitesimal skin depth of the surface of the cylinder, and the plasma shell carrying this current acts as a cylindrical piston. As the piston moves radially inward do to the **j**×**B** forces, it sweeps up and accumulates plasma. A cylindrically converging shock wave precedes this plasma, which heats up the plasma and radiates some of its kinetic energy.

1.4. Inductive current distribution

In wire arrays the load current is distributed through the wires according to their inductances – the impedance of the load is higher than the resistance of the wires – and the plasma columns the wires turn into. For example, in cylindrical arrays with changeable current return configuration, the current division between the wire and the precursor plasma obeyed the inductive current distribution [Lebedev2005b].

For cylindrical arrays with equal wire spacing the distribution is even. For nested cylindrical arrays, the inner wires have lower current, as the outer wires provide inductive shielding. For nested cylindrical arrays with high wire numbers, the current division between the inner and the outer wires can be approximated as [Velikovich2002]

$$\frac{I_2}{I} = \frac{\frac{1}{N_1} ln\frac{R_{c1}}{N_1 R_{w1}}}{ln\frac{R_{c1}}{R_{c2}} + \frac{1}{N_1} ln\frac{R_{c1}}{N_1 R_{w1}} + \frac{1}{N_2} ln\frac{R_{c2}}{N_2 R_{w2}}} , \quad (1\text{-}11)$$

where subscript 1 refers to the outer, and subscript 2 refers to the inner array, N is the number of wires in the respective array; R_c is the radius of the array and R_w is the wire diameter; I_2 is the current in the inner array and I is the total current. For arrays with over a hundred of wires, the current fraction in the inner array can be lower than 1%. For an arbitrary wire array, the current distribution can be calculated using a method that calculates the inductive current division through loops, consisting of wires and return current posts [Davis1997].

1.5. Stages of implosion in a wire array Z-pinch

The implosion of a wire array Z-pinch can be divided into four different phases. During the current prepulse, the wire cores are heated up and turn into plasma. In the ablation phase plasma from the wires is ablated and accelerated by the **j**×**B** forces. In most wire arrays, a precursor plasma column forms in the center of the array. In the implosion phase, the wire cores break up, and are moved to the center of the array. In the stagnation phase most of the array mass arrives at the center of the array, an axial plasma column - the Z-pinch itself - is formed. The pinch radiates, and is eventually disrupted by

growing MHD instabilities. Fig. 2 shows the implosion stages on a load on the ZEBRA generator.

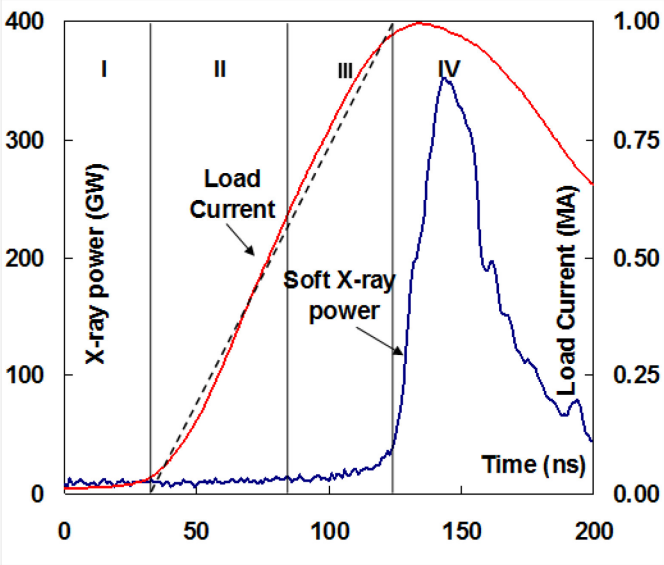

Figure 2: The stages of implosion on the ZEBRA generator, for a star array load. I: Initiation, II: Ablation, III: implosion, IV: Stagnation

1.5.1. Initiation

In some Z-pinch generators, there is a distinct electrical current before the main electric pulse, called the prepulse. On the ZEBRA generator the prepulse is approximately 200ns long and has a magnitude of 5kA. This prepulse starts the initiation stage of the wires in the array. During this stage, the Ohmic heating deposits energy in the wires, which are heated up, and a low-density cylindrical plasma sheath – a corona discharge – forms from the wire material around the dense wire cores [Kalantar1993]. Depending on the prepulse form and wire material, the wire cores can melt, and even turn into plasma in some cases. The core structure was shown to be foam-like, corresponding to the formation of vapor bubbles in the superheated liquid metal [Pikuz1999]. The increasing electric field eventually causes breakdown in the corona discharge. At this

point the current switches from the wire cores into the corona. The condition of the core at the breakdown determines the homogeneity of the ablation from the wires [Sarkisov2007]. Fig.3 shows the prepulse, the initiation phase and light/x-ray emmission on the ZEBRA generator.

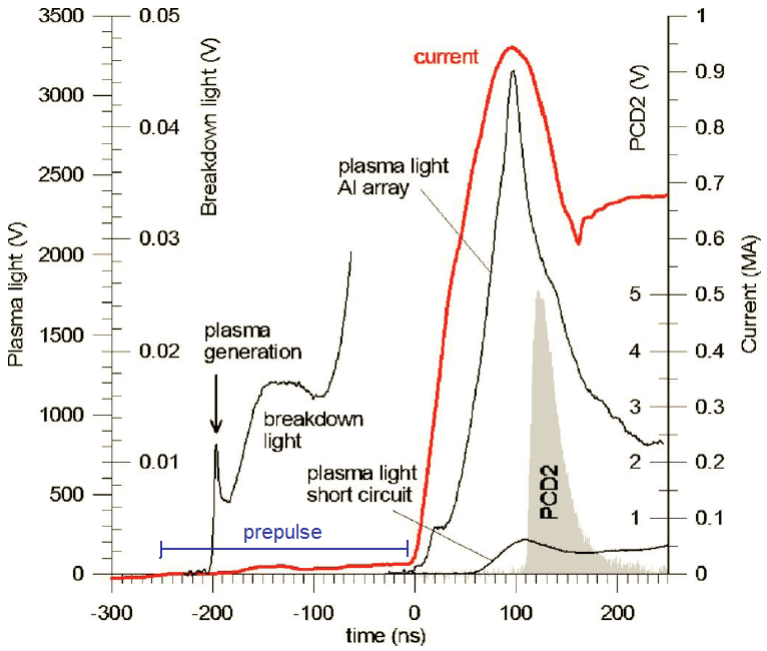

Figure 3: Current prepulse on the ZEBRA generator, and light generated by the coronal plasma, from [Sarkisov2007]

1.5.2. Ablation phase and precursor formation

The start of the ablation process roughly coincides with the start of the main current pulse. The wire cores had been heated up during the wire initiation, and the coronal plasma had already broken down. The wire cores expand, forming a dense core of 0.10-0.25 mm diameter [Lebedev1998a, Lebedev2000a, Shelkovenko2007]. This core is surrounded by the lower density, higher temperature expanding coronal plasma, in which MHD instabilities develop, dominantly m=0 type. These instabilities create a periodical structure in the coronal plasma, with characteristic wavelength that is material-dependent,

i.e. ~0.5mm for Al, 0.4mm for Ti and ~0.25mm for W [Lebedev2000a]. This characteristic wavelength is strongly coupled to the diameter of the coronal plasma, as the ratio of the wavelength and the expanding coronal plasma remains constant [Knapp2010]. The periodic structure initially forms at a smaller wavelength (~0.13mm or smaller for Al), and as both the wire cores and the coronal plasma expand, it grows into the longer, characteristic wavelength, (0.5-0.6mm for Al) in about 30ns, and then remains unchanged as the coronal plasma diameter stabilizes [Knapp2010]. The ablation was shown to be correlated in tungsten wires when the wires are placed at ~0.25mm distance – i.e. within the characteristic wavelength – but not when the spacing was over 1mm [Zier2009]. The structure of the instabilities is preserved further in the ablating plasma streams [Lebedev1998a].

With only a low current flowing through the wire cores, the ablative forces act mostly on the coronal plasma, and they remain at (or very close to) their original position for most of the implosion process. The coronal plasma is then swept by the $\mathbf{j}\times\mathbf{B}$ forces from around the stationary wire cores [Lebedev2001a]. The heated up coronal plasma ablates the wire cores by radiation, and replenishes itself. The electron temperature of ablated plasma was determined to be 20 eV by absorption spectroscopy [Ivanov2011a].

The mass removal rate can be described by different ablation models, like the rocket model [Lebedev2001a], or a somewhat different relation [Alexandrov2002]. The total mass ablation rate for the whole array was found to increase with increased wire diameter [Sinars2006, Yu2007], although the ablation rates measured in experiments ($\dot{m}\sim r_{\mathrm{wire}}^{0.66\text{-}0.92}$) were different from theoretical ones derived from simulations ($\dot{m}\sim r_{\mathrm{wire}}^{0.42}$). The

ablation speed, measured by Thomson scattering on the MAGPIE generator, varied between 50 and 120 μm/ns for cylindrical W and Al arrays [Harvey-Thompson2012].

The ablated plasma moves to the center of the wire arrays and forms an axial precursor plasma column. The precursor plasma temperature was determined to be in the range of 50-100eV for various materials on the MAGPIE generator [Lebedev2001b]. The precursor itself can carry some current, its magnitude mainly determined by inductive division between the wire array and the central precursor, but some advection of the field by the ablated plasma streams is possible. The current carried by the formed precursor was measured by B-dot probes within the array [Alexandrov2002] or by Rogowski coils in a modified current return structure [Lebedev2005b]. This current was also determined by Faraday rotation of a laser beam transmitted through the z-pinch plasma [Ivanov2006a] on the Zebra generator. The precursor was estimated to carry 5-10% of the total current on the Angara-5 [Alexandrov2002] and Zebra [Ivanov2006a] generators. On the MAGPIE generator, for cylindrical arrays with 16 wires, the precursor current was below 2% of the total current [Bott2007]. In other experiments, the precursor current varied between 2-20%, according to the inductance of return current structure [Lebedev2005b]. The precursors on the Magpie and Zebra generators are, however, different in nature. The one on the Magpie generator tends to be a well-defined straight plasma column [Bott2007]. The precursor on the Zebra generator, on the other hand, is much more irregular and displays strong kink instabilities, e.g. [Ivanov2006b]. The main instrumental difference is that the Magpie generator is a slower, 200ns risetime machine,

compared to the 100ns risetime of Zebra. The ablation process on Magpie lasts longer and displays steady-state like behavior, while the ablation on Zebra is more transient.

Instabilities in the precursor are seeded by the imprints of ablated plasma streams on the ZEBRA generator, and their development is in agreement with the evolution of current-driven flute-mode instabilities [Ivanov2006a, Ivanov2007a]. The formation of the precursor was also observed in compact cylindrical arrays at 20 MA on the Z generator [Cuneo2005].

After the plasma of the wire cores is depleted, the plasma implodes, moving to the center, and forms the Z-pinch on the axis. This Z-pinch produces the majority of the radiation during the stagnation phase, and is finally disrupted by the developing plasma instabilities.

Some interesting physical phenomena arise when wires are placed close together. In cylindrical arrays with very large number of wires, optimal wire spacing exists for maximizing the radiated K-shell power [Coverdale2002]. This optimal distance was 0.7mm for Aluminum wires on the Saturn generator. At smaller wire spacing, the maximum power of the array drops. At these small inter-wire distances, the so-called "clumping instability" arises, in which the plasma bunches azimuthally from the $\mathbf{j}\times\mathbf{B}$ attraction and forms filaments [Stickler2005].

The precursor may affect the pinch stability and the x-ray production by different mechanisms. The precursor current impacts the magnetic field within the array, and the

ablation rate on the wires. The presence of ablated material inside the array also provides MRT stabilization for the imploding plasma through "snowplowing" [Velikovich1996].

The precursor also represents a mass on the axis for the imploding plasma, which may inhibit the growth of kink instabilities. A somewhat similar phenomenon is observed in cylindrical wire arrays by introducing a wire at the center of the array, which reduced the amplitude of the plasma perturbations on the precursor, but also reduced the soft x-ray yield [Martinez2010a, Martinez2010b]. The current flowing through the precursor could also drive instabilities within the precursor and seed it to the pinch. According to 2D MHD simulations [Lemke2009], increasing the precursor mass weakens the shock interaction in the final pinch, thus lowering the maximum temperature attainable. The heavier precursor might also explain the sub-quadratic current scaling of the power in some cylindrical wire arrays [Lemke2009]. A small amount of on-axis mass, however, may enhance x-ray output by providing a target for shock heating and compression [Chuvatin2006].

The effect of the precursor in the implosion process and on the x-ray yield is not clear and can be studied in experiments. There are wire array configurations that implode without a central precursor. Linear (planar) arrays with equidistant wire spacing implode with a precursor, but in linear arrays with a large central gap no precursor was observed on the axis. The x-ray yield of the latter arrays was 5-10% lower relative to linear arrays with equidistant spacing [Ivanov2007b]. In multi-planar wire arrays, several precursor plasma columns can form within the wire array, not necessarily at the array center

[Kantsyrev2008, Kantsyrev2009]. MHD simulation of gated star arrays also showed an implosion without forming a precursor [Ivanov2010a].

1.5.3. Implosion

The wires stay at (or close to) their original position for an extended duration into the implosion process, for about 60-80% of the implosion time [Lebedev2005b, Cuneo2005, Ivanov2006c]. The ablation phase ends when the wire cores are exhausted by the mass removal, and breaks develop in the wire cores, which run out of material at certain axial positions. After this point, plasma from the wire cores start to implode, moving to the center of the array, sweeping pre-filled plasma with it. At these wire core discontinuities magnetic bubbles form [Jones2005]. These magnetic bubbles were observed in cylindrical [Lebedev2005b, Ivanov2006c] planar [Ivanov2007b] and star-like arrays [Ivanov2008a]. A shockwave can be seen as the leading edge of the bubbles (as a "piston") pushes the ablated material filling the inside of the array [Lebedev2001b, Ivanov2006c], referred as the "snowplow" model [Velikovich1996, Haines2011]. There's a broad radial mass distribution in the imploding plasma, due to the elongated bubbles. For cylindrical loads, a significant percentage of the array mass also stays at the original position, and do not arrive at the axis until the stagnation phase [Lebedev2005b, Cuneo2005].

The spatial scale for the bubble formation is larger than in the ablation phase [Ivanov2006b, Ivanov2006c], 1.7-2.3mm for Al wires. This is larger than the ~0.45mm periodicity of the wire core radius modulation and ablation. In Zebra, the leading edge moves by the speed of $1\text{-}6\cdot10^7$ cm/s (100-600 km/s), with accelerations in the order of

10^{15} cm/s^2 [Ivanov2006c]. The dispersion in speed is strongly non-uniform – even for bubbles from the same wire. The bubbles also expand axially and azimuthally, hitting neighbor bubbles. Due to the magnetic field present in the plasma, the characteristic speed of waves ('speed of sound') is the Alfvén speed [Jackson 3rd ed., p. 321]

$$v_a = \frac{B_0}{\sqrt{\mu \rho_0}}. \qquad (1\text{-}12)$$

The Alfven speed for the imploding plasma is in the order of 10^7 cm/s, so the plasma hits the precursor at supersonic velocities. The bubbles also seed instabilities in the central pinch for cylindrical arrays.

1.5.3.1. Implosion dynamics in nested wire arrays

Nested (i.e. double) cylindrical arrays produced the highest soft x-ray power, 280 TW on the Z accelerator [Sanford2007, Deeney1998, Cuneo2005]. Introducing an inner mass that the outer plasma shell could implode into mitigates the instabilities and improves the x-ray yield of the array [Hammer1996,Velikovich1996]. Nested cylindrical arrays have several implosion modes, depending on the number of wires and the relative inductance of the inner and outer array [Cuneo2005,Lebedev2001c, Chittenden2001]. In the hydrodynamic mode, the outer plasma shell impacts into the inner one, the two merge and implode together [Sanford2005]. Simulations of the hydrodynamic implosion mode predicted a factor of 2-3 improvement in radiative power. Measurements, however, showed that power increased only by 23% compared to single-array cylindrical loads, suggesting different implosion dynamics [Sanford2005].

In the transparent, current transfer mode, the current initially flow through the outside wires. When the plasma of imploding outside array passes the inner array, the current switches to the inside array as it would have the lower inductance, and the inner array would start to ablate. The transparent mode is typical on the Z generator, where the high (over 100) number of wires provides the inductive shielding on the inner array. On 1MA generators, similar effect was achieved by increasing the length (and inductance) of the inside wires [Bland2003]. The typical implosion of nested arrays on 1 MA-scale generators is simultaneous. The low wire numbers limit the inductive shielding, and significant current flows through the inner wires. This nonzero initial current starts the ablation of the inner array, and produces a magnetic flux that has to be compressed by the outer array, so the inner and outer arrays implode simultaneously [Sanford2007].

1.5.3.2. Cascade implosions

Cascade implosions were first observed on the Zebra generator [Ivanov2008a], and are typical for star-like arrays. The implosion of the array starts at the outer edges due to both the higher collective magnetic field and current, while the inner wires remain in place.

The plasma from the outer wires merges with the plasma of the wires (in the next set from the outside) and starts moving to the center, hitting the next wires, and so on. Cascade implosion results in a smoother final pinch due to the suppression of instabilities, and higher X-ray yields. The cascading ‘resets’ the growth of instabilities, and the bubble-like structure of the implosion is smoothed out. The scale of instabilities is also decreased from ~1.1mm to 0.4mm (with lower growth rates), compared to cylindrical arrays. The presence of the global magnetic field inside the array (zero in

cylindrical arrays) also inhibits instability growth. Furthermore, the trailing mass is reduced, and almost all the array mass is accumulated in the pinch.

The collision processes also mixes the material from inner and outer wires. This mixing is effectively homogeneous, providing a method for investigating two-component plasmas. In cylindrical and nested arrays, no such mixing exists, and different materials would have different spatial distribution in the stagnating pinch. This effect can be used for spectral diagnostic purposes, e.g. [Weller2012].

1.5.4. Stagnation

The radiation of a stagnating pinch is inhomogeneous from plasma instabilities, with hotspots of high intensity. The three main radiative processes in the Z-pinch plasma are continuum Bremsstrahlung radiation, continuum free-bound transitions, which is stronger than Bremsstrahlung, and line radiation from bound-bound atomic transitions. Bremsstrahlung on the Zebra generator is soft (sub-*keV*) x-rays produced by electron-ion collisions. The Brehmstrahlung emissivity is proportional to the square of the ionization state Z of the plasma. Heavier transition metals have higher ionization states, and have stronger electric fields, so they are stronger soft x-ray radiators. Line radiation produces keV photons from atomic transitions. The temperature attainable on a given generator determines which electronic shells contribute mainly to the radiation. On 1 MA machines, only light elements are highly ionized, so Al loads produce the most keV x-rays from K-shell transitions. For heavier elements, transitions from higher shells (L and M-shell) dominate. The Z generator with over 20MA drive current can ionize heavier elements. Attainable keV yields depend on the material, Al loads achieved 350kJ yield in

the 1.2-2.8keV range, while copper loads provided only 20kJ yield, but at the photon energy of 8.4keV [Coverdale2010].

The x-ray energy radiated by the stagnating pinch can be higher than what can be accounted for by the total kinetic energy and Ohmic heating from Spitzer resistivity [Deeney1991, Ivanov2009]. Several alternative mechanisms were proposed to explain this phenomenon, like enhanced Ohmic heating from anomalous resistivity due to ion acoustic or lower hybrid turbulence [Ryutov2000], resistive effect in a Hall plasma [Kantsyrev2006] dissipation of entrained magnetic flux [Velikovich2000], compressional work in the imploding plasma [Lovberg1993], interchange m=0 ion viscous heating [Haines2006], and lengthened/narrowed current path in the helically deformed pinch due to m=1 instabilities. Even with reducing the kinetic energy to a minimum by an initial array diameter not much larger than the final pinch (1 mm) the radiation is not reduced by the same extent [Ivanov2009].

There are several methods that could be used to mitigate the instabilities, which should produce more uniform plasma, and higher overall energy densities [Ryutov2000]. Increasing the initial homogeneities of the load is one way. High number of wires in a cylindrical array produces azimuthally more uniform plasma, and an increase in the x-ray power [Coverdale2002]. In nested wire arrays, the mass introduced on the inner array stabilizes the implosion of the outer array [Velikovich2006, Deeney1998]. In star wire arrays, the cascading implosion creates a smoothened plasma front, and re-sets the growth of instabilities [Ivanov2008a]. Rotation around the axis induced in the plasma

might lead to sheared flow in the pinch, which can also have stabilization effect [Velikovich1995, Sotnikov2002].

1.6. Instabilities in Z-Pinches and instability mitigation

There are several types of plasma instabilities that play a key role in the physical processes at every stage of the implosion. The specific instabilities are not dominant through the whole implosion, but the inhomogeneities produced by one instability can seed follow-on ones. These instabilities are the explanation why high-symmetry (0D or 1D) models have difficulty describing the Z-pinch properly.

In the ablation phase, the wire corona displays periodic modulations, and the wire cores break up from m=0 MHD instabilities. The ablating plasma forms a corresponding periodic jet structure on the wire cores [Lebedev2000a]. The precursor is also subjected to Magnetic Rayley-Taylor instabilities, the m=0 ("sausage") and m=1 ("kink") instabilities.

The imploding plasma is characterized by plasma bubbles (loops) that form when the wire cores break up [Ivanov2006c]. These bubbles can break up again forming plasma streams. Furthermore, the imploding plasma is also subject to the magnetic Rayleigh-Taylor instability. The stagnating pinch is finally broken up by the development of the m=0 and m=1 instabilities.

1.7. Plasma flow control in wire array z–pinches

As the ablation of the coronal plasma around the wire cores is driven by the $\mathbf{j}\times\mathbf{B}$ forces acting on the plasma, changing the magnitude and direction of the initial $\mathbf{j}\times\mathbf{B}$ forces allows

some control of the ablating and imploding plasma flows. This was demonstrated in some specific wire array configurations.

In one experiment on the MAGPIE generator, a linear array was placed close to a flat current return surface, which provided a strong unidirectional magnetic field at the wire positions [Bland2004]. This resulted in an ablation that was oriented outward of the array. On the 0.45MA Cornell XP pulser, the magnetic field in high-current Z-pinches was simulated by a 4-ray linear array and a close return current rod [Hu2005]. In conical wire arrays, the ablation is perpendicular to the wires with an axial component [Ampleford2007], corresponding to the direction of the ablative forces. In the implosion of radial wire arrays the **j**×**B** forces produce a collimated plasma jet on the axis, combined with a somewhat broader outflow, perpendicular to the array plane [Lebedev2008a]. Using wires of different wire lengths can be used to change current distribution within a nested array [Bland2003]. The transparent/nontransparent implosion mode of nested arrays can be simulated by "gated" star arrays [Ivanov2010a]. Implosion dynamics can also be influenced by having an implosion velocity much higher than the speed of ablation. On the Z generator, compact (20mm or smaller diameter) regular (with several mm distance between the inner and outer arrays) nested arrays implode with precursor plasma forming at the center of the array, similar to cylindrical wire arrays. In large array diameter with low wire number (e.g. 70mm diameter with ~100 wires in the outer array), however, there may be no dense axial precursor plasma. Ablated plasma traveling with a speed of 150km/s would not reach the axis during the 100ns implosion time, and the ablated pre-fill is swept by the imploding array [Jones2008].

1.8. Research Summary

In this dissertation three different research topics will be covered, First, plasma flow control was used to simulate the "transparent" and "non-transparent" implosion regimes of nested wire arrays, in star-like wire arrays with the innermost wires replaced by wire pairs (gates). The significant (25% of the total) current through the innermost wires trapped the plasma flow from the outer wires. The current through the inside wires was reduced by increasing the length and inductance, and instead of trapping, the plasma passed between the wires. The transparency of the arrays was diagnosed by UV laser shadowgraphy.

Second, stabilization effect of the precursor discharge was investigated in nested and star-like wire arrays. Different theories suggest effects both improving and degrading the stability of the final pinch, and experimentally verifying either effect would allow improving the x-ray yield of wire array Z-pinches. The presence of precursor was predicted from the direction of $\mathbf{j}\times\mathbf{B}$ forces on the innermost wires, and could be changed by changing the array configuration. Star wire arrays followed this prediction, and the presence of the precursor degraded the x-ray yield by a small amount (3-15%). In closely spaced nested arrays ablation to the center was observed with shadowgrams, independent of the calculated direction of $\mathbf{j}\times\mathbf{B}$ forces. In low wire number arrays the plasma accumulation on the axis was delayed, due to the (conjectured) speed of the ablating plasma being lower. These experiments also provided an unexpected result, where significant (up to 100%) improvement in Al K-shell x-ray yield was observed in low-wire-number arrays.

Third, cooling effect of high-Z materials in Al plasmas would be presented. The cascading implosion of star wire arrays allows the mixing of different wire materials. The presence of high-Z material reduces the Al K-shell yield and cools down the plasma. Spectroscopic analysis with PrismSPECT code shows a cooling effect of ~40eV in Al-Au plasma. In contrast, in Al-Au plasmas produced by 0.8ns laser pulses no cooling effect was present. This difference could be attributed to the different heating mechanisms in laser and Z-pinch produced plasmas.

2. PLASMA DIAGNOSTICS AND EXPERIMENTAL SETUP

2.1. Optical diagnostics

2.1.1. Intensified CCD and Optical Streak camera

In an Intensified CCD (ICCD) camera, incident light create electrons on a low work function cathode, and the photoelectrons are multiplied though a multichannel plate. This allows the imaging of the low-intensity optical self-radiation of the pinch during the early stages of implosion.

A streak camera is another electron optics device, which records the time evolution of a 1D image, created by a slit. The image creates photoelectrons, which are accelerated in a cathode-ray tube (CRT). Changing the transverse electric field applied in the CRT projects the images at different location on the CRT screen. Ramping up the voltage in time therefore allows the recording of an image, with one axis corresponding to position along the 1D image, and the other axis corresponding to time.

2.1.2. Laser diagnostics

2.1.2.1. Dark field schlieren imaging

Dark-field schlieren diagnostics uses the refraction of the incident laser by plasma gradients. The refraction is sensitive to density gradients perpendicular to the propagation of laser beams. The plasma is imaged with an optical system to an image plane. With a knife edge at one focal point, the undeviated beam is blocked. The refracted beam itself is not focused by the lens to the same focal point, and is unblocked. This allows the imaging

of gradients in low-density plasmas [Hutchinson2002 p. 130]. A dark field schlieren image uses the same beamline used for shadowgraphy, with the knife wedge installed at a focal point.

The refraction angle of a laser beam passing through plasma with density variations perpendicular to the direction of propagation can be written as [Hutchinson2002 p. 125]

$$\theta = -\int_0^l \frac{\partial}{\partial y}\frac{n_e}{n_c} dl = -\frac{\lambda^2 e^2}{4\pi^2 c^2 \epsilon_0 m_e}\int_0^l \frac{\partial n_e}{\partial y} dl \,. \quad (2\text{-}1)$$

On the image at a distance L from the plasma, this diffraction shows up as a density variation [Hutchinson2002 p. 131]

$$\frac{\Delta I_d}{I} = -L\left(\frac{\partial^2}{\partial x^2} + \frac{\partial^2}{\partial y^2}\right)\int_0^l \frac{n_e}{n_c} dl = -\frac{\lambda^2 e^2}{4\pi^2 c^2 \epsilon_0 m_e} L\left(\frac{\partial^2}{\partial x^2} + \frac{\partial^2}{\partial y^2}\right)\int_0^l n_e dl \,. \quad (2\text{-}2)$$

With the knife edge blocking the undeviated beam, only such intensity variations will be present on the image.

2.1.2.2. Shadowgraphy

In laser shadowgraphy, a short-pulse laser is used to make snapshots of the plasma, and the image is projected onto a CCD camera. The contrast of the shadowgram is created by both the absorption in the plasma, reflection at and above the critical density, and refraction on gradients dominantly at the edge of the plasma. The intensity of the refractive contribution is proportional to the second spatial derivative of the electron density normal to the probing beam [Hutchinson2002 p. 131]. In the probing of Z-pinch

plasmas, usually the absorption in the plasma is dominant, but it depends on the density gradients.

The electric field of an electromagnetic (EM) wave propagating through the plasma interacts with the free electrons in the plasma. The free electrons oscillate and re-emit the laser wave. The dispersion relation of an EM wave through the plasma is given as

$$kc = \sqrt{\omega^2 - \omega_p^2}\,, \tag{2-3}$$

where the plasma (angular) frequency of the electrons is

$$\omega_p = \sqrt{\frac{n_e e^2}{\epsilon_0 m_e}}\,. \tag{2-4}$$

If the laser frequency is lower than the plasma frequency, the EM radiation is absorbed. So for a given wavelength λ there exists a critical plasma density n_c, above which the plasma is opaque to the incident light

$$n_c = \frac{4\epsilon_0 m_e \pi^2 c^2}{\lambda^2 e^2}\,. \tag{2-5}$$

The critical density for a visible, green 532nm wavelength laser is $n_c = 3.92\times10^{21}$ cm^{-3}. The absorption of the laser in the plasma is mainly through the inverse bremsstrahlung –the photons collide with electrons, and the latter transfer their energy to other electrons by collisions. The absorption coefficient of this process is given by [Johnston1973] as

$$\kappa = 3.1\times10^{-7}\,\frac{Zn_e^2\ln(\Lambda)}{T_e^{3/2}\omega^2}\frac{1}{\sqrt{1-\omega_p/\omega}}\;[cm^{-1}]\,, \tag{2-6}$$

where n_e is in cm^{-3}, T_e is in eV, Z is the ionization state of the plasma, and $\ln(\Lambda)$ is the Coulomb logarithm. The latter has values around 6 to 12 in Z-pinch plasmas, and is a slowly (logarithmically) varying function of temperature and density. The latter two equations show that higher frequencies are more suitable to study higher plasma densities, as both the critical density is higher, and the absorption is lower.

2.1.2.3. Other laser diagnostics methods (interferometry and Faraday rotation)

The free electrons in the plasma induce a phase shift in the EM radiation, which can be detected using interferometry. The phase shift in the plasma can be given as [Hutchinson2002 p. 112]

$$\varphi = \frac{e^2\lambda}{4\pi\epsilon_0 m_e c^2}\int_0^l n_e(x)dx\ , \tag{2-7}$$

where l is the plasma thickness. On the setup used on the Zebra generator, an air-wedge interferometer [Sarkisov1996] is used, where the image is shifted laterally, and interfered with the original beam.

The Faraday rotation imaging is based on the Faraday Effect. If a polarized light travels through a medium with magnetic field parallel to the direction of propagation, the polarization plane of the probing beam is rotated. The magnitude of the rotation is expressed by [Hutchinson2002 p. 131]

$$\beta = \frac{e^3\lambda^2}{2\pi\epsilon_0 m_e^2 c^3}\int_0^L B_z(z)n_e(z)dz\ . \tag{2-8}$$

With the electron density known (e.g. from interferometry), the magnetic field within the plasma can be inferred. It should be noted that eqns (2-7) and (2-8) are valid only if the plasma density is significantly smaller than the critical density, so that $(1-n/n_c)^{1/2}$ is close to unity.

2.1.2.4. UV laser diagnostics

The most commonly used diagnostic laser for z-pinch plasmas are Nd:YAG lasers operating at the second harmonics at 532nm. Probing at this wavelength has some shortcomings, mainly that the absorption at this wavelength is very strong in dense plasmas, and also strong refraction on the density gradients. This limits the utility of 532nm probing mostly to the ablation and implosion phase for z-pinch plasmas. Laser probing at higher frequencies provides significant benefits in investigating dense plasmas. The absorption, refraction, phase shift and Faraday rotation angle all decrease in

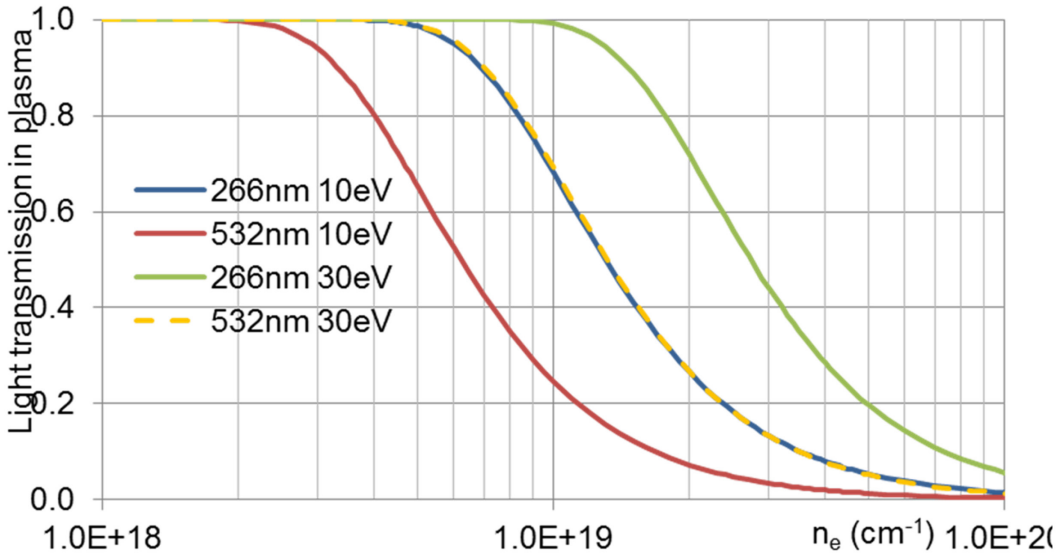

Figure 4. Transmission coefficient for laser beams at wavelengths of 266nm (violet lines) and 532nm (grey lines), through 1mm thick plasma, as a function of electron density, at two electron temperatures typical for the ablation-implosion stage.

plasmas with increasing the probing beam frequency. At 266nm the critical plasma density is $n_c = 15.68\times10^{22}$ cm^{-3}, four time the critical density at 532nm. As seen on eqn (2-6), the inverse bremsstrahlung absorption also strongly decreases with the frequency. Fig.4 plots the transmission of the laser light as a function of electron density at 532 and 266nm, for temperatures typical for the ablation and implosion stage. Due to the high transmission UV lasers offers the capability to probe 2-3-times denser z-pinch plasmas, especially at the later (implosion and stagnation) stages.

UV probing of dense Z -pinches (shadowgraphy, interferometry and Faraday diagnostics) was developed at the University of Nevada, Reno, using the fourth harmonics of a Nd:YAG laser at 266nm [Ivanov2010a]. Third harmonics (355nm) probing was also used at the MAGPIE generator [Swadling DZP2011].

2.2. X-ray diagnostics

2.2.1. Diagnostics for x-ray energy, power and pulse shape

X-ray emission was recorded by bolometers, x-ray diodes (XRD) and diamond photoconducting detectors (PCD). Fig.5 shows the signal of these detectors for an Al array on the ZEBRA generator. Bolometers measure the time-integrated energy of the incident electromagnetic radiation. They consist of Ni or Au films 200μm thick on an insulator substrate. They are heated up by the incident radiation, which increases the resistance of the film. There is a roughly linear dependence between the change in resistance and absorbed energy. Measuring the voltage drop over the film at a known current gives a signal proportional to the time integral of the x-ray power.

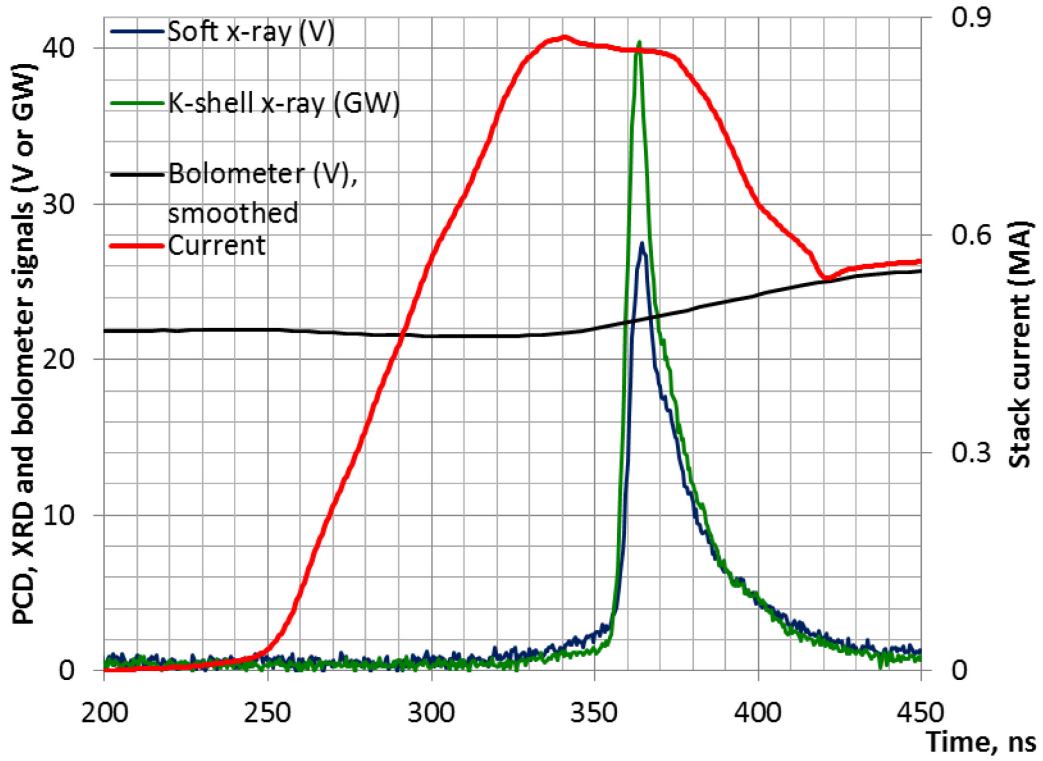

Figure 5. X-ray signals for Zebra shot #987, a 16×10μm Al nested 16/8mm wire array. Soft x-ray signal is recorded by XRD with 2μm Kimfoil filter, K-shell x-ray (calibrated) is recorded by a PCD with 8μm Be filter, Bolometer signal is smoothened. Current is integrated from stack B-dot probe.

An X-ray diode (XRD) consists of a planar photocathode and a collecting anode mesh [Chandler1999]. The photocathode is a diamond polished vitreous carbon disk 12.5mm in diameter and 2mm in thickness. The charge saturation current for such a photocathode is 28 A/cm^2. The sensitivity of an XRD is strongly dependent of the photon energy, with a variation of over two magnitudes in the spectral range of z-pinch x-ray emission. The integrated XRD signals for all shots during a campaign can be normalized by the bolometer energy values, which can be used to determine the soft x-ray power from the peak of the XRD signal. This calibration is not very accurate, as the variation of the x-ray spectrum varies from shot to shot, and the XRD sensitivity has strong energy

dependence. The XRD detector was used with a 2µm filter, which combination has two "windows" of high sensitivity, in the x-ray ranges of 130 to 300eV, and 400 to 2000eV (Fig.6).

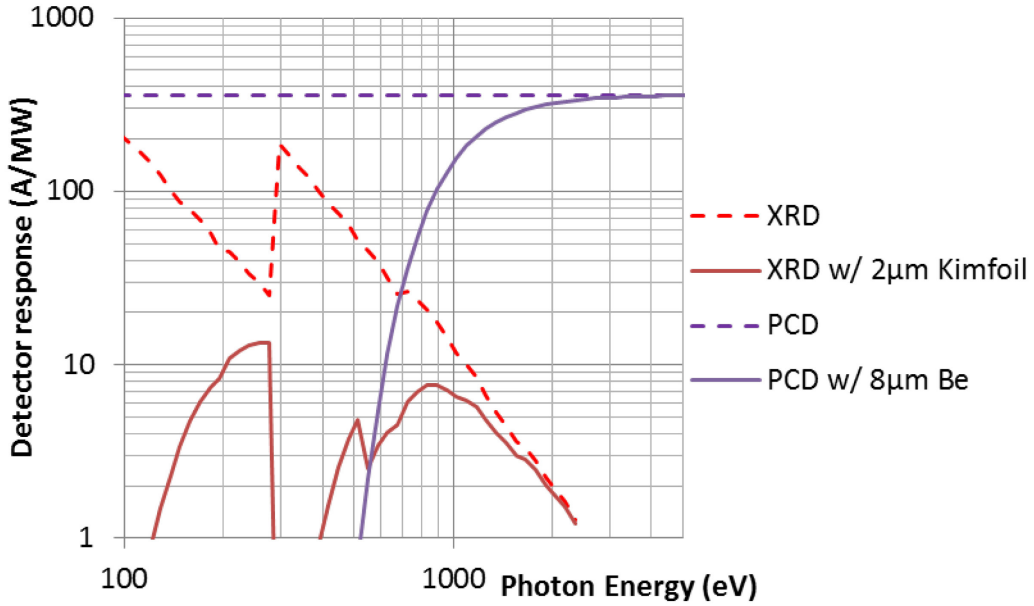

Figure 6. Response of bare and filtered x-ray detectors. XRD and PCD data from [Spielman1995], filter data from [Henke1993]

A photoconductive detector (PCD) is a resistive element, made of an intrinsic semiconductor [Spielman1995]. Absorbed photons create electron-hole charge carrier pairs in the semiconductor, increasing the conductivity of the crystal. The PCDs used were built from gem-quality diamond, with a 3x1mm surface facing the radiation [Spielman1992]. A PCD has a flat energy-response curve in the 10eV-6keV range. The PCD was used with a 8µm Be filter that cuts off most x-ray radiation below 1000eV energy (Fig.6).

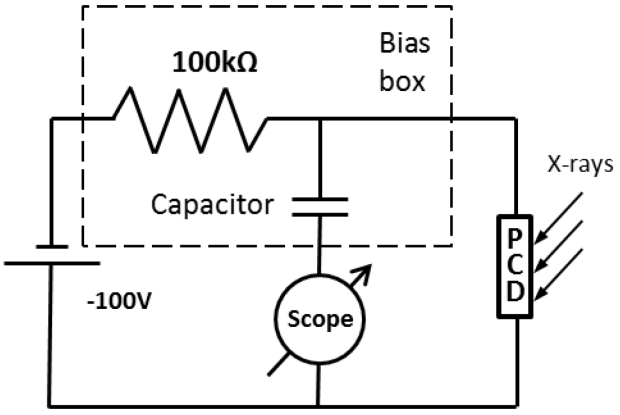

Figure 7. Circuit diagram of the PCD detector

The circuit diagram of the PCD is shown in Fig.7. The -100V bias is applied on a "bias box", which contains the 100kΩ resistor and the capacitor. The capacitor acts as a high-pass filter, filtering out the DC signal. When there is no radiation on the PCD, the capacitor is charged to the -100V bias voltage, there is 100V drop on the PCD, and no current flows through the oscilloscope (with 50Ω internal resistance on a high-frequency input). Incident radiation decreases the voltage drop on the PCD, which is recorded on the oscilloscope (with the -100V DC signal filtered out). There is also a "saturation effect" on the PCD. When the incoming radiation is strong, and the PCD output voltage is over ~20% of the bias (i.e. 20V), the voltage drop over the PCD is less (e.g. 80V), and the PCD current drops correspondingly.

In the unsaturated range, the PCD signal V_{m} is proportional to the incident x-ray power $P_{\text{x-ray}}$:

$$V_m = \frac{a_{PCD}}{4\pi r^2} AkFRP_{x-ray} \ . \tag{2-9}$$

The fraction stands for the detector solid angle. Placed at $r = 2.02$m distance from the z-pinch, the $a = 3\text{mm}^2$ surface area of the detector corresponds to a solid angle of

Ω=5.85×10^{-8} sr. The installed signal attenuation in the setup is A=0.25 (-12dB). The sensitivity of the used PCD detector (PCD #2) was k = 3.28×10^{-4} A/W. The average filter attenuation, F=0.82 was calculated for a typical Al K-shell spectrum and the transmission of the 8μm Be filter. The resistance of the high-frequency input on the oscilloscope was R=50Ω.

The saturation correction for the PCD signal [Spielman1988] is then

$$V_c = \frac{V_m}{1 - V_m/(AV_b)}, \tag{2-10}$$

where V_c is the corrected signal, V_m the measured PCD signal on the oscilloscope, A is the scope signal attenuation and V_b is the applied bias voltage. This gives the overall sensitivity of this detector as 1.96×10^{-10} V/W.

2.2.2. X-ray Spectroscopy

Important information on the plasma characteristics, particularly N_e and T_e, can be derived from spectroscopic measurements. In the case of Aluminum (and Al-Mg alloys), the high temperature in the final pinch ionizes the plasma to a great extent (Z>10), and the characteristic line radiation is composed dominantly of the K-shell lines of H and He-like Al (and Mg) ions and their satellites. These lines fall into the x-ray energy range of 1.3-2.3keV, or 5.4-9.5Å wavelength.

The spectrum of an x-ray source can be obtained by a dispersive single crystal element, which has selective reflection described by Bragg's law,

$$2d \cdot \sin\theta = m \cdot \lambda, \tag{2-11}$$

where d stands for the separation between the specific atomic planes in the crystal, θ is the angle of incidence for the incoming x-ray, λ is the wavelength that is reflected in the angle θ, and m is an integer, referred as the order of diffraction. A convex KAP (Potassium Acid Phthalate) spectrometer was used to record time integrated spectra during Z-pinch (Zebra) and laser (Leopard) shots. The KAP spectrometer used first-order Bragg reflections, as the reflectivity of the crystal is significantly lower at the second and third orders.

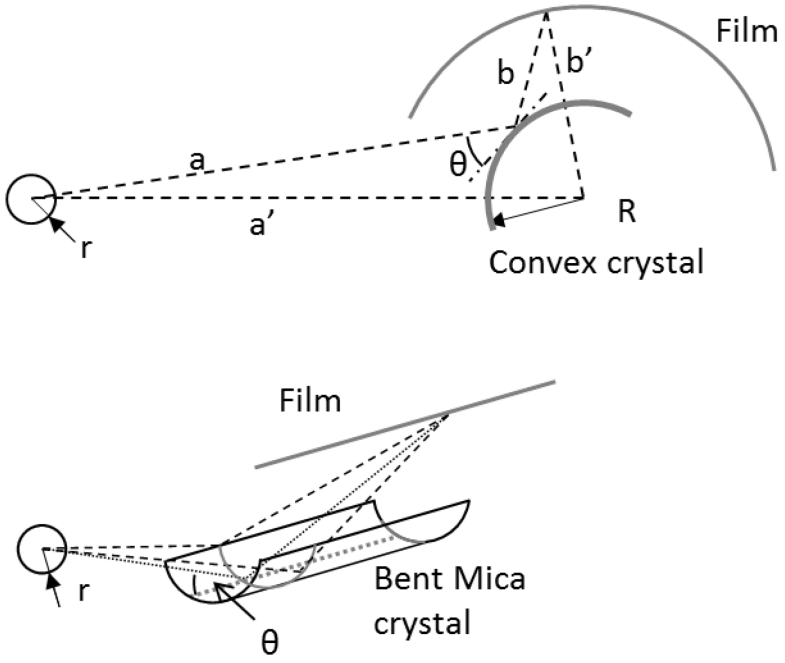

Figure 8. Schematics of a convex crystal spectrometer (top), and a von Hamos spectrometer (bottom).

Convex-crystal spectrometers can register x-ray radiation in a wide spectral range [deBroglie1914, Swartz1971]. A cylindrical von Hamos spectrometer [Shevelko2002] was also used for LEOPARD laser shots within the PHOENIX target chamber. The cylindrically bent mica crystal focuses the reflected X-rays, enhancing the intensity does

not provide spatial resolution. The spectral resolution in this instrument was not high due to the affordable but low quality split mica crystals used. The mica crystal has strong 3rd and 5th order reflection, but in the experiments only the first order was used. At the experimental geometries and used materials there was no high-energy x-ray radiation that would show up at the higher orders. The dispersion of the convex crystal spectrometer can be given as [Swartz1971, Fedin2004], with notation as in Fig.8

$$D = cot\theta \cdot \frac{\lambda}{a+b}, \tag{2-12}$$

and the resolving power as

$$\frac{\lambda}{\Delta\lambda} = \frac{\sin\alpha}{2r}\frac{R\cdot\sin\theta + a}{R\cdot\sin\theta + b}. \tag{2-13}$$

The spectral luminosity $\xi = I/SI_0$, the ratio of the incident intensity on the detector (film) of area S from a monochromatic source with intensity I_0 over a solid angle of 4π, can be expressed as

$$\xi = \frac{R}{a'b(a+b)}\frac{sin\theta}{\sqrt{1-R\cdot cos\theta/a'}} \sim sin\theta \sim \lambda. \tag{2-14}$$

The spectrometer had a slit perpendicular to the pinch axis, providing an axial image of the pinch with a spatial resolution down to 0.5mm, which depends on the slit width and the distance between the spectrometer and the pinch. Filters were used to protect the film from exposure to light and soft x-rays. As the slit is perpendicular to the pinch, the finite width of the pinch creates an instrumental broadening.

The spectrometer was placed 550-800mm from the pinch, and the distance between the crystal and the film was 51mm. The lattice constant of the KAP crystal in the used [001] direction is d=13.3Å. For the Al-Mg K-shell spectrum of 5.6-9.2 Å, the value of $\tan\theta$ is 0.2-0.36, and $\tan\theta$~0.3 for the Al He-α line at 7.76Å. The finite size of the source causes a source broadening of the spectra. Assuming 1mm source radius at the minimal distance 550mm, the resolving power (eqn. 2-11) of the spectrometer at this line is $\lambda/\Delta\lambda$ ~180, or $\Delta\lambda$~0.043Å. This source broadening is the dominant broadening effect for the spectrum. With laser plasmas of smaller size (~0.1mm radius), the resolving power can be over 1000, in which case the effect of source broadening would be comparable to (or smaller than) other mechanisms.

On the Zebra chamber, the resolution of the spectrometer was $\lambda/\Delta\lambda$ =200-350, depending on the distance from the pinch. When used with laser plasmas, $\lambda/\Delta\lambda$ >500 resolution was achieved.

The intensity of the radiation, as recorded by the photographic film, is influenced by several wavelength-dependent factors. The film sensitivity is given by optical density/photon flux, and the intensity incident on the film for a given photon flux is proportional to $1/\lambda$. The reflectivity of the crystal ρ is wavelength-dependent, and was taken from [Gilfrich1975]. The spectrometer luminosity ξ is proportional to λ. Finally, the transmission T of the filters must be taken into account. This gives a calibration of

$$I_{experimental} \sim \frac{I_{film}}{T\,\rho\,\lambda^2} \quad . \qquad (2\text{-}15)$$

Normalized calibration coefficients for the spectrometers used in experiments are shown in Fig.9. The recorded spectra were digitized using an EPSON V700 photoscanner. Pixel intensity values corresponding to the specific optical density (OD) of the film were determined by a Stouffer step wedge. Film sensitivity (film OD dependence on incident intensity) for the Kodak BIOMAX film was taken from [Marshall2006]. The calibration was valid up to a film OD of 3.5.

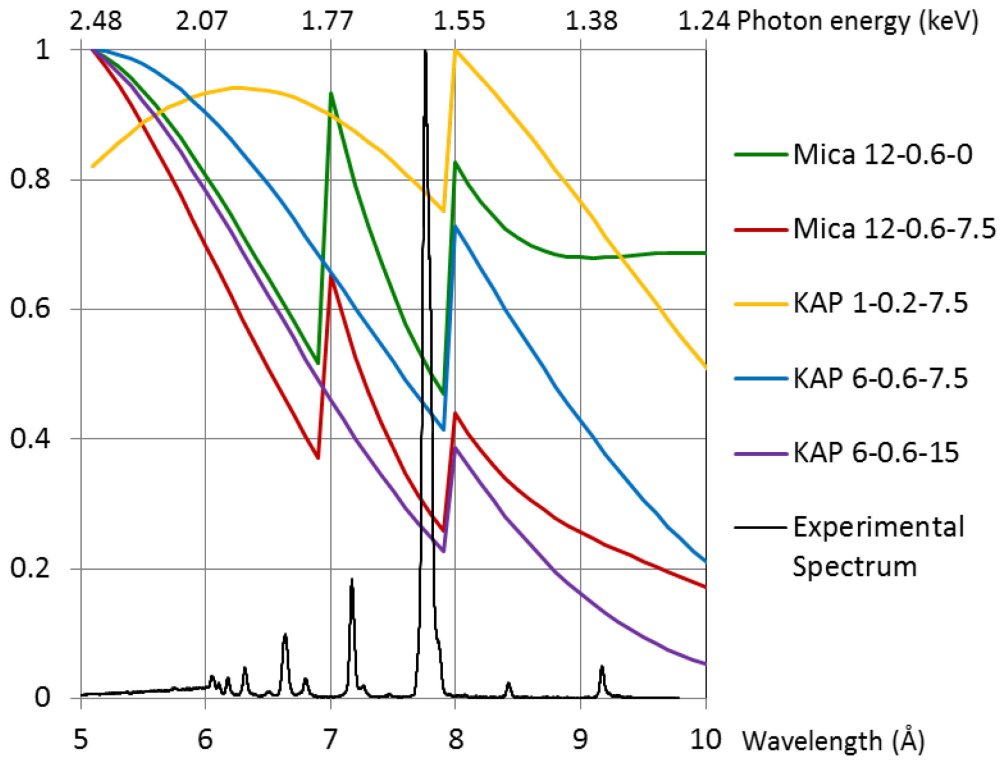

Figure 9. Normalized spectrometer calibration coefficients (from crystal reflectivity, filter transmission and film response) used in experiments in the Zebra and Phoenix chambers, and experimental spectra for an Al-Mg alloy wire array z-pinch. Mica crystal with 12μm Mylar and 0.6μm Al filters (thicknesses are total for one or more foils); Mica crystal with 12μm Mylar, 0.6μm Al and 7.5μm Kapton filters; KAP crystal with 1μm Mylar, 0.2μm Al and 7.5μm Kapton filters; Mica crystal with 6μm Mylar, 0.6μm Al and 7.5μm Kapton filters; Mica crystal with 12μm Mylar, 0.6μm Al and 15μm Kapton filters.

2.3. The Zebra generator, the Leopard laser and diagnostics setup

2.3.1. The Zebra generator

The Zebra Z-pinch pulsed-power generator, used for conducting the wire array Z-pinch experiments described in this dissertation, is located at the Nevada Terawatt Facility of University of Nevada Reno, in Reno, NV. The generator was developed and built at the Los Alamos National Laboratory under the name HDZP-II [Schlachter1990]. While the generator was designed to deliver 1.2MA into an inductive D_2-ice fiber Z-pinch load with a rise-time of 100ns. Current operations at the University of Nevada are limited to a nominal 1MA to reduce wear on the capacitors. Schematics and photo of the generator is shown in Fig.10.

The generator has three power storage and compression stages, connected by switches. The first stage consists of a Marx capacitor bank of 32 1.3μF capacitors placed in an oil tank. The capacitors are charged parallel to 85kV (the maximum voltage is 100kV), and can store a total energy of 150kJ at 85kV. The Marx bank is triggered in series by SF_6-filled spark gap switches. The intermediate storage capacitor of 27nF, a pair of nested stainless steel bottles, is charged by the first stage, and fired by a SF_6-filled Rimfire switch. The third stage consists of a coaxial vertical transmission line with an impedance of 1.9Ω, and a self-breaking water switch. A short section of magnetically insulated transmission line (MITL) minimizes the inductance of the current feed to the load and shields the insulator stack from breakdown. The generator is capable of in average 2-4 shots per day.

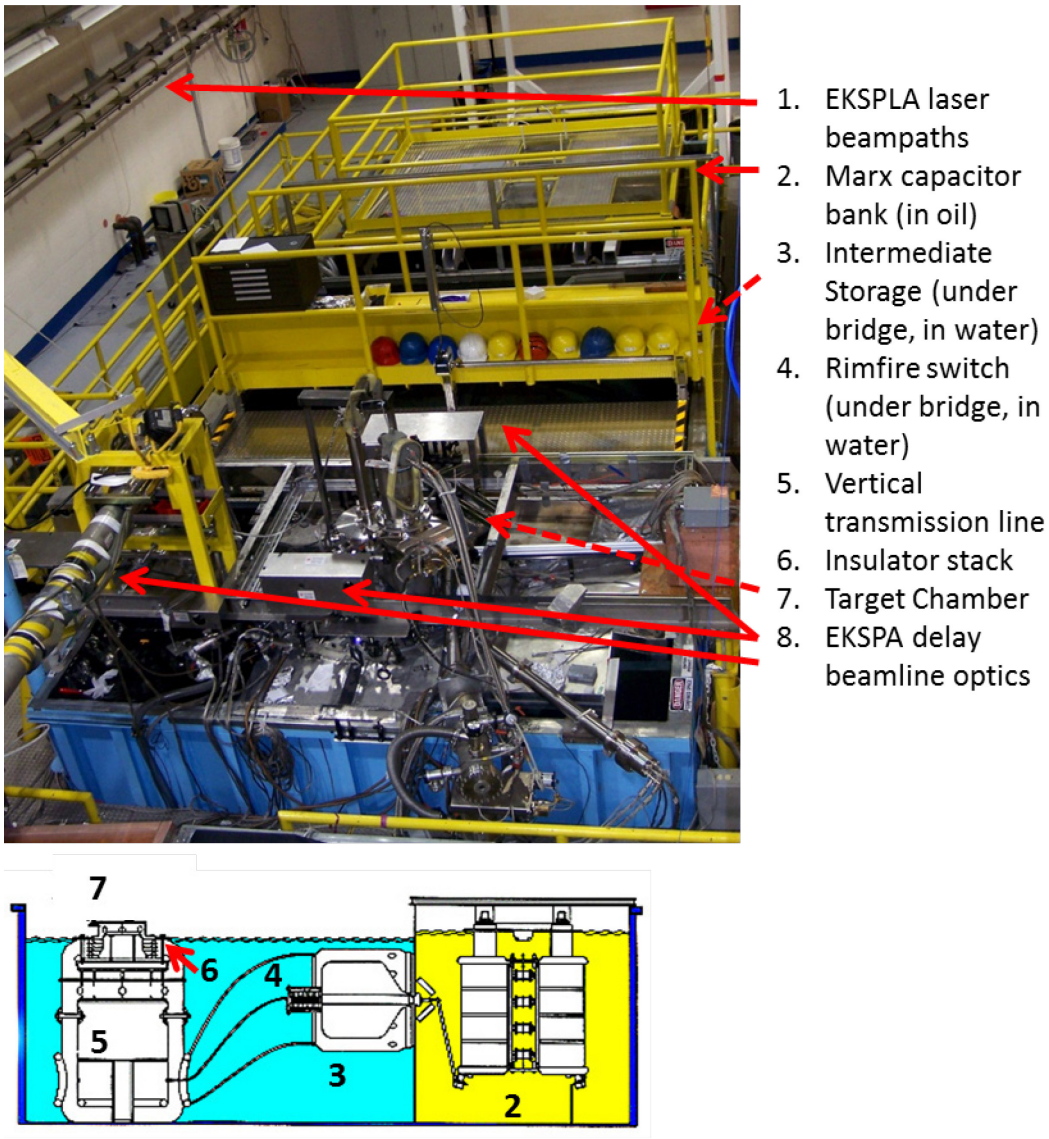

Figure 10. The Zebra generator and its schematics

The current through the loads can be determined by B-dot probes. B-dot probes at the insulator stack, below the load gives an approximate value for the load current. The load current can be determined more accurately by three pairs of differential B-dot probes located around the load. The load current in the Zebra chamber can be increased by a Load Current Multiplier [Chuvatin2009]. With 85kV capacitor charge, up to 1.6MA load current was produced.

2.3.2. Diagnostics setup on the Zebra generator

The physical diagnostics setup of the Zebra generator chamber is shown in Fig.11. The chamber has the outer diameter of 608mm. The optical streak camera and the ICCD are placed at the North port. The x-ray diodes are located at the NE port in a single five-channel head. The time-gated pinhole camera and the time-integrated spectrometers are located SE. Three pairs West and East ports are used for laser probing in three separate optical channels. Timing information and the x-ray diagnostics signals are recorded on several oscilloscopes placed in shielded enclosures to protect the electronics from the EM pulse of the generator.

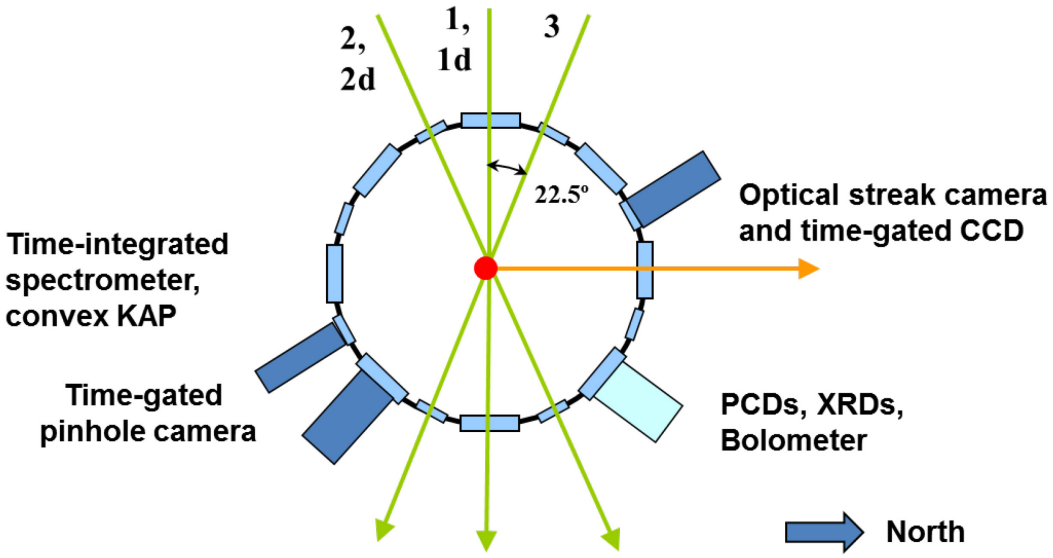

Figure 11: Physical configuration of the diagnostics around the Zebra chamber. The red disk at the center of the array represents the pinch.

There were two YAG lasers used for diagnostics, both built by the company EKSPLA. The first laser operated on the second harmonics (532nm green), had a pulse length of 150ps and a maximum power of 80mJ in the second harmonics. The beam was

split by the two polarizations, and the second polarization was 6-25ns delayed before merging back, which provided two-frame probing on a single channel. This two-frame beam was split into two channels, for a total of 4 frames: 1, 1d (delay), 2 and 2d [Ivanov2010a]. The timing between channels 1 and 2, and the regular and delay frame could be varied by changing the beampath lengths. The second operated the fourth harmonics (266nm UV), with a maximum UV energy of 120mJ. Channel 3 was used for UV probing.

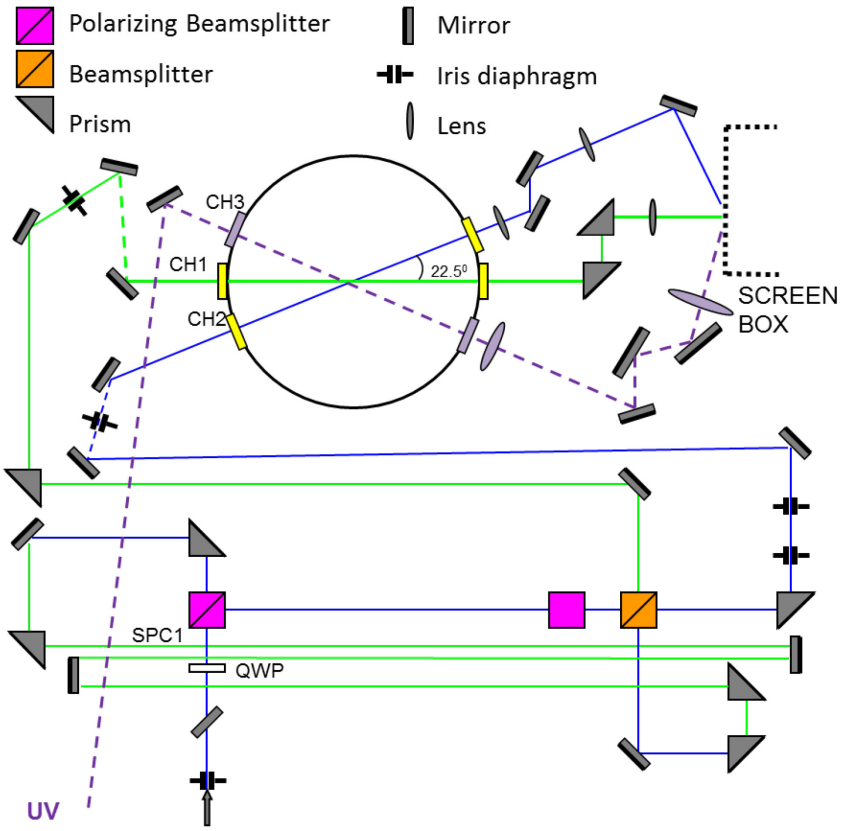

Figure 12: Schematics for the EKSPLA diagnostics beamlines on the Zebra generator

Lens systems after the chamber provided an image resolution of around 20μm. Neutral density filters attenuated the probing beam before the CCD cameras, built by Finger Lake Instruments. Narrowband filters (at 532nm and 266nm) were used to filter out the self-emission of the pinch. The cameras were set to a 0.2ms shutter time, but their exposition happened only through the laser pulses. The laser diagnostics setup and the delay line is shown in Fig.12.

2.3.3. Leopard laser and the Phoenix target chamber

The Leopard laser is a hybrid Ti:Sapphire/Nd:Glass laser system using chirped-pulse amplification, capable generating sub-picosecond pulses [Wievior2010]. The front-end uses a mode-locked Ti:Sapphire oscillator with 130fs pulse length, which is stretched to 1.3ns. Stretched pulses are seeded to a Ti:Sapphire regenerative amplifier with a gain of over 10^6. A fast Pockels cells reduce repetition rate from 500Hz to 100Hz and a second one improves contrast ratio. The amplifiers include four stages of rod Nd:Glass amplifiers, and one (upgraded to two) 94mm disk amplifiers. The amplifier stages are separated by beam expanders, spatial filters, Faraday isolators and Pockels cells. Adaptive optics is used to correct laser beam wavefront aberrations and allows 8-times improvement in focal spot size, down to 10μm with an off-axis parabola. A spatial compressor is available to compress the beam to 0.35ps. The beam can be transported to the Zebra target chamber, but for standalone Leopard experiments the Phoenix target chamber is used, which is equipped with a precision target positioning system. Diagnostics system provides laser parameters, like shot energy, duration and intensity profile. Without the compressor, the laser operates in the long-pulse regime with 0.8ns

pulses, and energies up to 50J. In the short-pulse mode, the maximum laser energy is 15J, mostly limited by the damage threshold of the compressor.

The Leopard laser was used for mixed-plasma experiments in the Phoenix chamber in the long-pulse regime. Focusing of the beam was done by an f=50cm lens, and a focal spot size of ~Ø25μm was achieved. The 30-40J laser energies used corresponded to a laser intensity of ~10^{17} W/cm^2. The Leopard laser room and the target chamber are shown in Fig. 13.

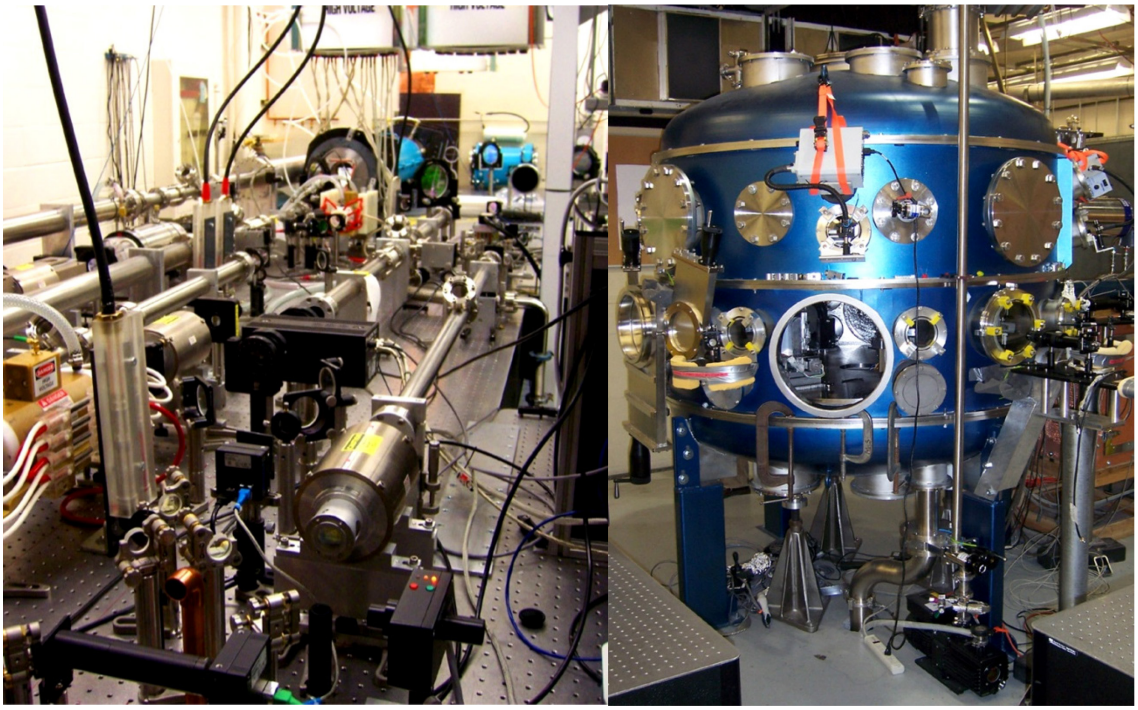

Figure 13. The Leopard laser room with different amplifiers (left) and the Phoenix target chamber (right) used in the experiments.

3. TRANSPARENT AND NONTRANSPARENT IMPLOSION REGIMES IN SMALL-WIRE-NUMBER ARRAYS

3.1. The goals of experiments on the 1MA Zebra accelerator

Nested wire arrays with over 100 wires on the Z accelerator implode in the transparent regime, where the inner wires stay at their original positions until the plasma from the outer wires pass through them [Deeney1998]. The inductive shielding of the outer wires reduces the current in the inner array, so they would implode only after the current from the outer array switches to the inner array. This transparent implosion offers only a fraction of improvement that is suggested by simulations for nontransparent arrays [Sanford2005]. Nested wire arrays on university-scale, 1MA machines are imploding with different dynamics, as the current fraction in the inner wires is higher in low-wire number nested arrays. To suppress the inner current fraction, the inductance of the inner wires can be increased by placing longer (up to 4×) wires on the inner array. Such a scheme was used to reproduce the transparent implosion regime on the MAGPIE generator [Bland2003].

Star-like wire arrays [Fig.1(c),(d),(e)] are low-wire number arrays that have a distinct, *cascading* implosion mode [IvanovPRL2009, Haboub2008], and also produce short, high-power x-ray pulses. In these wire arrays the majority of the current flows through the outer wires. The magnetic field is also the strongest on the edge of the array. This causes the outside wires to heat up the earliest, ablate and implode into the next wires inside, sweeping them into the next wire and so on. The implosion cascades from one

wire to the next, and produces a smoothened plasma front, which helps the mitigation of instabilities in the stagnating pinch.

In experiments conducted on the Zebra generators we showed that nontransparent implosion regime can be modeled in star arrays [Ivanov2010b]. In a "gated" star array configuration the innermost wires are replaced by wire pairs forming "gates" on either side of the array. The transparency of these gates could be toggled by changing the length and material of these gate wires, acting either as an open gate or a closed "trap" for the imploding plasma. Details of these experiments will be discussed further in this chapter.

The control of plasma flows can facilitate further studies. It might be possible to create rotating pinches [Veliklovich1995], and the principle may also be used in laboratory astrophysics experiments to study plasma bow shocks [Ampleford2010] and colliding plasma jets.

3.2. Calculating inductive current division in wire arrays

As described in the introduction, the current distribution within an arbitrary array can be calculated using an inductive current division scheme [Davis1997]. This scheme was coded and implemented to calculate current division in nested and star wire arrays in MATLAB, and the code itself is listed in the Appendix. In this method, a wire array is modeled as current loops consisting of an *i*-th wire and a *k*-th return current backpost of infinite length. The voltage drop over the load is the same for each current loop. As the load is assumed to be inductive, the voltage drop is determined by the rate of change of the magnetic flux Φ over each wire loop:

$$\mathrm{V} = \frac{\partial \Phi_{ik}}{\partial \mathrm{t}} = \frac{\partial \Phi}{\partial \mathrm{t}} = constant\ , \tag{3-1}$$

therefore $\Phi = constant$, i.e. the same for all the current loops. The total magnetic flux through a current loop *ik* is the sum of the contribution of all possible loops:

$$\Phi_{ik} = \sum_{j=1}^{N_w} \sum_{m=1}^{N_b} L_{ik,jm} I_{jm}\ , \tag{3-2}$$

where N_w and N_b are the number of wire and backposts in the array. The mutual and self-inductances $L_{ik,jm}$ (from loop *jm* on loop *ik*) of wire-backpost loops can be calculated as

$$L_{ik,jm} = \frac{\mu_0 h}{2\pi} \ln\left(\frac{r_{im} r_{jk}}{r_{ij} r_{mk}}\right) + \frac{\mu_0}{4\pi} \ln\left(\frac{2h}{r_{ij}} - 0.75\right) \delta_{ij} + \frac{\mu_0}{4\pi} \ln\left(\frac{2h}{r_{km}} - 0.75\right) \delta_{km}\ , \tag{3-3}$$

where h is the height of the load, and $r_{\alpha\beta}$ ($\alpha \neq \beta$) is the distance between the wires/backposts of the respective indices. If $\alpha \neq \beta$, i.e. $r_{\alpha\alpha}$, it refers to the radius of the wire/backpost with the index α. In this equation, the first term is the loop mutual/self-inductance, the second term is the self-inductance of the wire and the third term is the self-inductance of the backposts. The latter two terms can be neglected. At this point, eqn. (3-2) represents a system of linear equations with the $N_w \times N_b$ unknowns, i.e. the loop currents. The flux Φ can be chosen as arbitrary (e.g. unity) vector of size $N_w \times N_b$. The loop currents would be determined relative to each other, except of their magnitude, which can be calculated by normalizing to any total current.

The method was benchmarked by the inductive current division formula for nested arrays (eqn. 1-11) [Velikovich2002], and by comparing with another implementation of the method by S.N. Bland at Imperial College, London [Bland2009]. Benchmarking

comparison with the equation is shown in (Fig.14). As the equation is derived in the high-wire-number limit, it is inaccurate for low wire numbers. The main source of difference at high wire numbers comes from that the code does take wire self-inductance into account, while the equation does not, so the equation underestimates the current flowing in the inner array. One such current distribution is shown in Fig.14. for a 9-wire 3-ray star array.

# Wires	Code	Equation	Difference
8	0.3439	0.3445	-0.2%
16	0.2022	0.1994	1.4%
32	0.0790	0.0749	5.2%

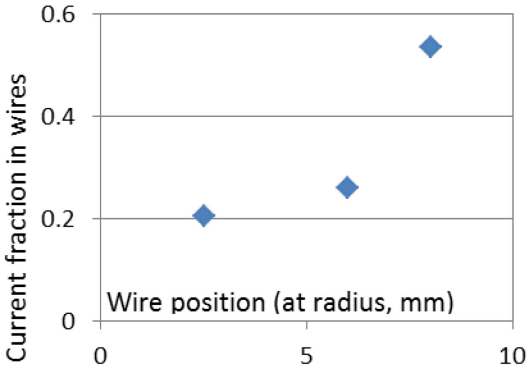

Figure 14. Benchmarking comparison with eqn. (1-11) of current fraction through the inner wires in 16mm outer and 8mm inner diameter nested arrays at 200μm radius (left). Current fraction in wires in a 16/12/5mmØ star wire arrays, based on inductance code calculation (right).

The numerical parameters used are representing the Zebra generator geometry. While the position and number of the return current posts can be changed, it was assumed that there is six return current posts arranged in a hexagonal pattern. Changes to the return current post positions had negligible effect on the current distribution. The six return current posts, each 2.22mm in diameter, are assumed to be at 42.9mm radius. Instead of the actual wire diameter, the diameter of the wire corona was used in the calculations, as the current goes through the expanded coronal plasma. Plasma column diameters assumed in the code were 0.4mm diameter for Al and 0.25mm for stainless steel.

The inductance matrix itself is close to singular, which results in a very low conditioning number. This causes observable numerical up to 1% - e.g. the total current fraction adds up to 1.01 instead of unity, or the current distribution is not being completely symmetrical even in 3 and 6-ray stars, which has the same rotational symmetry as the return current posts. With higher number of wires, numerical errors can increase further.

The formalism of the method is 2D, i.e. assumes infinite axial length, but the same principles can be used to calculate current distribution that take 3D effects (e.g. finite load length, current return from hardware and tilted wires) into account. It would require the mutual inductances to be integrated numerically, and self-inductance formulas changed accordingly.

3.3. Gated star and linear arrays

In ‘star wire arrays’ wires are arranged in star shape, that is, three or more radial rays, with each array containing three or more wires. The mitigation of plasma instabilities was observed in star arrays, and they produce reproducible, short, high-power x-ray pulses [Ivanov2009PRL]. The improvements can be attributed to the cascading implosion. The implosion starts at the edge wires and jumps from one wire to the next one. This process forms a smooth plasma column, re-sets the growth of instabilities, and limits the “trailing mass” – most of the array mass is collected in the stagnating pinch.

Such implosion in star and planar arrays is always “nontransparent”, as the moving plasma collides with the stationary wires located inside the array. Fig.15(a) shows a

shadowgram of the cascading implosion in a 3×6-wire star array (shot #2402), with the cascading implosion advancing from wire to wire. Fig.15(b) shows the interferogram of a somewhat similar implosion in a 6-wire linear array (shot #1840). The shadowgram of a 12-wire 16/8mm nested array (shot #1342) is shown in Fig.15(c). This array also implodes in the nontransparent regime. As seen on the latter shadowgram, the implosion on the inner array is somewhat delayed compared to the outer array, but the inner wires are already breaking up when the outer array starts to implode.

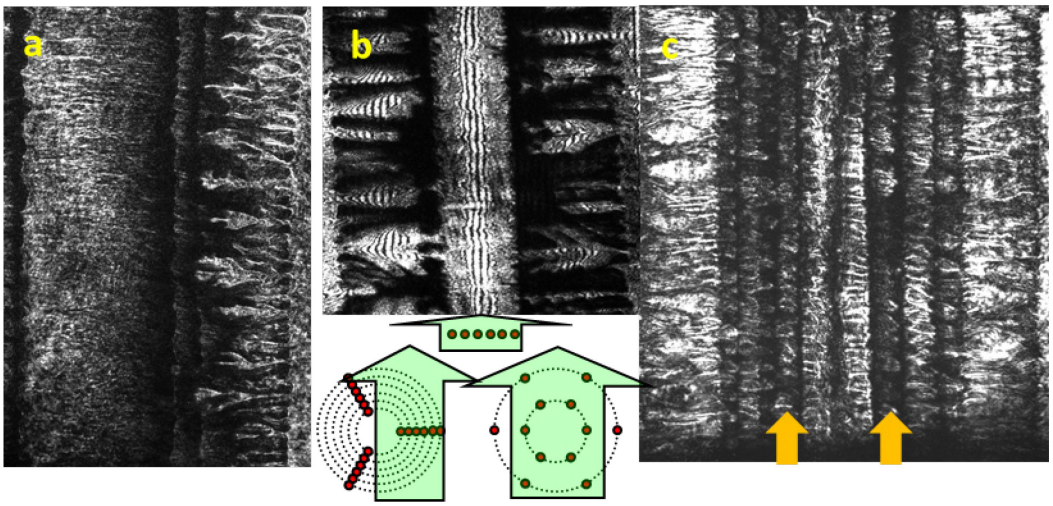

Figure 15. Shadowgram of a 3×6-wire star array, shot #2402 (a). Interferogram of a 6-ray planar array, shot #1840 (b). Shadowgram of a 12-wire 16/8mm nested array, shot #1432, with two inner wires indicated by arrows (c).

Gated star (and linear) arrays have the innermost wires replaced by wire pairs which are perpendicular to the rays, and form symmetric “gates” on the sides of the array [Ivanov2010b], as seen in Fig.16. As no wire blocks the way of the moving plasma, these arrays should implode in a transparent regime.

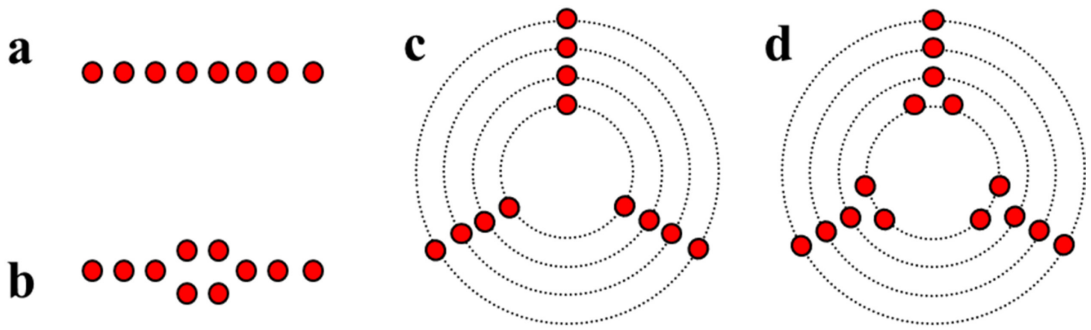

Figure 16. Gated and regular array configurations. Linear (planar) 8-wire (a) and linear 10-wire gated (b). 3-ray 12-wire star (c) and 3-ray 15-wire gated star (d).

Experiments were carried out with gated star (and linear) arrays, and were compared to star (and linear) arrays without gates. Several star and gated star configurations were tested, with arrays containing Al, Ti, Ni-Cr, Stainless Steel and W wires. Array linear masses varied between 19 and 100μg/cm. Fig.16 shows the schematics of selected star and linear array configurations. Array outer diameters of star arrays were 16mm, while the gates were placed at 5 or 6mm (inner) diameter. Linear arrays had 10mm width.

3.4. Current distribution in star arrays

The current distribution was calculated for 3-ray 12-wire gated star arrays, with single wires at 16 and 12mm diameter, and gate wires at 5mm. With 2mm gate width, 46% of the current is through the outermost wires, 26% through the middle wires and 28% through the six gate wires. Fig. 17 shows the current through the inner cylinder in these 3-ray stars as a function of gate width. The inner-cylinder current is higher in gated arrays than in regular star arrays (‘single wire’ in Fig.17), and it increases with the gate width. The current is higher than in the case of the innermost wire in non-gated star arrays, but not twice as much, as the mutual inductance of the close gate wires is high. Doubling the

wire length drops the gate current to about half, less than in the case of single innermost wires (Fig.17), which might account for the different implosion behavior – whether the gates function as traps or transparent gates. High-Z wire material, accounted by the

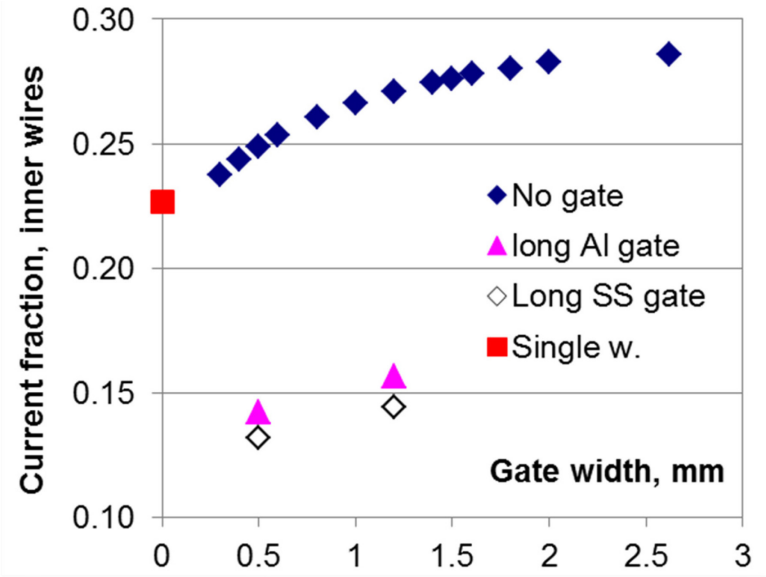

Figure 17. Calculated initial current division in 16/12/5mm gated arrays as a function of gate width.

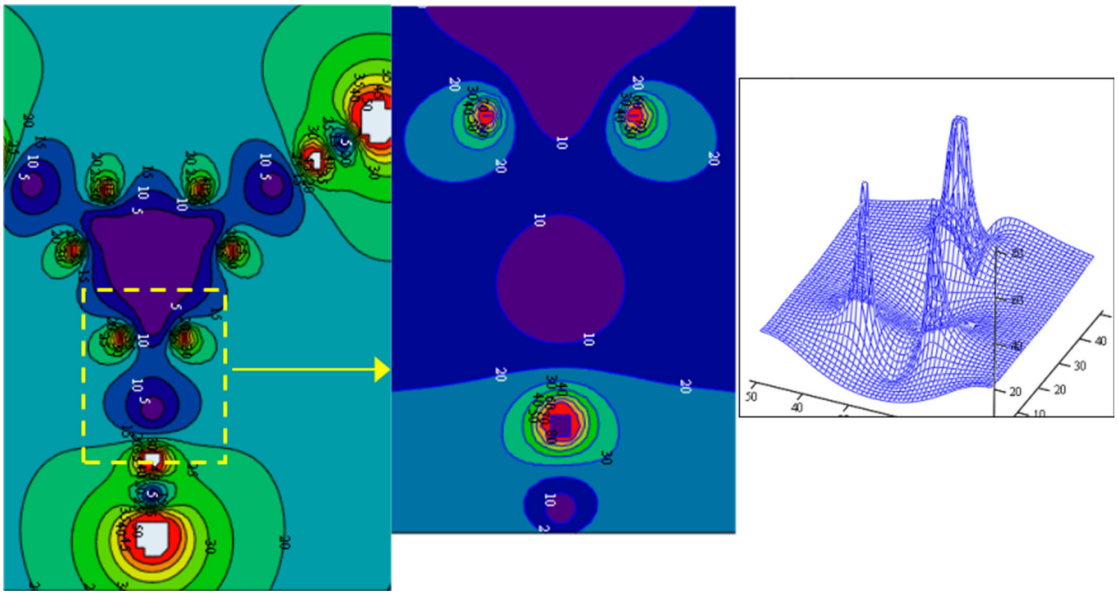

Figure 18. Magnetic field strength contour plot (left, middle) and 3D plot around gate wires in

plasma column diameter in the calculations, causes a 4% drop in the inner current compared to the regular diameter (i.e. Al) gate wires. Magnetic field structure around the gates is shown in Fig.18.

3.5. Nontransparent implosion in gated star and linear arrays

Gated star arrays show cascading implosion similar to regular star arrays, and replacing the innermost wire with a gate had no significant effect, neither on the x-ray yield nor the implosion dynamics. The implosion starts in a typical cascading mode, with the outer wires imploding into the inner ones [Fig.19(a)]. When the cascade reaches the inner gate wires, the plasma won't pass through the "gates". Shadowgrams show that the high current through these inside gate wires traps the imploding plasma, which forms plasma columns at the position of the gates [Fig.19(b)]. This trapping is present for gap width of 0.3-2mm. These plasma columns then implode to the center of the array. This is analogous to the "nontransparent" implosion mode of nested cylindrical arrays.

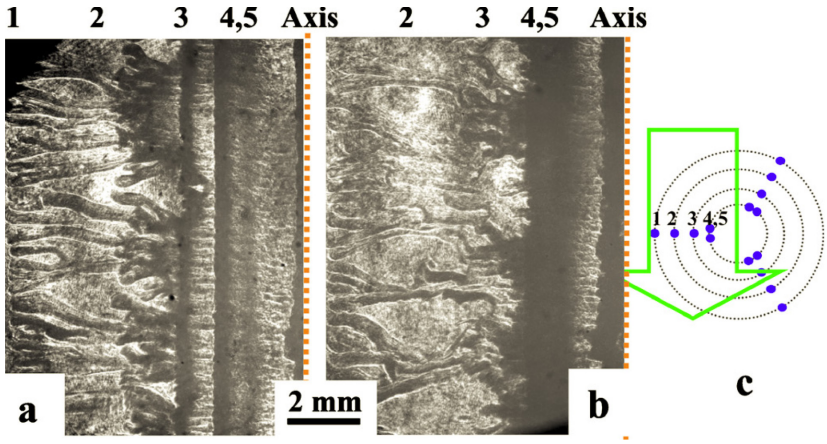

Figure 19: Cascading implosion in a gated star array (a), and the plasma trapping of the gates (b) for shot #1245, 15x10μm Al array. Numbers show original wire positions. The plasma column forms at the position of the gate wires (4,5). From [Ivanov2010b].

The cascading dynamics can also be seen in streak images of gated star arrays, shown in Fig.20 for two loads with 0.3mm and 0/8mm gate width. Outer wires implode into the inner wires that are moving at a small velocity. The implosion velocity in both star arrays is 180km/s, higher than the ablation velocities of 80-120km/s measured in cylindrical arrays [Harvey-Thomson2012].

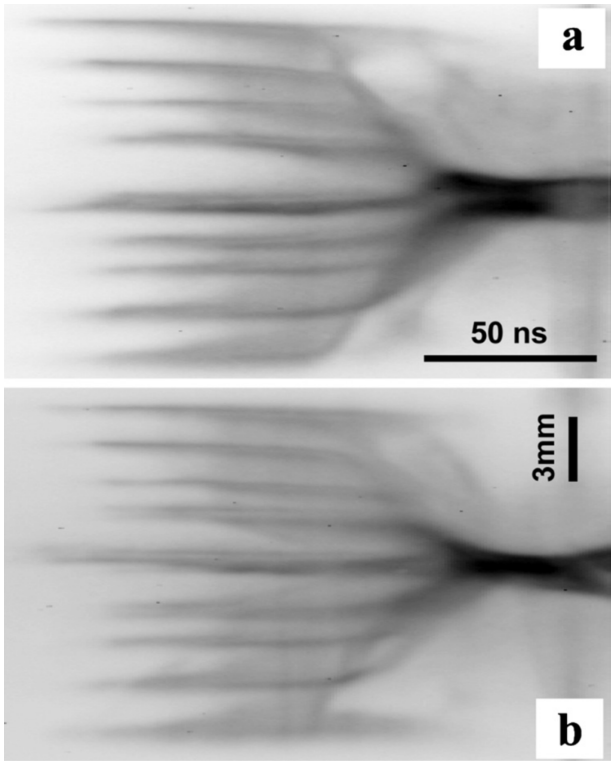

Figure 20. Streak-camera images of implosions in Al 15-wire star arrays Ø16/12/8/6 mm, with the gate widths of (a) 0.3 mm and (b) 0.8 mm. From [Ivanov2010b].

In the time-gated pinhole camera x-ray images of these implosions, high level of instabilities were observed in wire arrays with the 2mm-wide gates, but it made no observable differences to either the implosion dynamics or the x-ray yield (discussed later). Images of the z-pinch for narrower, 0.3-0.8mm gates showed a much more regular z-pinch, not different from the pinch of regular star arrays.

The implosion of gated star arrays was simulated by Dr. J. P. Chittenden of the Imperial College, London, UK, with the GORGON 3D resistive MHD code. The axial view of a simulation is presented in Fig.21. The simulation shows a nonprecursor implosion for this configuration, as the direction of **j**×**B** forces point outward at the gate wires. Shocks can also be seen where the ablating [Fig.21(c)] and imploding [Fig.21(d),(e)] plasma from the different rays collide. The trapping of the imploding

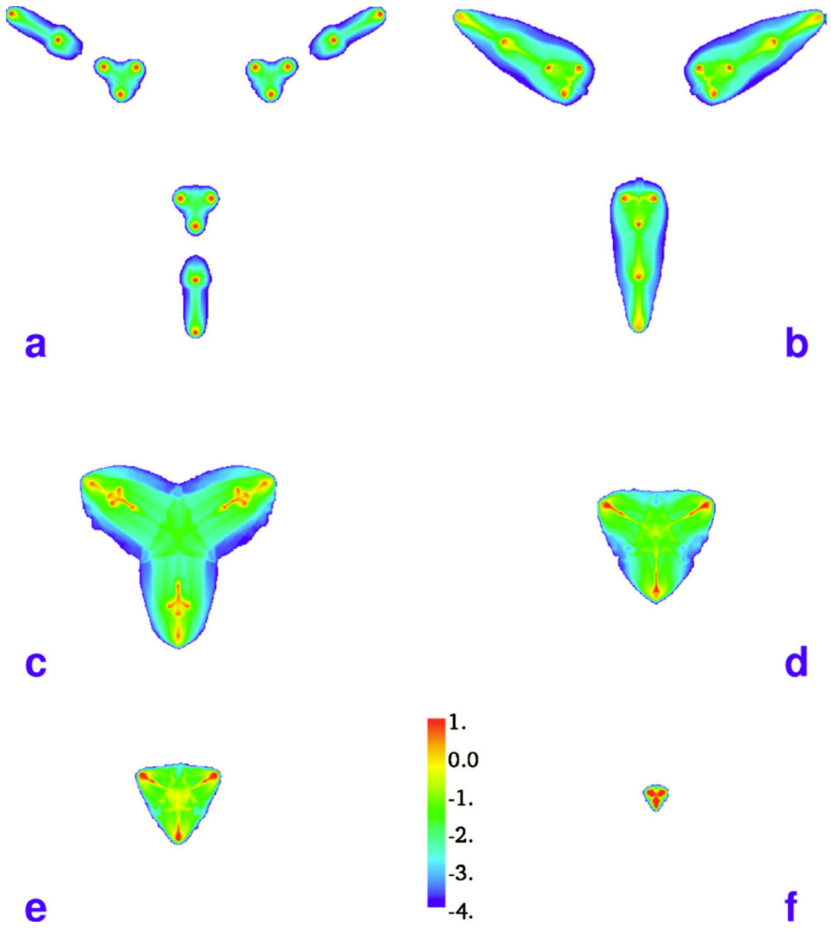

Figure 21. Top view of 3D resistive MHD simulations of the cascade implosion and trapping of the imploding plasma in Al star wire arrays, Ø16/12/8/6 mm with gates of width 1.2 mm. The timing of frames to the beginning of the current pulse is (a) 28 ns, (b) 53 ns, (c) 82 ns, (d) 88 ns, (e) 91 ns, and (f) 96 ns. The scale range is mass density from 10^{-4} kg/m^3 to 10 kg/m^3. From [Ivanov2010b].

plasma from the outer wires by the gates is clearly seen, as this plasma forms columns at the gate positions.

Results of this simulation were also compared with shadowgrams. It was found that some of the 3D plasma behavior was reproduced in simulations: plasma bubble implosion, cascading, plasma column merging and trailing plasma streams, and gate

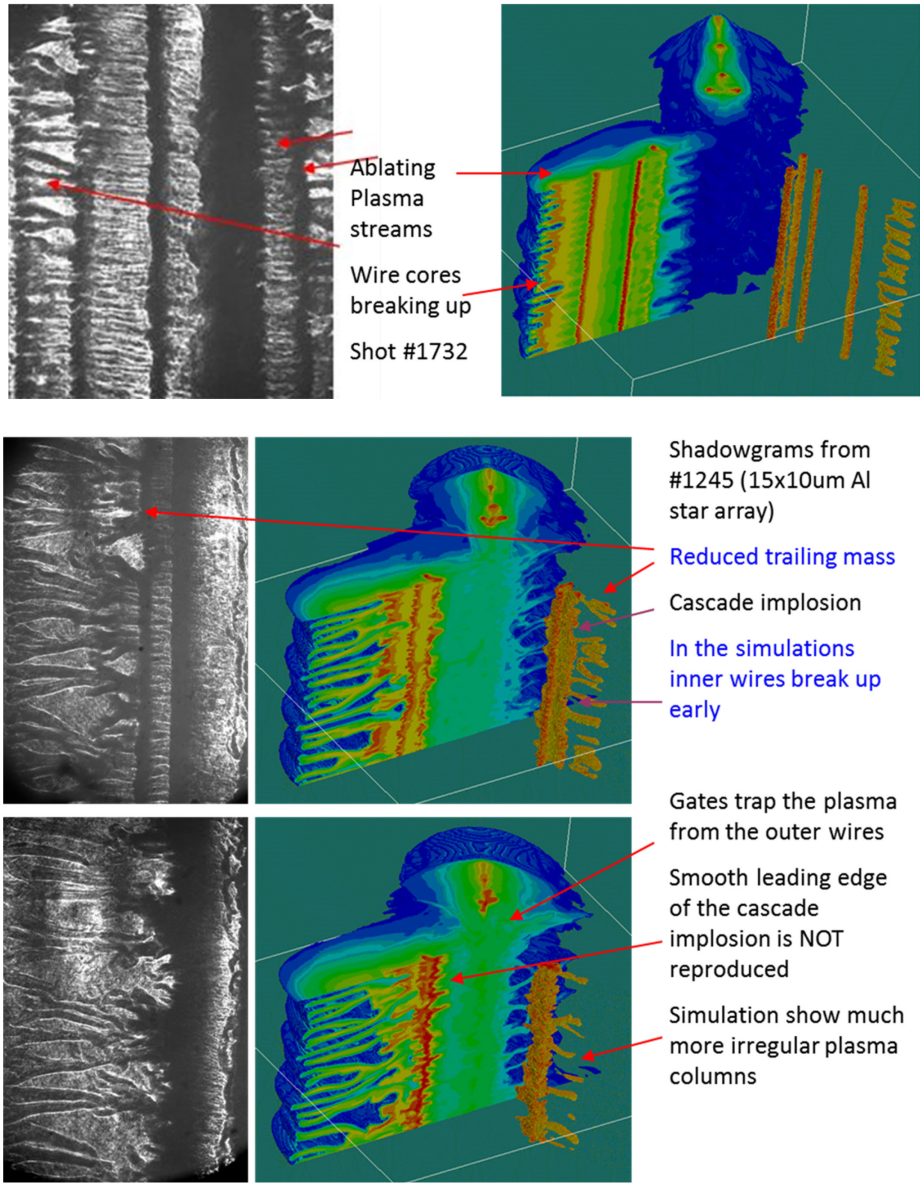

Figure 22: Comparison of the implosion dynamics in shadowgrams and Gorgon 3D MHD simulation, by J. Chittenden, Imperial College, London, UK.

wires trapping the plasma from the inner wires. The simulation, however, could not reproduce some key features of the implosion. The inner wires break up earlier, which can be attributed to the "hot start" initial condition of the simulation. The smooth leading edge of the cascade implosion is not reproduced, and much more irregular plasma columns are shown. Comparisons of the simulated images with experimental shadowgrams are shown in Fig.22. Overall, the simulations were in general agreement with the experiments.

3.6. Transparent implosion in star arrays

Gated arrays can also be used to simulate the "transparent" mode of implosion typical to nested cylindrical arrays [Cuneo2001]. Doubling the length of gate wires would increase the inductance of the gate wires, like in nested arrays [Bland2003], and decrease the gate current. The decreased magnetic field around these wires cannot trap the imploding plasma and allows it to pass through. Fig.23 shows the implosion in a gated star array with double-length Al wires, the drawing and the schematics of these loads. The plasma is impenetrable to 532nm laser, but 266nm resolves details in dense plasma. The plasma from the outer wires passes through between the gate wires, which stay at their original positions. The gates, however, are breaking up at some positions, and take part in the implosion, demonstrating a partially transparent mode of implosion (Fig.23).

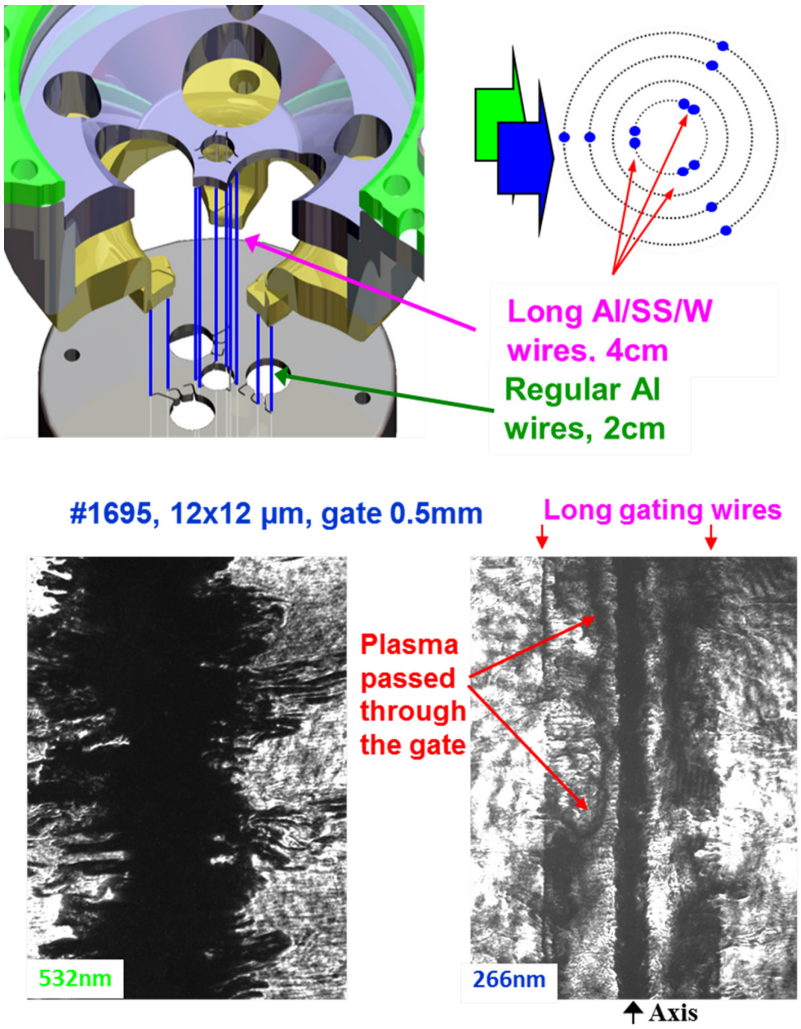

Figure 23:Drawing of load hardware with long gate wires (top left) and schematics (top right). Transparent mode of implosion at the gate wires, 532nm and 266nm (bottom left and right) shadowgrams of a gated array implosion, shot #1695, 12x12um Al array, mass 36ug/cm (long Al gate wires, 0.5mm gate width).

Besides increasing wire length, one further option was investigated to decrease the current in the gate wires. Wires with high atomic number would carry smaller amount of current in an array where the other wires are made of Al. This was confirmed by shadowgrams of linear arrays with Al [Fig.24 (a),(b)] and mixed materials, Al with Ti [Fig.24(c)] and Al with Au [Fig.24(d)] arrays. Linear arrays with equidistant wires [Fig.24(a)] demonstrate regular ablation of plasma and accumulation of plasma on the

center of the array, and the central area is opaque due to plasma already ablated to the axis. The implosion starts at the edge of the array and cascades to the inner wires and the center of the array.

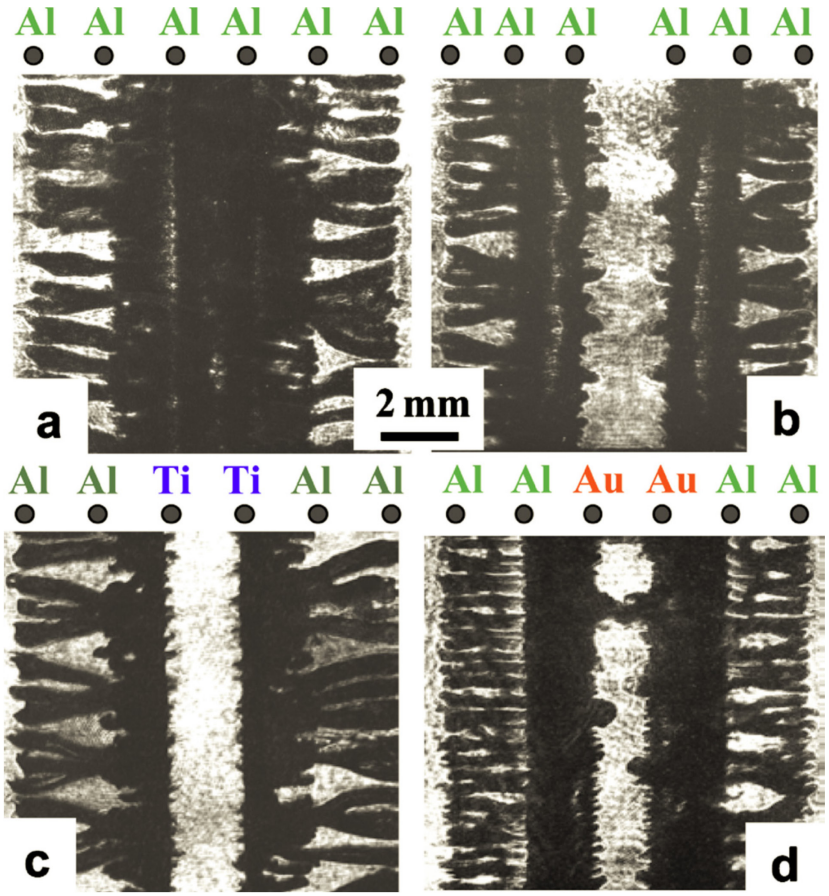

Figure 24. Shadowgrams of implosions in (a) and (b) six-wire Al and (c) mixed Al–Ti and (d) Al–Au linear arrays. Configuration of wires is presented on the top of shadowgrams. Delay of shadowgrams to the beginning of the current pulse is (a) 51 ns, (b) 47 ns, (c) 71 ns, and (d) 76 ns. All arrays are 10 mm in width. From [Ivanov2010b].

Introducing a larger central gap in the arrays, as seen in Fig.24(b), changes the implosion dynamics, as the **j**×**B** forces are directed away from the center, and thus the center remains free of precursor plasma for the ablation stage. When the Al wires in an equidistant array are replaced with Ti or Au wires, a nonprecursor implosion is seen [Fig.24(c),(d)]. This suggests that the current in the higher-Z wires is smaller than in Al

wires, if they were placed at the same location. The smaller current may be linked to the higher resistivity of the plasma, as Spitzer resistivity is higher for high-atomic number elements. Higher-Z wires also expand to smaller diameter plasma columns in the ablation stage [Ivanov2007b, Lebedev2000b]. Such a smaller plasma column has higher inductance and resistance. These factors decrease the current through plasma column of the inner wires, when at the outer wires it remains the same.

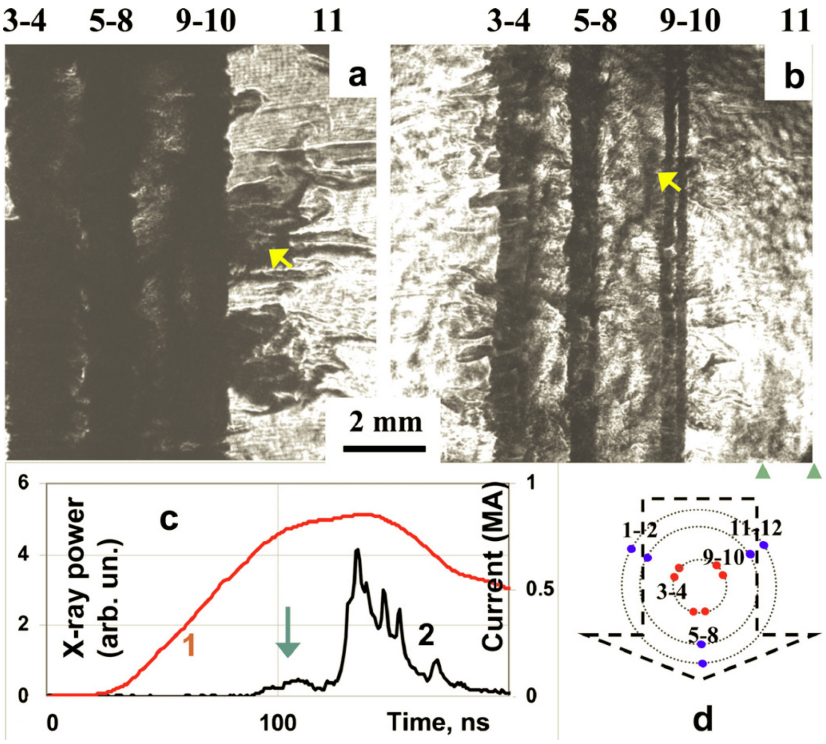

Figure 25. 532nm (a) and 266nm (b) shadowgrams of a Ø16/12/5mm star wire array with 6×10μm Al and 6×10μm stainless steel wires, with gate width of 0.5mm. Diagram (c) shows frame timing over the current pulse and the keV-energy x-ray emission recorded by a PCD with a 8μm Be-filter. Wire array configuration shown in (d). From [Ivanov2010b].

In order to produce a transparent implosion, the long Al gate wires were replaced by higher atomic number wires – W and stainless steel. The inductance and resistance are increased in the higher-Z plasma columns formed by these wires. The resulting smaller

current delays the implosion of the gate wires further, and these wires would break up later.

The implosion of an Al star array with stainless steel gate wires is shown in Fig.25. The 532nm shadowgram [Fig.25(a)] shows imploding plasma, and some of this plasma is already past the gates (between wires 5-8 and 9-10). The 266nm shadowgram [Fig.25(b)] shows the dense plasma structure. The plasma from the external wires (indicated by an arrow) passed through the gate wires. The plasma column from the stainless steel gate wires 3-8 and 9-10 are intact and at their original position. The timing diagram [Fig.25(c)] shows that there is a keV x-ray pulse at the same time with the frame, when the plasma reaches the axis. This (smaller) pulse is generated by the Al plasma from the outer wires imploding to the center pinch. The main x-ray peak is generated ~20ns later, by the implosion of the gate wires.

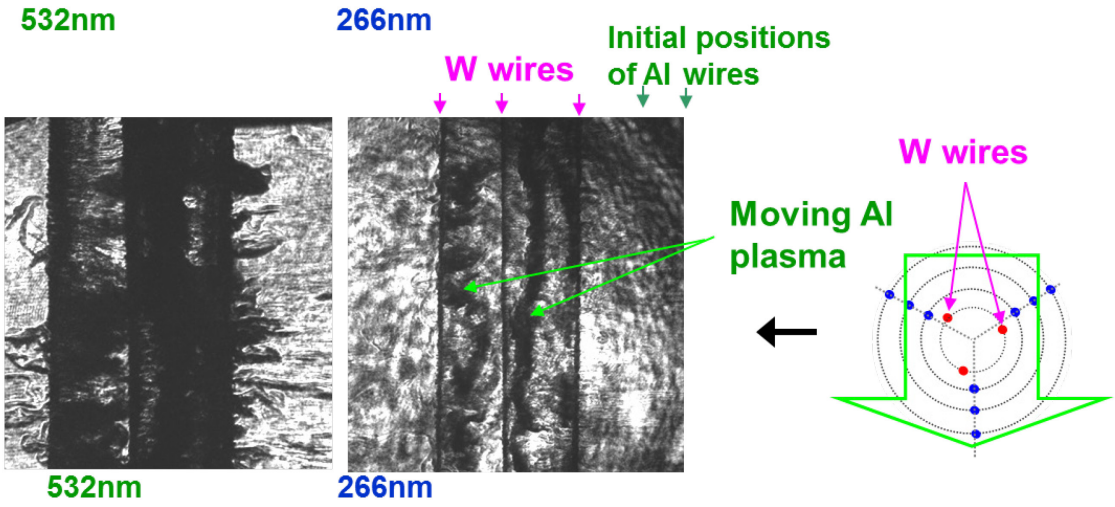

Figure 26: Transparent mode of implosion at the gate wires, Shot #1702. 9x10um Al wires, 3x7.6um W inner wires, mass 45ug/cm.

A similar effect was observed with arrays when only one of the (long) gate wires was in position. The single offset wires carry less current, and they don't trap the imploding plasma from the outer wires, but passes by them [Fig.26]. The Al plasma is more prominent in the shadowgram compared to Fig.25, as it was formed by 3 10μm wires in each ray, compared to only 2 wires in Fig.26.

3.7. The effect of gates on the x-ray radiative characteristics

Al linear arrays wires were compared to gated linear arrays of the same mass. Light loads had 8x17.8μm wires (52μg/cm) in the regular and 10x15.2μm wires (47μg/cm) in the gated arrays. Heavier regular arrays had 6x25.4μm wires, and heavy gated arrays had 4x17.8+4+25.4μm wires – both array had a nominal mass of 80μg/cm. As shown on Fig. 27, the gated arrays had similar total x-ray yield, peak power and K-shell x-ray yield as the corresponding (light or heavy) non-gated arrays. Gated arrays, however, had 10-15ns earlier implosion.

For 3-ray star arrays with 12×15μm or 15×13.5μm Al wires, the total x-ray yield and peak power was similar for all gate width, (Fig.28). Arrays with 2mm gates had 30-50% higher keV X-ray energy. Like in the case of linear arrays, gated arrays were 10-15ns faster. The earlier implosion of gated wires can be attributed to two effects. First, gated wires had lighter wires on the outside, and they are heavier only on the innermost wires. Based on the 0D model for cylindrical arrays, where implosion speed scales as $1/mr^2$, as given by eqn.(1-5) :

$$\frac{\hat{m}}{2\pi r}\ddot{r} = -\frac{\mu_0 I^2(t)}{8\pi^2 r^2} \quad .$$

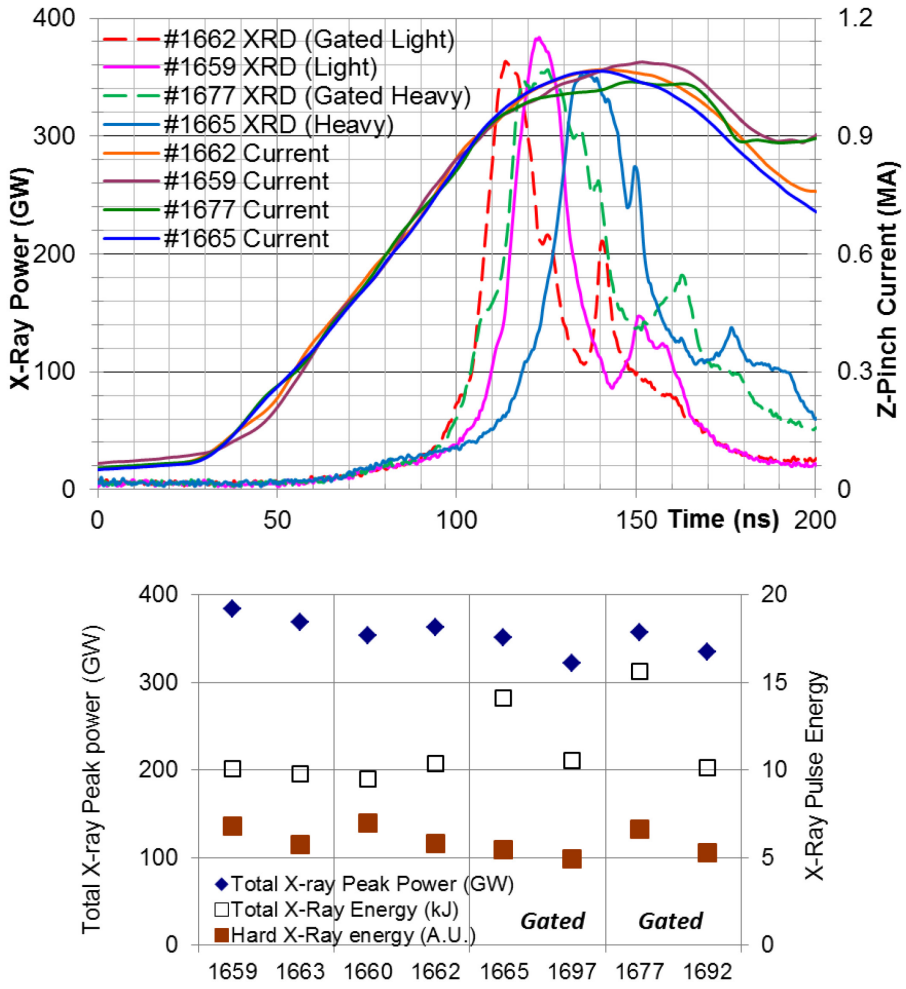

Figure 27. Soft X-ray (XRD with 2µm Kimfoil filter) pulse shape of gated and regular linear arrays, for heavy (80 µg/cm) and light (50 µg/cm) load masses (top). Pulse x-ray energies for the same linear loads (bottom).

For same array mass, a mass distribution that is light on the outside results in a faster implosion. Second, current distribution calculation shows that gated loads had higher current on the inside. This produces a higher magnetic field inside the array, which also accelerates the implosion.

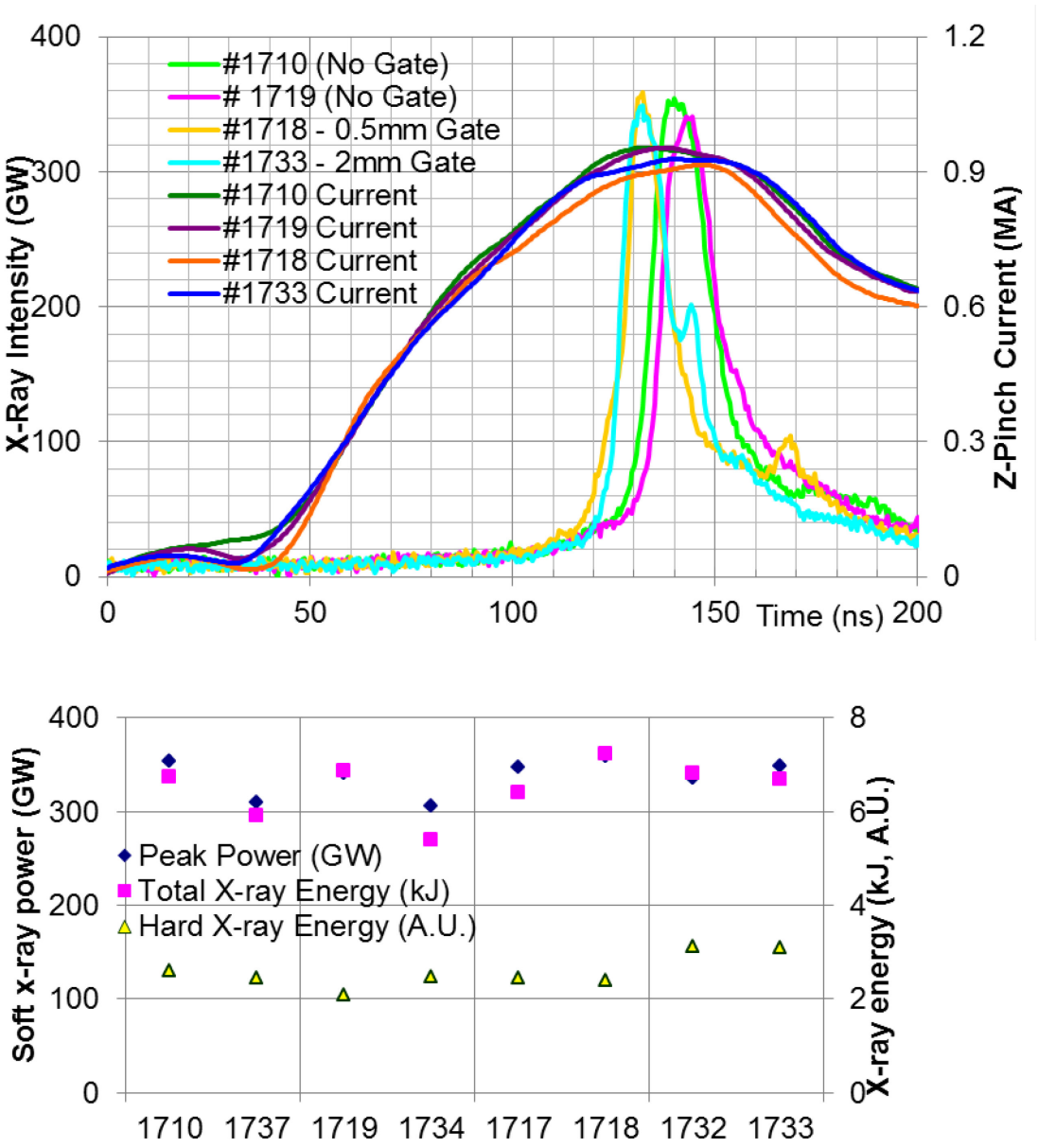

Figure 28. Soft x-ray (XRD) pulse shape for similar gated and regular star arrays (top). Load mass is 42-45μg/cm. X-ray pulse energies for the same loads (bottom).

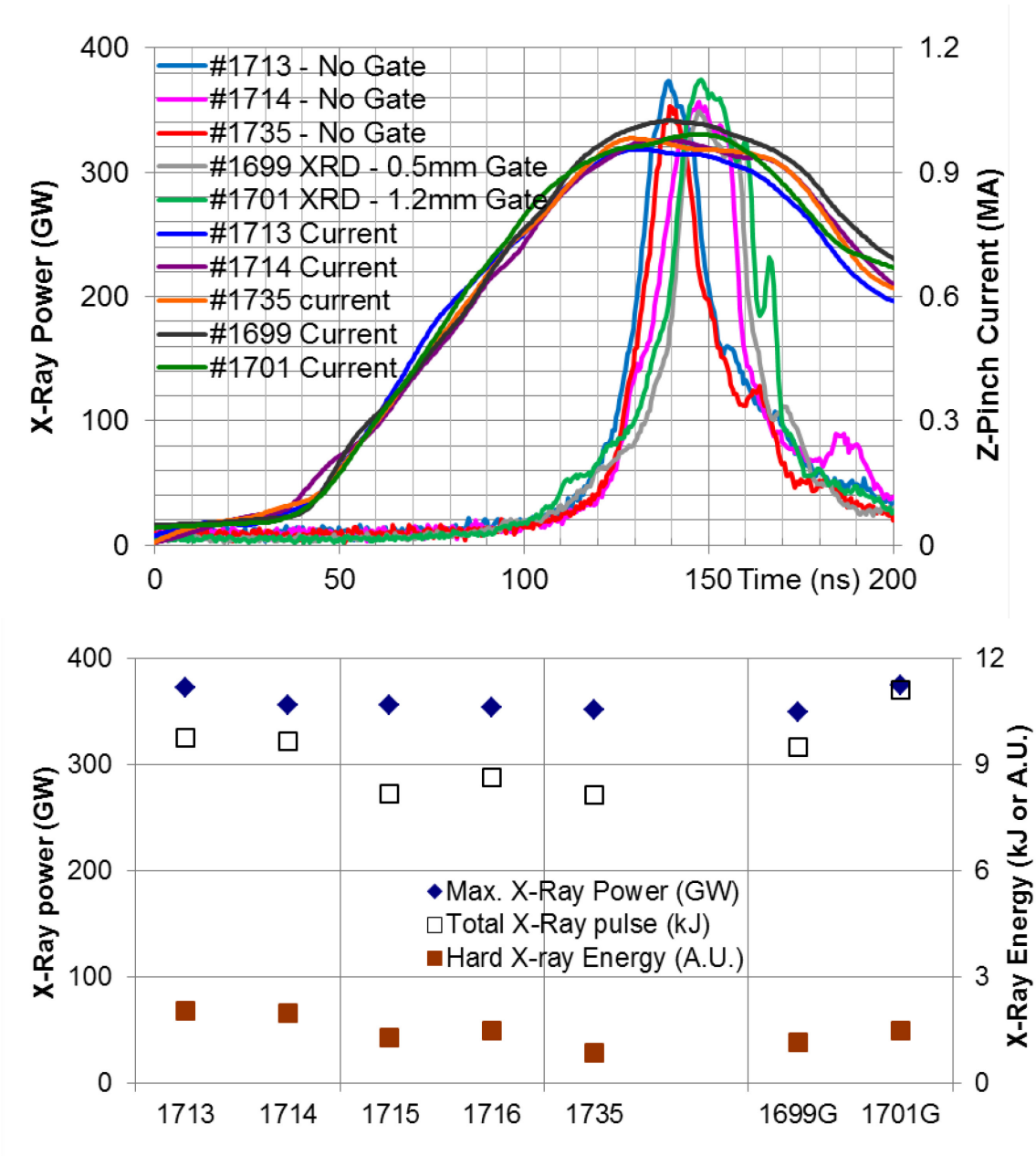

Figure 29. Soft x-ray pulse shape for star arrays with stainless steel ('SS') inner wires (top). X-ray pulse energies for the same loads (bottom).

Shot#	WireØ (μm) and configuration	Mass (μg/cm)
1713,1714	6x13.5Al+3x10SS	41.9
1735	6x10Al, 3x12.7SS	42.6
1699	6x10Al+6x10SS 0.5mm gate(long w.)	49.8
1701	6x10Al+6x10SS 1.2mm gate(long w.)	49.8

Table 1. Wire array configurations for investigated Aluminum/Stainless steel wire arrays

The x-ray yield and pulse shape for loads with stainless steel inner wires was also compared between regular and gated loads of similar mass (Table 1). Gated loads had long stainless steel gate wires. As seen in Fig.29, no effect was observed in the x-ray yield. Long gate wire star arrays had later implosion than the regular star arrays, contrary to the behavior of loads with regular gate wires. This should be attributed to the fact that loads with long gates were somewhat heavier than the regular loads. This is enhanced by the lowered inside magnetic field in the long gated arrays, as less current passed through the long gate wires.

3.8. The possibility of rotating pinch

The experiments with nontransparent and transparent implosion regimes shows that the imploding plasma flows might be redirected from the radial direction. Gated star arrays provide a form of plasma flow control in the array. Gate wires of regular length trap the plasma, but longer gate wires act transparent to the plasma from the outer wires. When only one of the long gate wires was left, the offset wire did not trap any plasma, most probably due to the low current through it. In this case, however, the offset wires produce a radial component to a magnetic field, which would produce an azimuthal

component in the **j**×**B** force, and thus induce rotation in the array. Azimuthal **j**×**B** forces that are necessary for rotation can also be found in twisted conical arrays, which rotate according to MHD simulations [Ampleford2007].

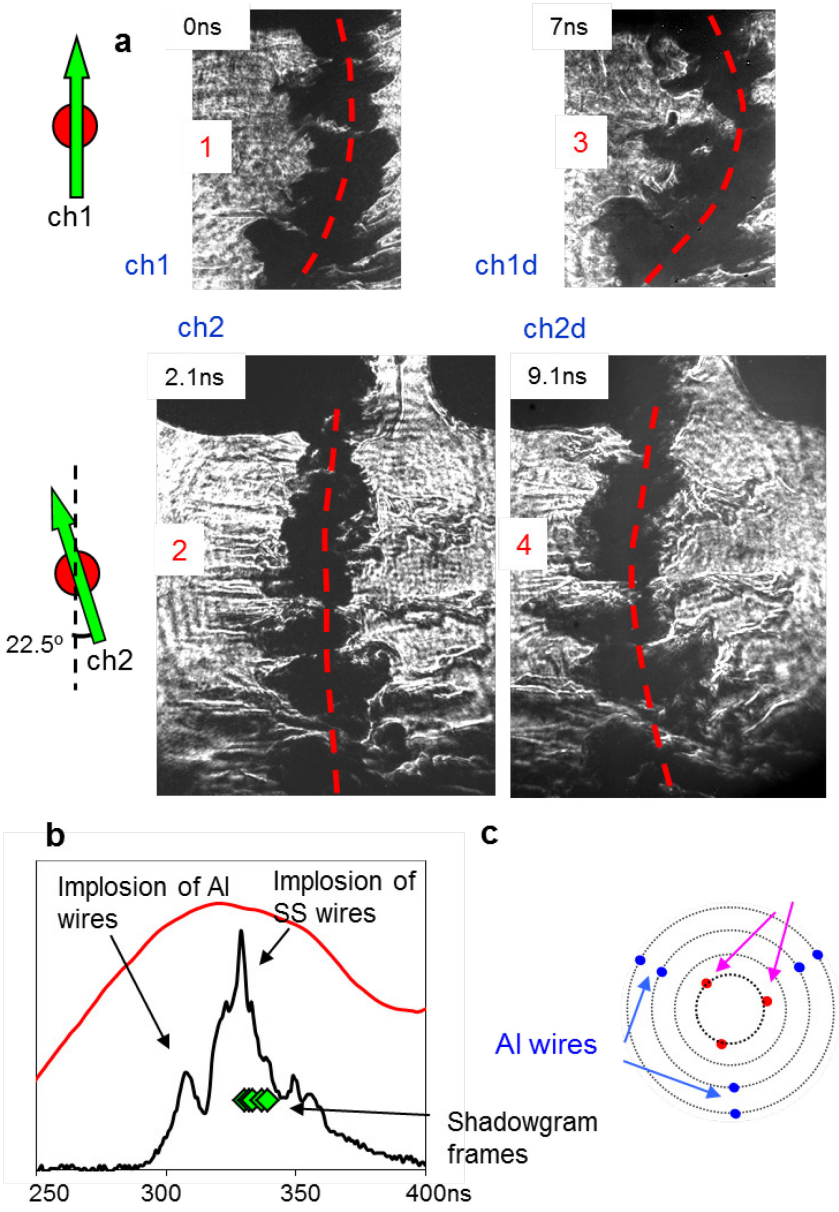

Figure 30. 4-frame shadowgram, stagnating pinch of a "shifted" star wire array (a), #1703, with 3×10μm stainless steel inner wires and 6×12μm Al wires. Shadowgram frame timing diagram with keV x-ray pulse (b), and array schematics (c).

Rotation in the imploding plasma should stabilize the pinch [Velikovich1995]. In particular, a rotating hollow plasma shell is stabilized for the m=0 Rayleigh-Taylor ("sausage") instability through the effect of centripetal acceleration on the pressure balance of the pinch, although it does require very high rotational velocity, similar in magnitude to the implosion velocity, i.e. 100km/s [Velikovich1995]. On the other hand, this would reduce the compression and energy density of the pinch. The rotation would also create an azimuthally sheared flow, which has further stabilizing effect [Sotnikov2002].

Fig.30 shows two-frame shadowgram of the final pinch of such a wire array. The pinch itself bends, which is an uncharacteristical behavior of the pinch, and was only seen in this wire array. It is possible that the emphasized bending of the pinch in the later frame is the effect of rotation.

Considering the wire array itself, the net angular momentum of the pinch would be zero, but sheared flow would be possible – by a core and outer region of the pinch rotating opposite directions. Some of the angular momentum, however, might transfer to the current carrying structure of the chamber, resulting in a net rotation in the plasma.

To determine the presence of rotation - or plasma flow with azimuthal component – two-frame end-on probing of the pinch is necessary. Diagnosing rotation with side-on probing is not conclusive. For example, even in the case of in twisted conical arrays [Ampleford], where azimuthal $\mathbf{j}\times\mathbf{B}$ forces are present, there was no clear experimental identification of rotation with end-on probing.

Single-frame end-on (i.e. axial or vertical) probing was used previously on cylindrical wire arrays [Lebedev1998a]. End-on imaging probing offers azimuthal instead of axial resolution, and its inherent advantage over side-on probing is that the probing direction is parallel to the axis of symmetry of the load, and that the field of view is not blocked by plasma streams. The main disadvantage of end-on probing is that the plasma areal densities are an order of magnitude higher, which limits probing beam to lower densities. 532nm end-on probing interferometry was used to study the ablation of cylindrical wire arrays at the Magpie generator [Lebedev1998PRL], and two-frame probing at the same wavelength can be used in the early implosion stage [Papp ICOPS2010 poster]. Single-frame 355nm end-on UV probing was used for interferometric imaging in the ablation phase [Swadling2011] and Thomson-scattering measurements [Harvey-Thompson2012]. End-on x-ray backlighting with x-pinches was used on the COBRA generator to study ablation in non-imploding wire arrays [Blesener2009].

3.9. 532nm end-on probing on the Zebra generator

For the study of the azimuthal development of the pinch, end-on probing setup was developed. Hardware modifications were designed using the ProEngineer (now Creo) CAD software. The hardware itself was machined and assembled in the machine shop of the Nevada Terawatt Facility. The drawing of the setup with the hollow cathode is shown on Fig.31.

The probing beam enters the chamber from above, passes through holes in the load hardware, and the imploding pinch. The beam is reflected by a 25.4mm diameter Al-coated mirror, then passes through the anode-cathode gap and exits the chamber. A glass

slide over the mirror prevents premature plasma formation on the mirror. The mirror itself is single-use, being destroyed by the x-ray radiation of the pinch and the impact of plasma after the implosion. This setup otherwise used the existing EKSPLA diagnostics beamline and delay line without significant modifications.

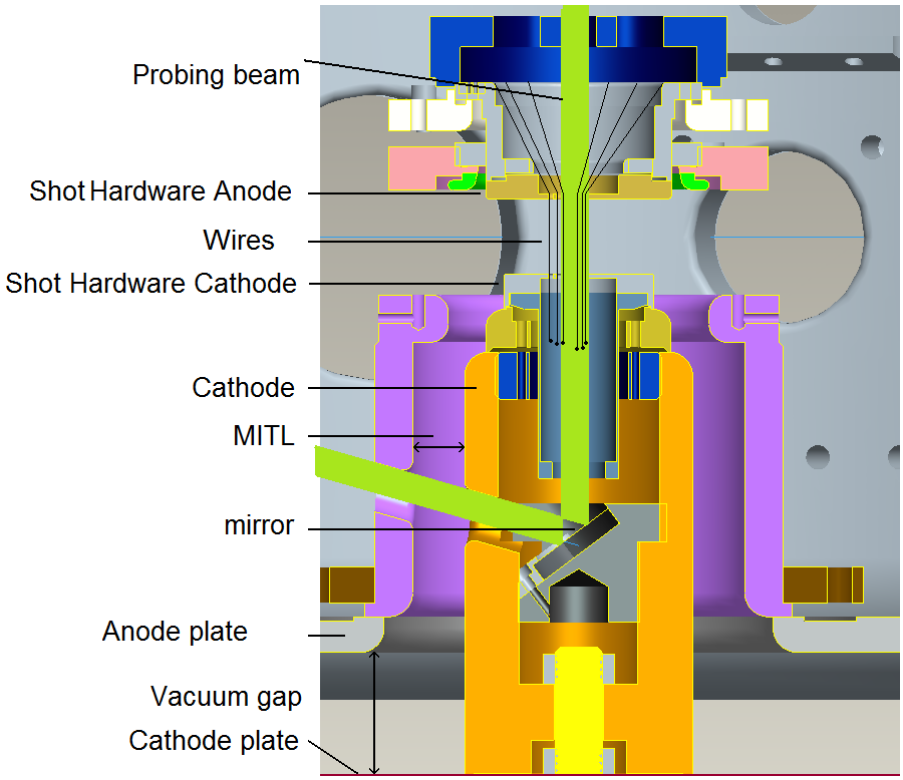

Figure 31. Schematics of load with the end-on probing setup. Drawing of the target chamber with a load installed.

End-on probing of cylindrical arrays showed a split in the ablating plasma streams (Fig.32). Shocks formed at the collision of neighboring plasma streams can also be discerned. Furthermore, the central precursor showed hollow characteristics, which was also reported by XUV self-emission [Bott2006]. The probing beam, however, was unable to penetrate into the dense plasmas during the implosion phase, and its usefulness for studying the final pinch is thus limited.

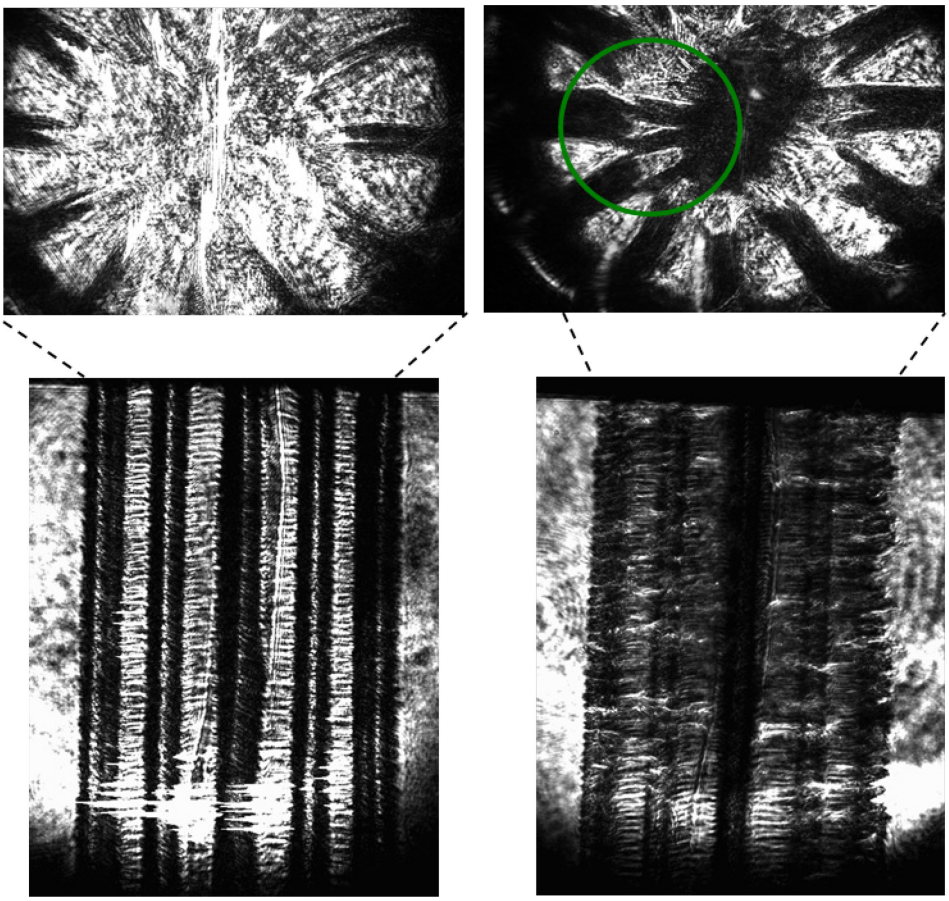

Figure 32. End-on and side-on shadowgrams of a 12×10μm Al cylindrical wire array, Shot #2183. Frames top and below were taken at the same time. Frames on the right are after a delay of 19ns.

3.10. 266nm end-on probing results

To probe higher density plasmas, the end-on probing setup was modified to work at 266nm wavelength. Optical elements were changed to ones working at 266nm. A new beamline was built after the chamber to the CDD cameras. Furthermore, a delay system was designed and built for the UV probing beam that was located in the EKSPLA laser room. The scheme for the setup is shown in Fig.33. The laser beam is split by a beamsplitter to two beams of similar intensity. The regular beam goes through a half-wave plate that is aligned to the provided P-polarization. The delay beam is merged into the regular beam on a Brewster-angle polarizer that reflects only the S component of the

delay beam. The length of the delay beampath is variable to provide a delay of 3-7ns between the two frames of orthogonal polarization. The resolution of the end-on imaging system was measured to be 10-16μm, determined by USAF resolution plate pattern.

The setup was used for end-on probing of shifted 3-ray star arrays and a gated four-ray star array (Fig.34). The array height was reduced to 10mm in order to decrease the plasma thickness and absorption. The shifted star arrays had all the rays shifted 1mm so the rays were pointing off-center, which provides a radial component to the magnetic field. The array was expected to implode along the rays, inducing rotation in the imploding plasma. The outer wires were 6-9 10μm Al wires, while the inner wires were 5-7.6 μm W and had double length (20mm).

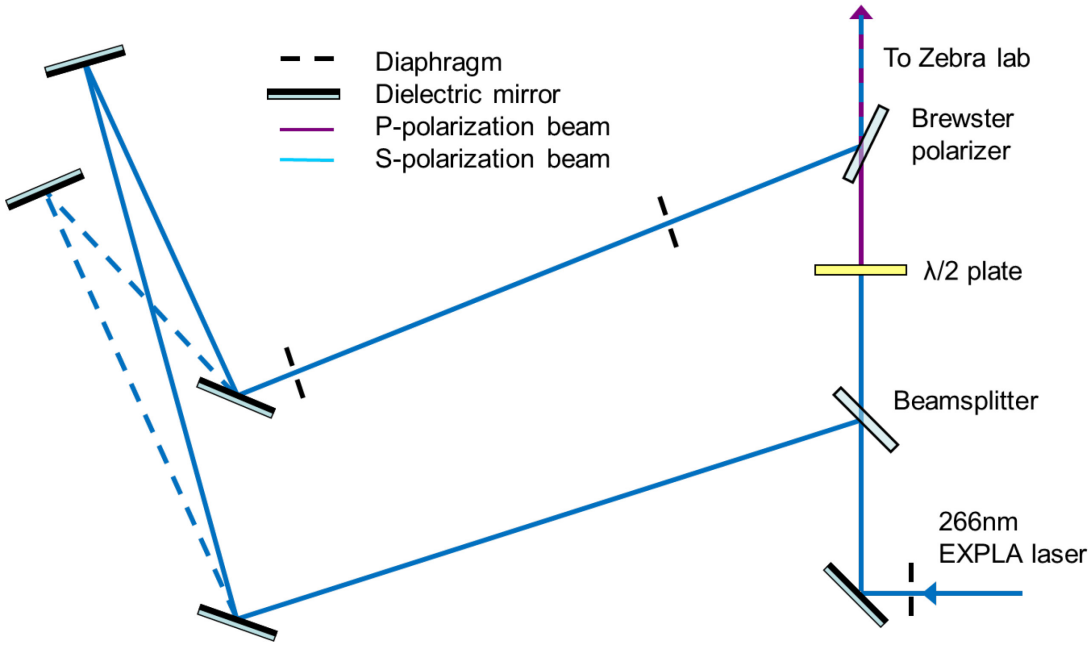

Figure 33. The delay scheme for the UV laser beamline.

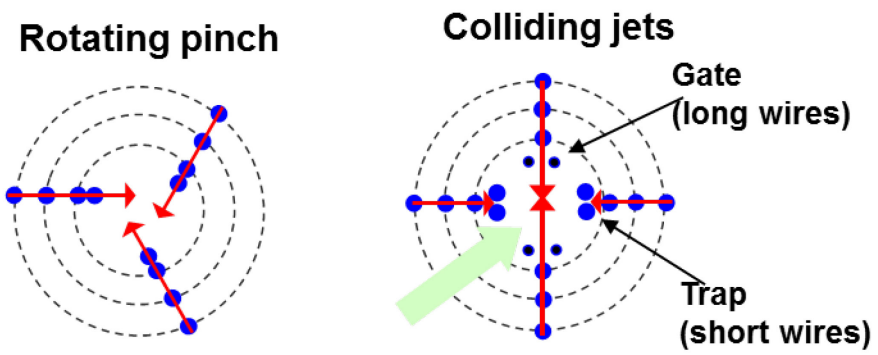

Figure 34. Shifted star array configuration (left), and colliding jet array with "trap" and "transparent" gates.

The 4-ray star arrays had outer Al wires and gates of W wires of similar size. Two facing gates were with long (20mm) wires that would be transparent to the imploding plasma, while the other two gates were short (10mm) so they would act as "traps". Ideally, plasma from the rays with a "trap" or "gate" would arrive at the center at different time and would be distinguishable from each other.

The results for the shifted arrays were inconclusive. The pinch itself, however, was evolving too irregularly, and it could not be determined if the pinches were rotating. The plasma of the outer Al wires, however, was passing by the three W wires, as seen in Fig.35(a),(b). The plasma passes clear of the inner wires, to the right of the W wire in the middle of the shadowgrams (Fig.35(a).(b)], i.e. the implosion is directed toward the center, not off-axis. The inner wire did not take part in the cascade implosion, unlike it is suggested in the scheme of Fig(34). Instead, the implosion is similar to the transparent mode in star arrays with a single offset wire in each ray, but does not offer a confirmation of any large-scale rotation in the pinch. That the strong absorption in the pinch in end-on probing [Fig.35(c),(d)] does not allow the resolution of the plasma details, so identifying

rotation would be difficult. This is complicated further that it was found that very fast plasma motion is present in the stagnation phase [Ivanov2011b].

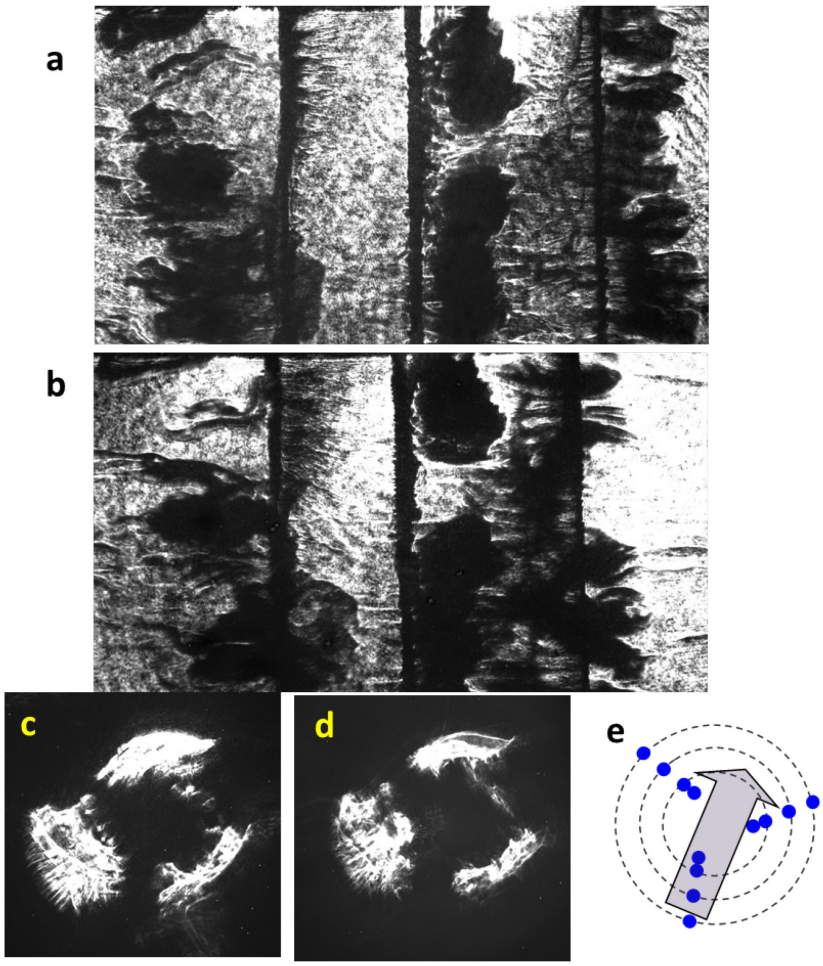

Figure 35. Side-on (a,b) 532nm probing for Shot #2643, and end-on 266nm probing for shot #2642 (c,d). Side-on probing beam direction is drawn in (e). The delays between frames a-b and c-d are 6 and 7ns. Load configuration is the same, 9×10μm Al outer wires and 3×6.4μm inner long W wires. The three distinguishable wires in (a) and (b) are the innermost W wires

For the 4-ray gated stars, the trapping effect could not be discerned from the limited number of experiments (Fig.36). One of the main difficulties was to find the correct neutral density filters to attenuate the beam before the CCDs, due to widely varying absorption in the plasma, as the plasma density on and around the axis of the pinch (and absorption through it) varies strongly in time. A quartz slide was also placed over the

mirror in the cathode [Fig.31] to protect it from early soft x-ray radiation. Some plasma did form on the protective slide, although that plasma could be penetrated, it offered further absorption, the effect of which was unpredictable. Frames at different stages of implosions thus required different neutral density filters to match the sensitive range of the CCD cameras.

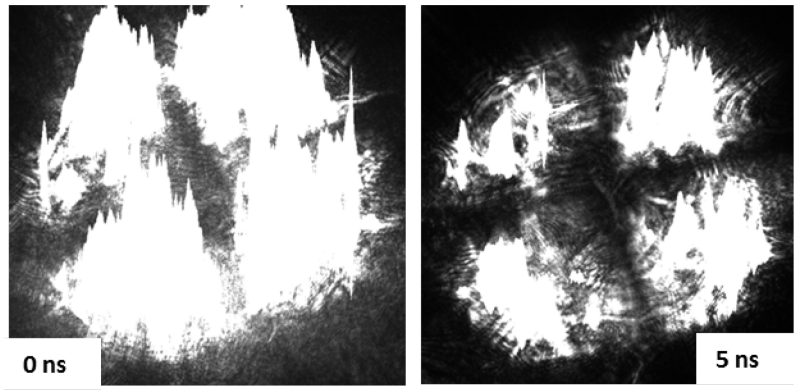

Figure 36. End-on UV probing of a colliding jet configuration. Shot #2727, 8×10μm Al outside and 8×5μm W gate wires.

The two-frame end-on UV probing beam, however, was able to fully penetrate a stagnating Z-pinch Al plasma (Fig. 37) in ZEBRA shot #2723. The load used was a 12mm diameter cylindrical 8x12.7μm Al wire array of 27.6μg mass. The height of the load was reduced from 20mm to 10mm to increase transmission through the plasma. As seen on fig.37, the intensity of the laser penetrating through the pinch was significantly larger than both the CCD dark current and the scattered light in the background, indicating penetration of the pinch with a transmission of ~5%. The density of the pinch was estimated to be 0.5mg/cm^3, assuming half the array mass is in the pinch. The electron density was estimated to be $n_e \sim 10^{20}$ cm^{-3} at an ionization of Z=11.

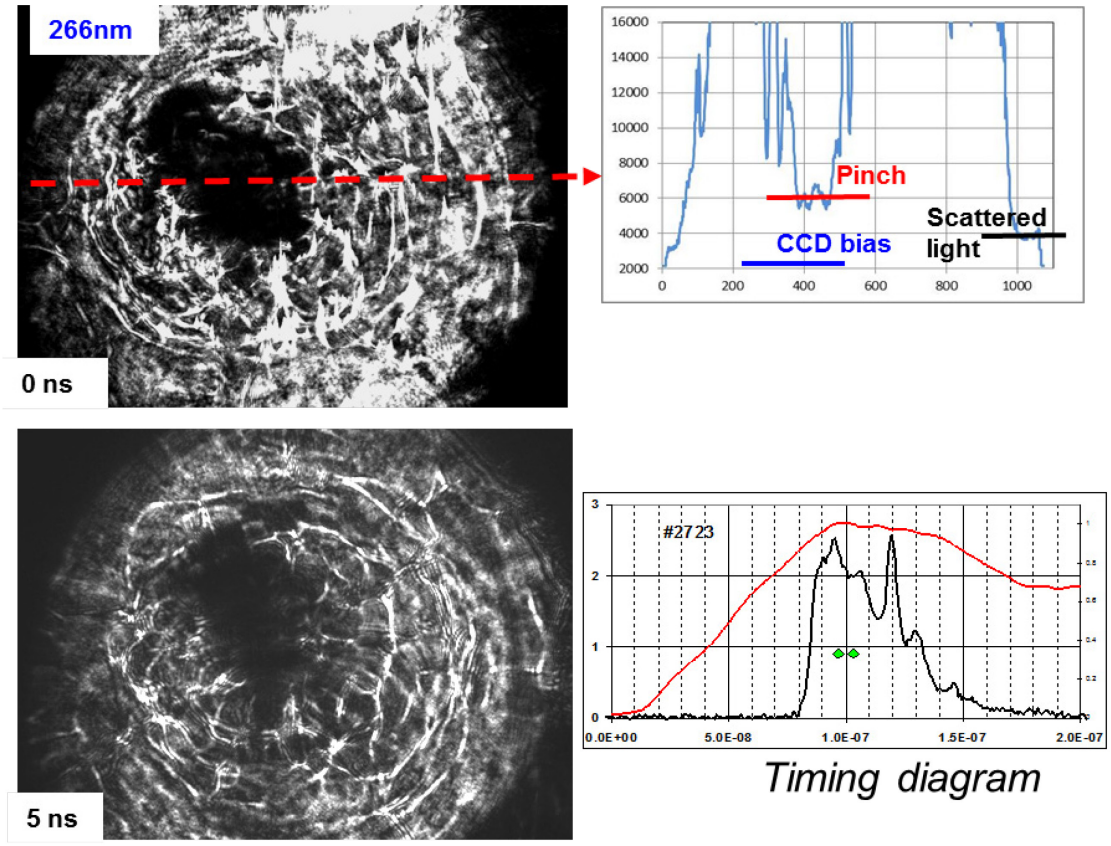

Figure 37. End-on UV two shadowgraphy of shot #2723, 8×12.7μm cylindrical array (left, top and bottom); CCD intensity profile showing the nonzero transparency (top, right) and timing diagram (bottom, right).

These results show that it would be possible to study dense plasmas with end-on probing on the Zebra generator, although the fast plasma motion found in the pinch [Ivanov2011b] made it difficult to identify rotation. End-on Faraday imaging diagnostics could also provide information of magnetic field convection/compression in such experiments.

In the MagLIF experiments proposed on the Z generator at Sandia National Laboratories, a cylindrical metal (Be) liner is imploded within an axial magnetic field of over 10T [Slutz2010]. On the inside of the liner there is a cryogenic hydrogen (D-D or D-T) layer and gas fill. The gas fuel fill is preheated by a 5-10kJ laser pulse to 100-

500eV temperatures. The imploding liner compresses the magnetic field with the gas fill, and heats up the fuel. Numerical simulations predict that with the pre-magnetized pre-heated fuel significant fusion yields – over the physical breakeven - can be achieved.

Such experiments would require the measurement of the magnetic field inside the liner, which provides significant challenges. For example, B-dot microprobes could be used only at lower convergences as the increasing magnetic field can induce voltages of several thousand volts and break through any insulation.

Faraday imaging diagnostics using axial probing provides a method for such magnetic field measurements. 266mn probing, as seen in Fig.36, can penetrate hot (over 200eV) Al plasma of 0.5 mg/cm^2 areal density, with a corresponding electron density of ~10^{20}cm^{-3}. These parameters are similar to the gas fill in the proposed MagLIF experiments (3mg/cm^3) at Sandia National Laboratories, so laser probing of the liner would be possible.

Deep UV probing with even shorter wavelength offers the possibility of probing the compressed fuel to higher densities. Such lasers are available, e.g. Nd lasers operating at the 5th harmonics at 211nm, or commercially available excimer lasers operating at 157nm. The critical plasma density is 1.6×10^{22} cm^{-3} at 266nm, increasing to 2.5×10^{22} cm^{-3} at 211nm and 4.5×10^{22} cm^{-3} at 157nm. The absorption due to inverse bremsstrahlung also decreases with increasing frequency. Fig.38 shows the transmission of a probing laser beam at these wavelengths, in hydrogen plasmas of 300eV and 1keV temperatures.

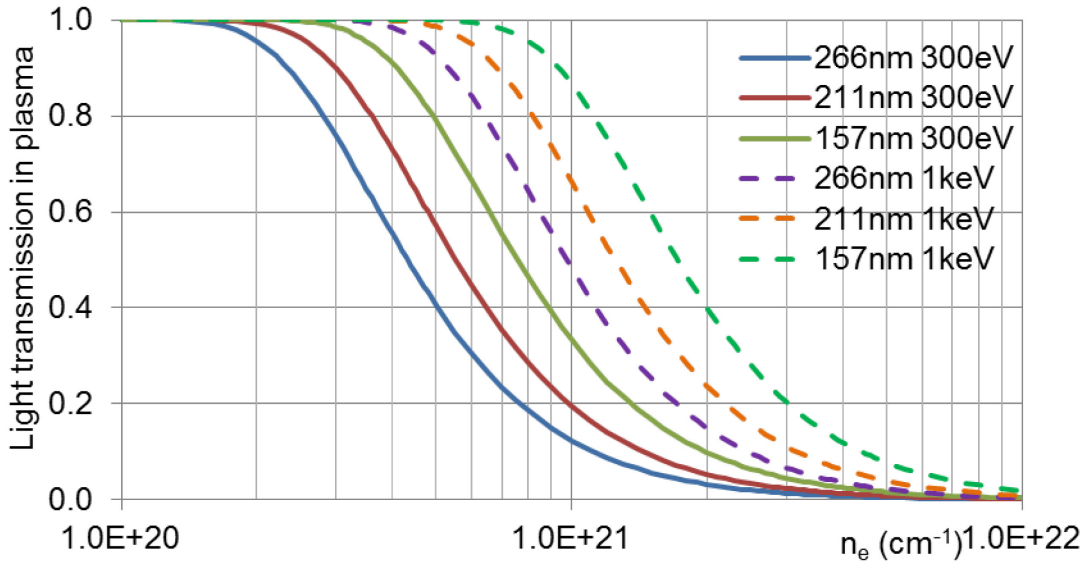

Figure 38. Transmission through a 1cm thick hydrogen plasma at two different temperatures for UV and deep UV laser wavelengths. Absorption was calculated from inverse Bremsstrahlung, formula given in eqn. (2-6).

The evolution of the fuel density and magnetic field, simulated for one set of starting parameters (and a deuterium gas pre-fill of 3mg/cm^3) is shown in Fig.39. The plasma can be penetrated for a significant time of the liner implosion, and during this time imaging Faraday diagnostics can deliver information on the magnetic fields within the liner during the initial stages of the implosion. Reducing the gas fill to 0.5mg/cm^3, while not optimal for fusion yield, would allow probing later stages, up to around 140ns of the implosion time.

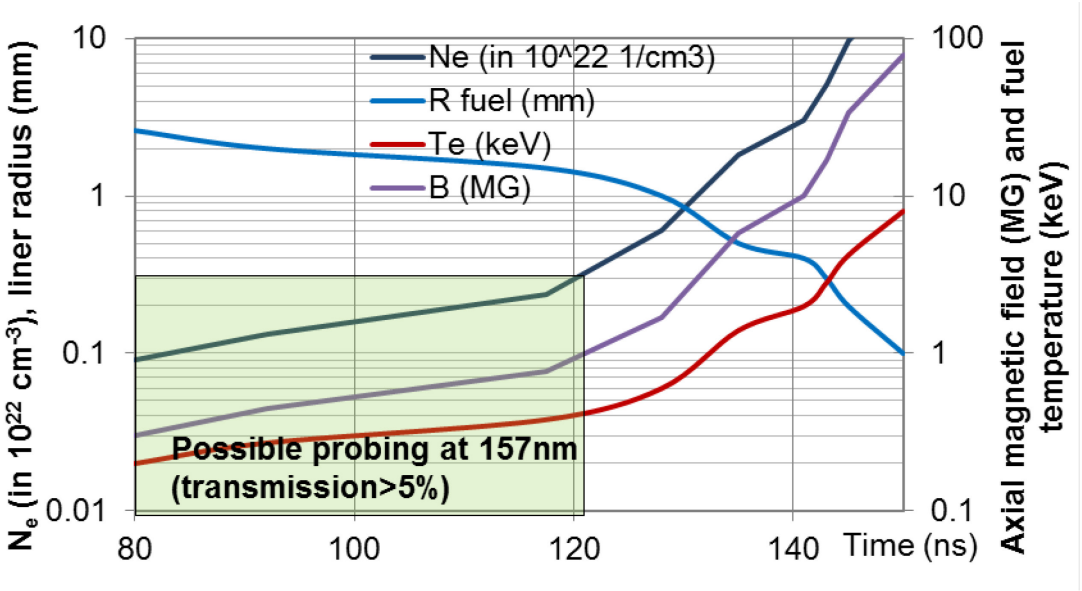

Figure 39. The evolution of parameters in the implosion of a 3mm radius MAGLIF capsule with an initial 3mg/cm^3 deuterium fill. Rectangle shows the feasibility of laser probing at 157nm (transmission larger than 5%), [Slutz2011].

3.11. Conclusions

These results show that gated star wire arrays can reproduce the transparent and nontransparent implosion regimes. In the transparent mode, the imploding plasma from the outer wires passes by the wires of the inner cylinder. In the nontransparent mode, the gates of 0.3-2mm width trapped the plasma from the outer wires, which formed plasma columns at the gate positions that imploded together. The presence of gates did not have a significant effect on the x-ray yield, only on the timing of x-ray pulse. The current through the gate wires can be calculated using inductive current division.

A vertical, end-on probing beamline was developed and built for the Zebra generator. Shadowgrams demonstrated that the pinch can be probed during the implosion and stagnation phase. Using 266nm instead of 532nm laser extends the densities where the plasmas can be penetrated. Wire array configurations were tested to produce colliding

plasma jets, but with inconclusive results. The 266nm laser was capable of fully penetrating the stagnating pinch of a light 1cm-high Al wire array implosion.

It was planned to induce rotation in a pinch by offsetting wires azimuthally in a star wire array, providing a radial component to the magnetic field. End-on probing did not offer proof on the rotation due to fast plasma motion. Side-on shadowgrams of such implosions, however, suggest that these loads imploded in the “transparent” regime.

Deep-UV end-on probing could be used to probe wire arrays and liner implosion experiments, and could provide information of magnetic field compression and convection with the use of Faraday imaging.

4. STUDY OF NON-PRECURSOR IMPLOSION IN CLOSELY SPACED AND STAR WIRE ARRAYS

During the ablation stage the ablated plasma behavior is determined by the **j**×**B** forces acting in the plasma. In cylindrical wire loads, the inward-pointing **j**×**B** forces result in plasma accumulation on the axis of the array. As discussed in Chapter 1.5.2., the precursor can affect the final pinch in several ways, beneficial or detrimental to the stability of the stagnating z-pinch plasma and its x-ray production.

To determine whether these effects of the precursor are important, experiments where the presence of the precursor can be controlled are necessary. In the case of linear arrays, equidistant wire spacing would produce an implosion with a precursor. When the center wire gap is increased, it was found that two plasma columns formed on the two sides of the array [Ivanov2008] before the final implosion. The absence of the precursor could be explained by the direction of the **j**×**B** forces. If there was an outward ablation on the inner wires, no precursor would accumulate on the center. Overall, wire arrays without a precursor had 5-10% reduced x-ray yield than arrays with precursor, but the configuration change modified the implosion dynamics, which could have affected the yield. On the Z accelerator, non-precursor ablation was achieved by a different mechanism. In large-diameter (up to 70mm) nested cylindrical arrays, investigated for high K-shell yield, the ablated plasma might not have reached the axis before being swept by the faster, main plasma implosion [Jones2008]. Such an implosion dynamics, however, offers no direct comparison with precursor implosions.

4.1. Closely spaced nested wire arrays

Non-precursor implosions were studied with a new array configuration, in which outward **j**×**B** forces would suppress centerward ablation, and thus precursor formation. If the single wires of a cylindrical array are replaced with wire pairs that are placed close together and aligned radially, the proximity of the outer wires would reverse the direction of the **B** field at the inner wires, and the ablative forces would point in the outward direction. Such closely spaced nested wire array configurations are shown in Fig.40. Such a closely spaced wire array with outer diameter R=8mm and wire spacing ΔR=1mm will be referred as a 16/14mm wire array, the numbers referring to diameters instead of radii.

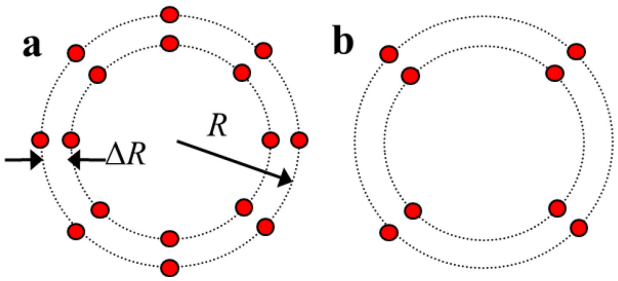

Figure 40. Schematics of closely spaced wire arrays with 16 (a) and 8 (b) wires, with wire pair spacing of ΔR.

The magnetic field around the wire pairs can be separated into a local and global component. Assuming an even current distribution between the wires, the global magnetic field (from all the other wire pairs) at the position of a wire pair can be written, based on eqn. (1-4), (using notation in Fig.40 as

$$B_{global} = \frac{\mu_0 I}{4\pi} \frac{N-2}{N} \frac{1}{R}, \qquad (4\text{-}1)$$

where N is the number of wires is the array – assuming that the global field does not change much within the distance ΔR. To get this formula, one must add up the contributions from every wire (except the wire pairs) of the vectorial components of the magnetic field – and assume ΔR=0. The local magnetic field (from the other wire of the pairs) on the other hand would be

$$B_{local} = \frac{\mu_0 I}{2\pi}\frac{1}{N}\frac{1}{\Delta R}. \qquad (4\text{-}2)$$

At the position of the inner wire, the local field from the outer wire is in opposite direction to the global field. The ablation forces would point outward on the inner wires, if the local field is larger than the global one, when the wire spacing ΔR is "small enough", that is,

$$\Delta R < 2R/(N-2). \qquad (4\text{-}3)$$

According to this approximation, for a 16-wire array with R=8mm, the wire spacing should be less than ~1mm. The approximations do not take the exact geometries into account, nor the actual current distribution in the array.

4.2. Current distribution in closely spaced wire arrays

The magnetic field can be determined more accurately by calculating the current distribution, as described in Chapter 3. Using eqns. (4-1) and (4-2) would give inaccurate results, as the number of wires was low in the investigated arrays. The current fraction going through the inner wires was around 40% (35-45% depending on the configuration) due to the inductive shielding of the outer wires. Table 2 and Fig.41 shows calculated

j×**B** forces on the inner wires in 8 and 16-wire closely spaced arrays with the same outer diameter. With a 14mm inner array diameter (equivalent to ΔR=1mm) the forces were outward on the inner wires, which predicts a nonprecursor implosion. It should be noted that the total force on the wire pairs is not that different from the force on a single wire in a corresponding cylindrical array.

Config	Wire #	I_in	B_in	B_out	F_in	F_out
14/16mm	8	0.44	-18	32	-40	89
15/16mm	8	0.45	-45	55	-102	151
14/16mm	16	0.36	-5	21	-5	33
15/16mm	16	0.38	-20	31	-19	47
16mm	8			11		27
16mm	4			9		47

Table 2. Current, magnetic field and **j**×**B** forces in selected closely spaced and corresponding cylindrical (bottom two row) arrays.

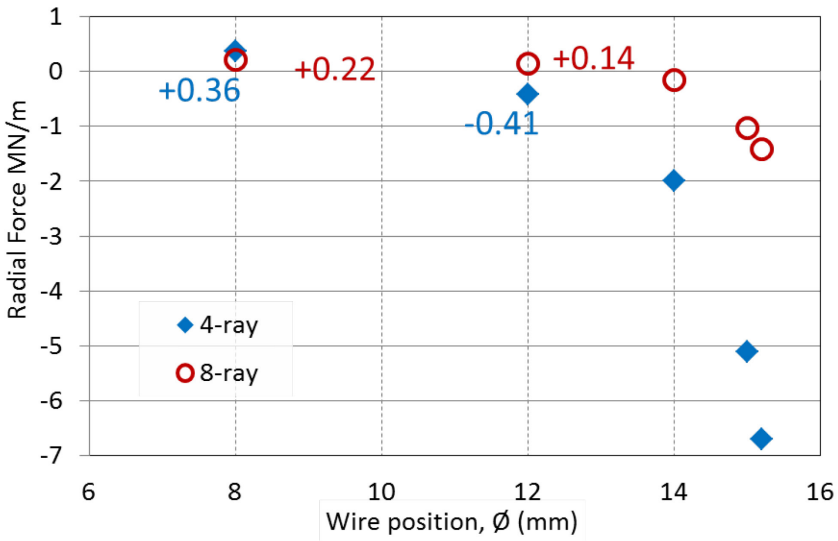

Figure 41. Radial **j**×**B** forces (negative outward, positive inward) on the inner wires at 0.5MA total current in closely spaced arrays with 16mm outer diameter, 4-ray 8-wire and 8-ray 16-wire loads. Wire position shows inner array diameter [Papp2012].

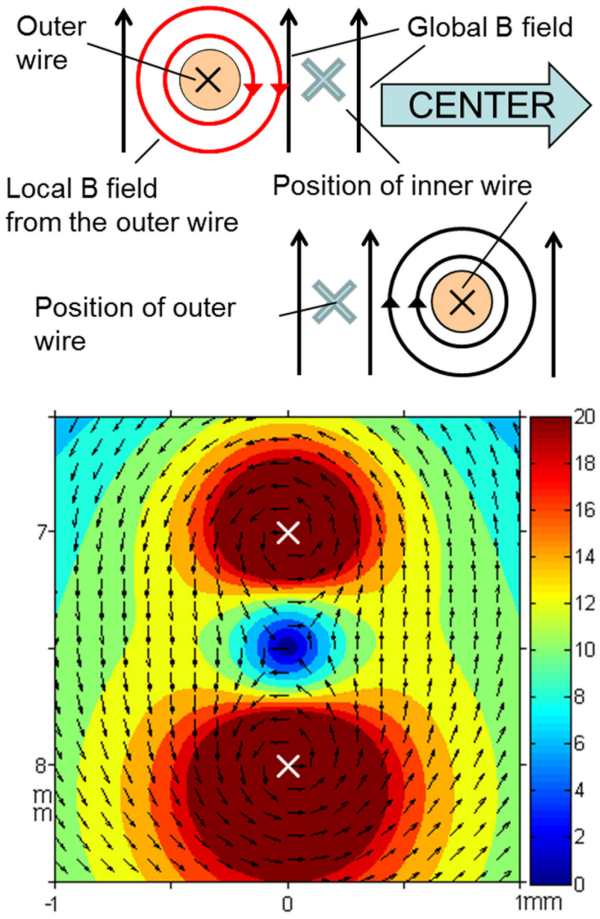

Figure 42. Schematics of the magnetic field around the wire pairs(a), and the magnetic field (arb. units) around the closely spaced wire pairs (b) [Papp2012], calculated for a 16/14mm 8-wire array. Array axis is at (0,0). Wire positions denoted by X.

In different closely spaced configurations (varying the wire spacing and the number of wires, but keeping the outer diameter the same) the magnetic field configuration around the wire pairs is qualitatively similar, with a null-point between the wires. The magnetic field configuration for a 8-wire 16/14mm array is shown in Fig.42, and it was similar to that in other closely spaced arrays with different wire numbers and spacing. The outward $\mathbf{j}\times\mathbf{B}$ forces would also suggest that the formation of precursor plasma columns between the paired wires would be possible. Otherwise, the strong attraction between the wires should result in early (ablation phase) merging of the wires.

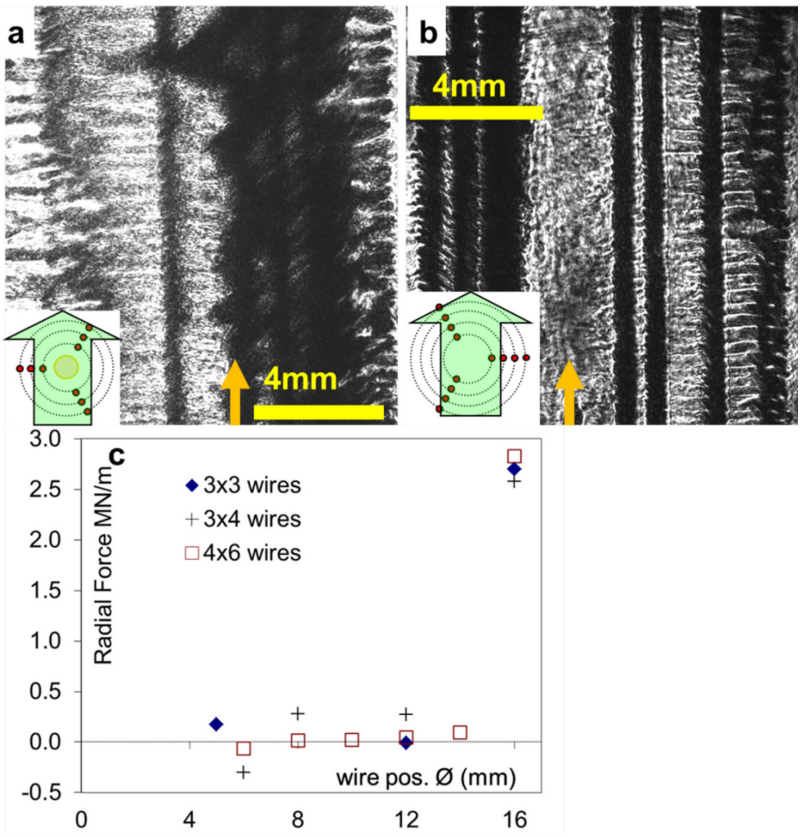

Figure 43. 3x3-wire star wire array #965 (a), with a precursor (Orange arrow). 3x4-wire wire star array #1714 (b) imploding without precursor. The **j**×**B** forces acting on the wires in these arrays and a 4x6 star wire array (positive inward, at 0.5MA total current) [Papp2012].

4.3. Nonprecursor implosion in star wire arrays

Star wire arrays, depending on configuration, implode with or without the formation a precursor. Fig.43 shows two different star arrays, imploding with and without a precursor. Calculating the current distribution and the magnetic field in these arrays shows that the wire arrays that imploded with precursor had inward pointing **j**×**B** force on the innermost wires [Fig.43(c)]. In implosions without a precursor, such ablative forces pointed outward. The direction of the ablative force and the magnetic field is heavily influenced by the position of the second wire from the inside. When there is a large gap

between the innermost and outer wires in a ray, the ablative forces on the innermost wires point to the center, and there is a precursor during the implosion. When there is another wire close to the innermost wire, its magnetic field causes an outward force on the innermost wire, preventing the formation of the precursor.

Rays	3	3	4	4	4	6	6
Number of wires	9	9	12	12	12	18	18
Wires at diameter (mm)							
Outermost	16	16	16	16	16	16	16
Middle	12	10	14	12	10	14	12
Innermost	6	6	8	8	8	10	10
jx**B** force direction on inner wires	In	Out	In	Out	Out	In	Out

Table 3. The direction of **j**×**B** forces (on the innermost wires) in 3, 4 and 6-ray star wire arrays depending on array configuration. Forces were calculated using the inductive current-distribution program.

Star wire arrays provide a great advantage in investigating the effect of precursor on the x-ray yield. Keeping the inner and outer diameters constant, changing the position of the middle wire (moving it closer or farther from the center) changes the direction of the ablative force on the inner wire, which should determine the direction of the ablation, and the presence or absence of the precursor. With such minor alteration in the wire array configuration, the implosion dynamics is changed only minimally between the different loads – except of the presence of the precursor. Table 3 shows star array configuration pairs in different star arrays. The position of the inner wires was determined by the requirement that the ablative forces must change direction when the middle wire is moved, so it could not be held the same for 3,- 4- and 6-ray star arrays.

4.4. Experiments on non-precursor and precursor closely spaced nested and star-like wire arrays

Closely spaced nested cylindrical wire arrays were investigated during several experimental campaigns on the Zebra generator. Implosion dynamics and x-ray radiative characteristics of these arrays were compared to regular cylindrical and nested cylindrical arrays. Aluminum star wire arrays were also investigated, where wire arrays in the corresponding precursor and nonprecursor were compared. The wire material, unless noted, was Al 5056 alloy with 5% Mg content, which provided low-opacity lines for x-ray spectroscopic purposes.

4.5. Presence of precursor in closely spaced arrays

For closely spaced arrays with 6-8 wires shadowgrams showed no ablation phase precursor [fig.44], in agreement with **j**×**B** force calculations. Fig.44(a),(e) and (f) show that the array axis is empty of plasma during the ablation stage, for 6 and 8-wire arrays with ΔR=0.5-1mm. Later, during the implosion phase, axial plasma accumulation was observed in 8-wire arrays [Fig.44(b)], even when there was no precursor in the ablation phase. Fig. 44(a) shows the first shadowgraphy frame for the same load during ablation with no precursor. At the latter stage the magnetic configuration of the array would be changed from the initial one, however. The implosion of the 6-wire star array is noticeably different. Three plasma columns form early [Fig.44(f)], and they start breaking up before they implode into the center.

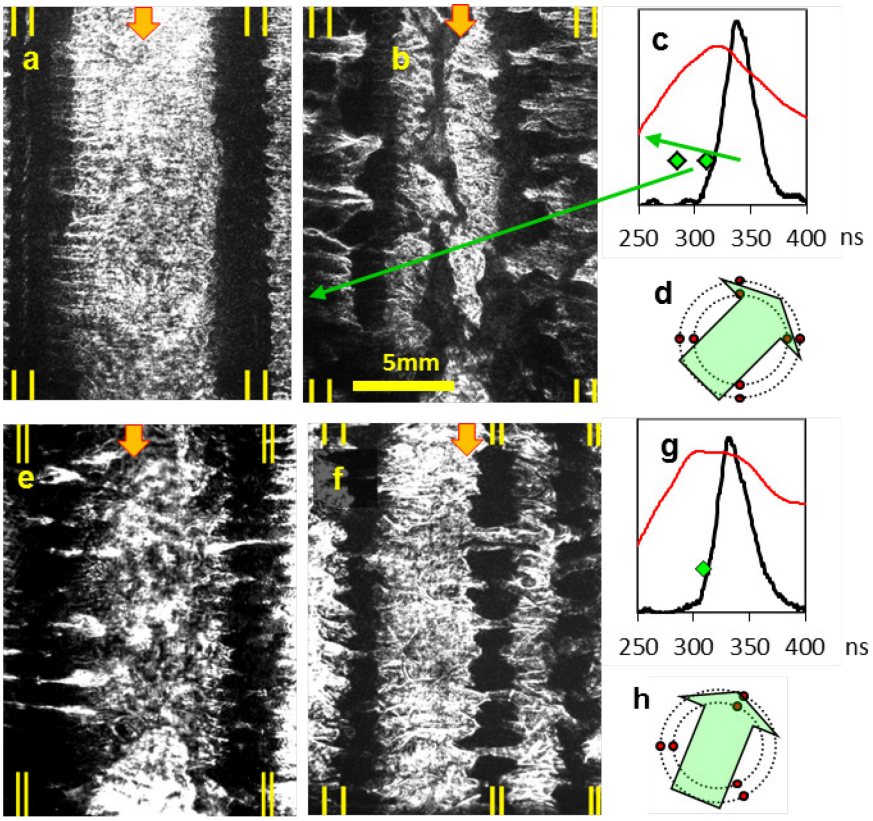

Figure 44. Two-frame shadowgraphy of a 8-wire 16/14mm load, shot #2396, with no precursor (a), and late plasma on axis (b) 25ns later, timing (c) and orientation (d). Shadowgram of 8-wire 16/15mm load, shot #2400 (e), timing (g) and orientation (d). Shadowgram of a 6-wire 16/15mm load #1344 (f) and orientation (h). Original wire positions denoted by yellow lines, array axes by arrows. From [Papp2012].

Optical streak images (Fig.45) for 8-wire cylindrical and 4-ray 8-wire closely spaced arrays show similar features. The precursor formation on the axis is apparent for the cylindrical array, preceding the implosion of the main array mass, as shown by the arrow in Fig.45(a). In closely spaced arrays, however, any axial plasma accumulation is clearly delayed [Fig.45(d),(e)] compared to the cylindrical array. The plasma arrives on the axis late, only shortly before the formation of the main pinch, in agreement with the shadowgrams. Furthermore the double-wire structure of closely spaced arrays is

conserved long into the implosion phase [Fig.45(d),(e)] – no early merging of wire pairs was seen as in the 16-wire arrays.

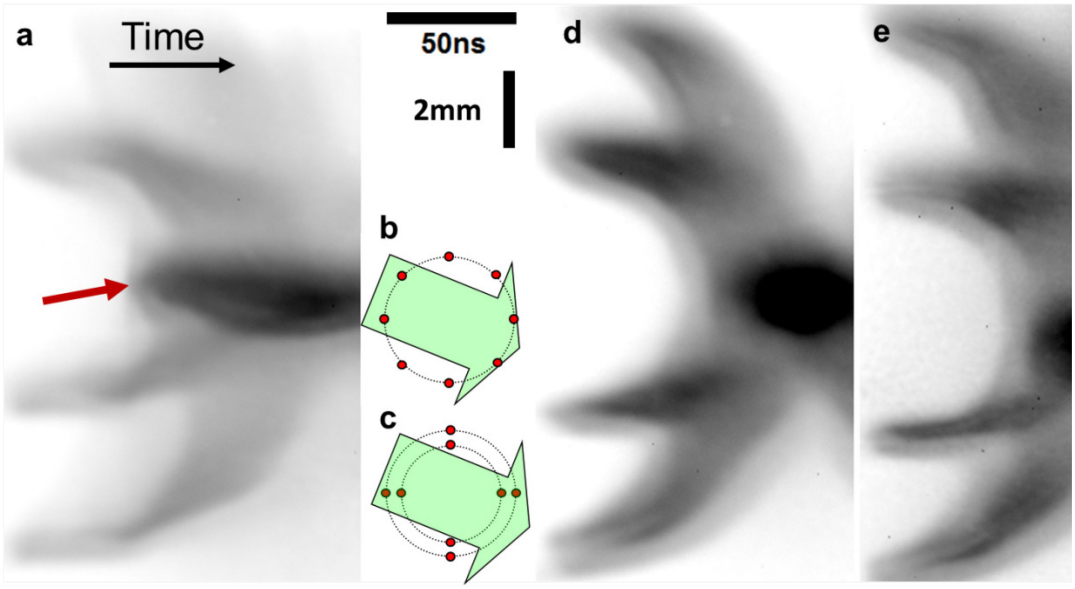

Figure 45. Optical streak camera image (a) of a regular cylindrical array, shot #2394 (b). Viewing direction for 8-wire closely spaced loads (c). Streak images of 8-wire 14/16mm, shot #2395 (d) and 15/16mm, shot #2400, (e) loads. The precursor plasma in (a) is indicated by arrow. Taken from [Papp2012].

In closely spaced nested arrays with 12-16 wires and ΔR=0.25-1 mm, precursor plasma was observed on the axis despite calculated outward ablative forces on the inner wires (Fig.46). In arrays with a small wire spacing (ΔR=0.25-0.5mm) these outward forces are very strong due to the proximity of the outer wire, but it does not prevent the formation of the precursor. The cause of this discrepancy most probably arises during the ablation process, and will be discussed later. Variations of wire diameter and array mass (33 to 53 µg/cm), or wire pair separation (ΔR=0.25-1 mm) had no discernible effect on the existence of precursor, it was determined solely by the number of wires in the array. It should be noted that the lower wire-number arrays had larger diameter wires than higher wire-number arrays of the same mass.

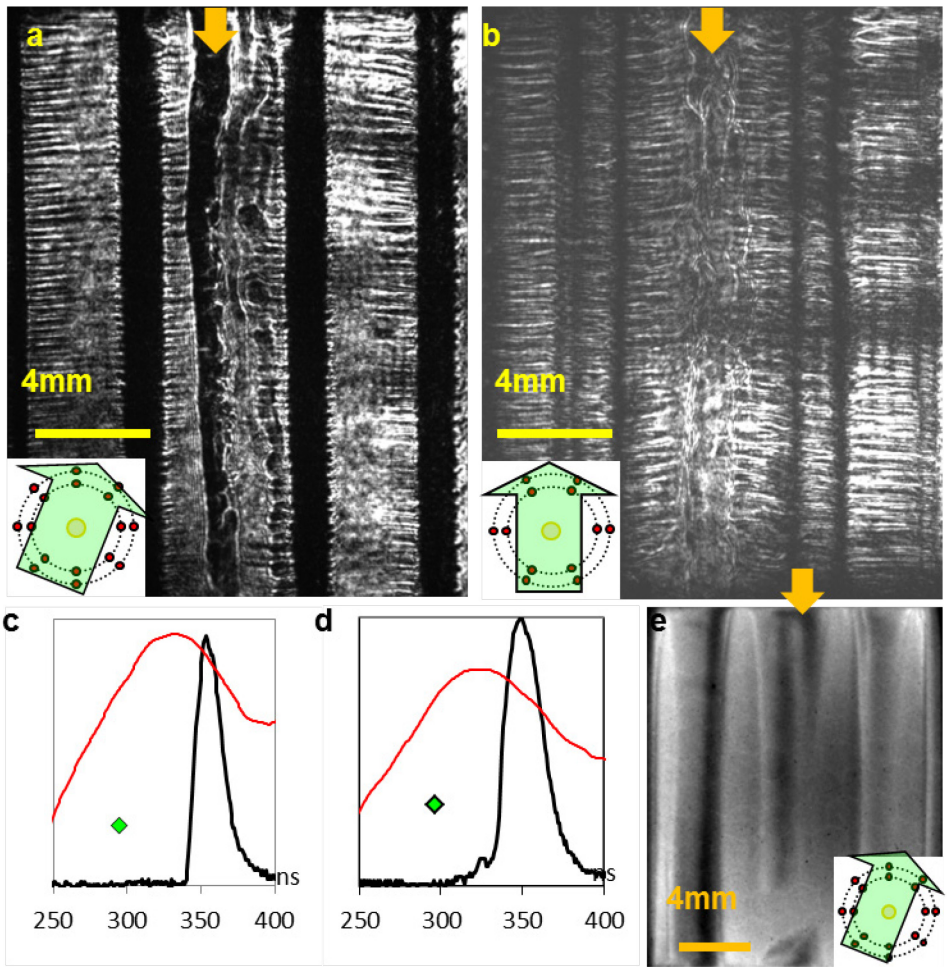

Figure 46. 532nm shadowgram, probing direction (a) and frame timing (c) for a 16-wire 15.2/16mm nested array #1068. 532nm shadowgram (b) and frame timing (d) for a 12-wire 15/16mm nested array #1352 (d). Gated ICCD image (e) for a 16-wire 15/16mm nested array #2385. Precursor plasmas on the axes are indicated by arrows.

4.6. Ablation and implosion dynamics in closely spaced arrays

The early ablation stage of closely spaced arrays was investigated in 8, 12 and 16-wire loads, with 14 and 16mm inner and outer array diameters, with 1mm gap between the paired wires. Shadowgraphy and schlieren imaging was used to determine the direction of ablation, and if inter-wire precursors would form.

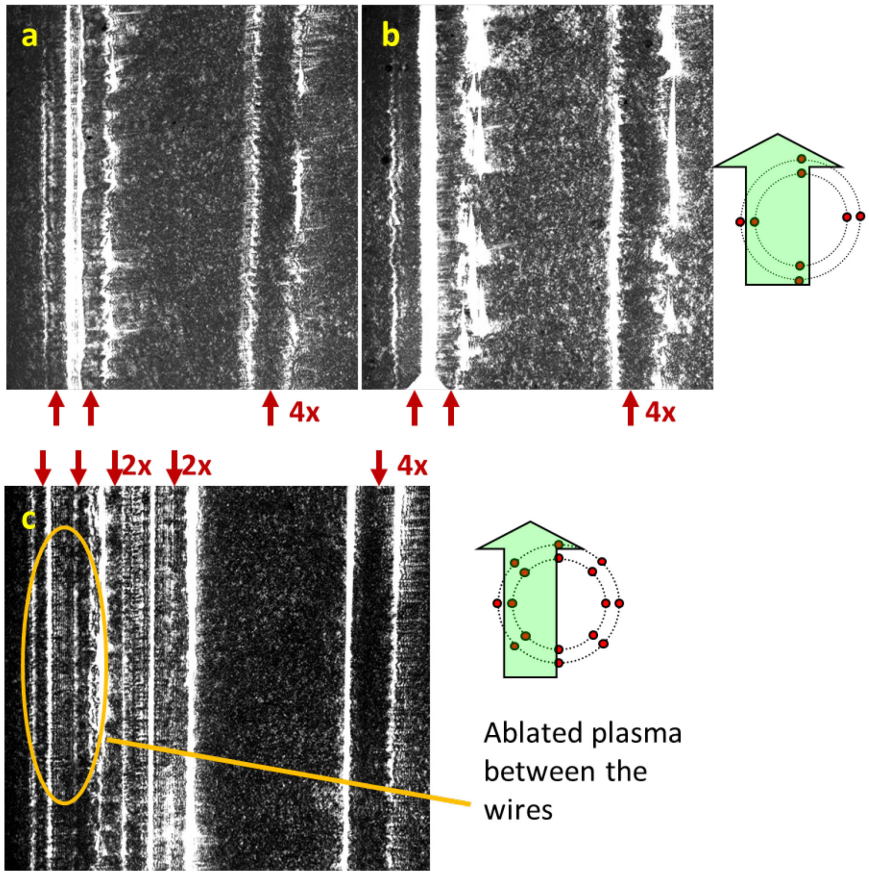

Figure 47. Schlieren images of closely spaced wire arrays in the early ablation stage. Shot #2618, 16/14mm 8×15μm wire array (a) at 0ns and at 7ns (b) frame delay with probing direction. #2619, 16/14mm 16×10μm wire array (c). Arrows show position of wires, number of wires covered shown next to arrows. No timing diagram available. High intensity (white) areas correspond to high plasma gradients.

Schlieren images in Fig.47(a),(b) shows that plasma starts ablating to the center on the inner wires, despite outward ablative forces. The plasma between the wires [Fig.47(c)] is ablated from the outer wire. Shadowgrams show similar features. No precursor formation was observed between the wires on the shadowgrams, either. Some shadowgrams show precursor-like features, but they are artifacts from the intensity variations in the probing laser beam. The same intensity features are present on reference

images taken before the Zebra shot [Fig.48], overlapped by the periodic pattern of wire ablation. Ablation from the inner wire [Fig.48(e)] can also be seen.

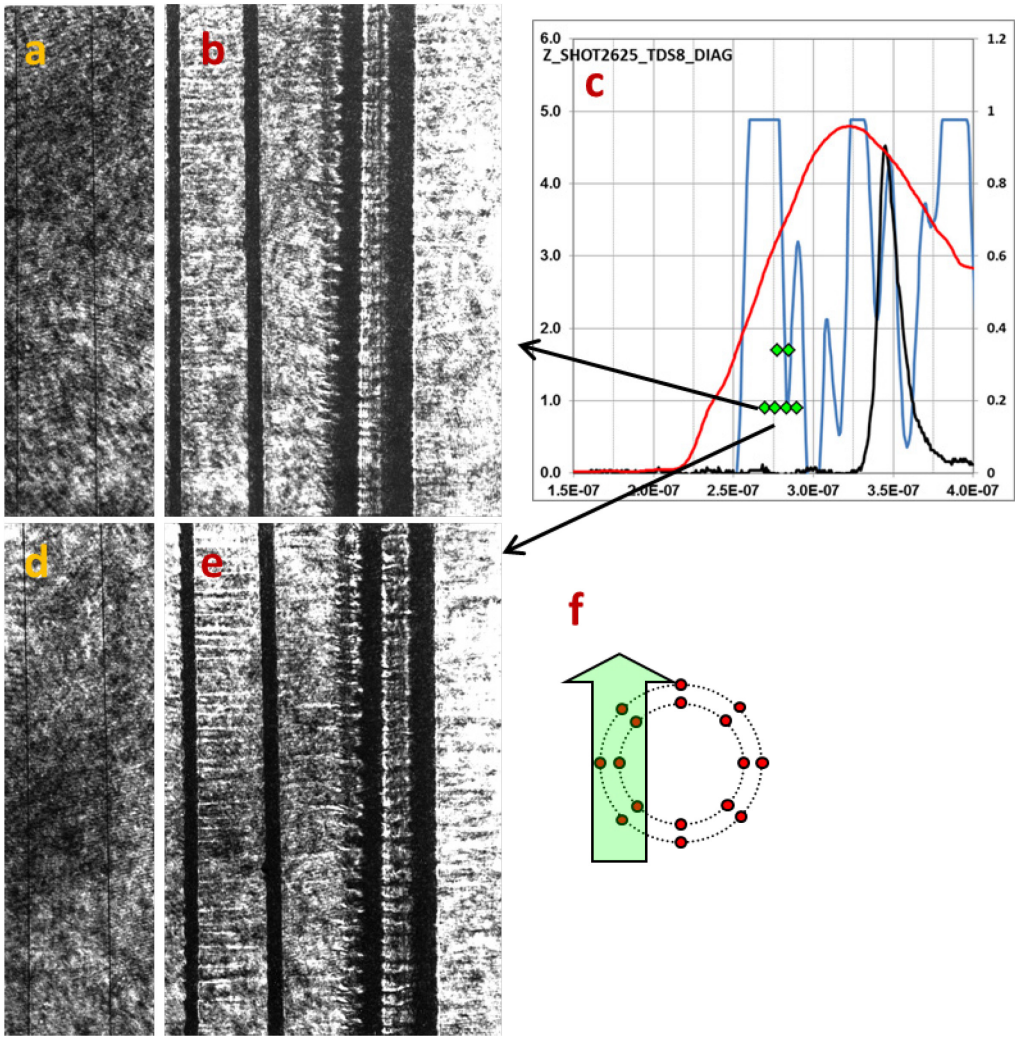

Figure 48. Two-frame shadowgram with 7ns delay (b,e), and corresponding reference images (only one pair of wires shown) (a,c). Timing diagram (c) and probing direction (f).

The ablation-implosion dynamics in closely spaced nested arrays is similar to the hydrodynamic collision mode of regular nested wire arrays [Deeney1998, Chittenden2001], but it also shows some cascading features of star arrays [Ivanov2009PRL].

Details of the ablation process were revealed by 2-frame 266 nm UV probing, which penetrated into plasma opaque to regular 532 nm laser probing. This allowed the resolution of breaks in the wire cores, which were not visible at 532 nm [Fig. 48(a),(d)]. Ablation starts in the outer wires, where both the current and the magnetic field are stronger. The outer wires break up first, while the inner wires still ablate [Fig. 48(e),(f)]. The plasma from the inner wires is ablated to the center. No outward ablation or outward movement of the inner wires was observed despite the strong outward **j×B** forces calculated for the initial configurations. The streak camera images (Fig.45) also show wire pairs moving together to the center, and that the double structure of wire pairs is preserved during the ablation phase. After the outer wires implode into the inner wires, the merging forms a smoothed implosion plasma front that can be seen in [Fig. 44(b)], which was seen in star wire arrays [Ivanov2009PRL].

It was also found that the wire diameter has an effect in the ablation, similar to the one discussed in [Yu2007]. In loads with fewer number of larger diameter wires, the ablation exhausts the wire cores earlier, triggering an earlier implosion stage. Fig. 49(g),(h) show the ablation of two closely spaced wire arrays at corresponding time during the implosion, at 70% of maximum current. The 8-wire load [Fig.49(g)] has the outer 15μm wires already broken up, imploding into the inner wires, while the wire cores are still intact in the 16-wire load Fig.49(h)] with 10μm wires, despite being 10% lighter in mass. The earlier implosion of lower-wire number closely spaced arrays corroborates this. It was found that for 8, 12 and 16-wire closely spaced arrays with ΔR=1mm, the implosion time increases with increasing wire numbers (Fig.50). 8-wire loads implode

~8 ns earlier than 12-wire loads and 13 ns earlier than 16-wire loads. This is despite that the radial mass distribution is similar in these arrays. Furthermore, due to the constraint in available wire diameters, the 8-wire load was heavier (37.3µg/cm nominal mass) than 12-wire (35.8µg/cm) and 16-wire (33.2µg/cm) arrays, which would suggest an opposite trend.

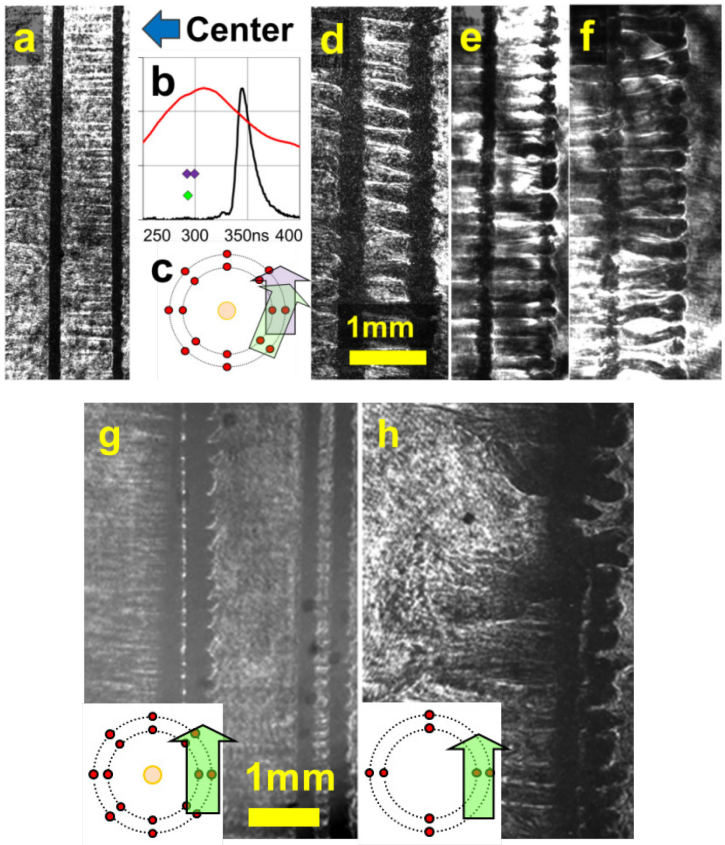

Figure 49. 532nm shadowgram of early stage ablation in a 16-wire 16/14mm load, shot #2625 (a). 532 nm (d) and 266 nm (e,f) shadowgrams of a 16-wire 16/14mm load, shot #2393, (not to scale). Probing directions shown in (c). 532 nm shadowgrams of shot #1170 (g) 16/15.2mm 16×10µm load of shot #1170 (h) 16/15.2mm 8×15µm load. The latter two frames were taken at similar time – at 70% of the maximum current. [Papp2012].

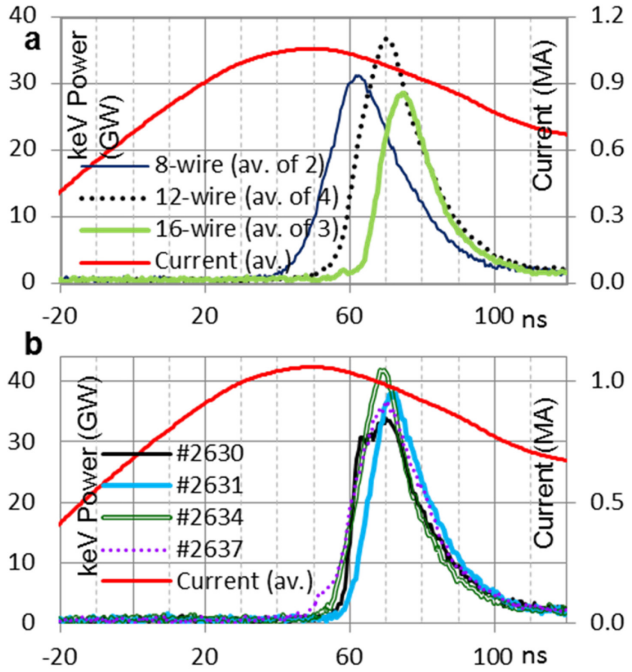

Figure 50. keV x-ray power (PCD with 8μm Be filter, keV x-rays) for 8, 12 and 16-wire closely spaced loads (top). Signals are averages for indicated number of shots. PCD KeV signal for 12-wire closely spaced loads (bottom) [Papp2012].

The x-ray pulse shape is fairly consistent for closely spaced arrays with small shot-to-shot variations, unlike simple cylindrical arrays, despite the low wire numbers. Fig. 50(b) shows the reproducibility of keV x-ray pulses for four 12-wire closely spaced arrays. Star wire arrays had the best demonstrated pulse-shape reproducibility on the Zebra generator [Ivanov2008a].

The timing and appearance of the precursor for shots 895-1342 and 2385-2400 is summarized in fig 51. The appearance of the precursor is delayed in 12-wire loads compared to the 16-wire loads. There is a shot-to-shot variation in the appearance for 16-wire arrays, which might also be caused by different array masses, limitations of the frame timing and difficulty to determine the presence of precursor in some viewing directions.

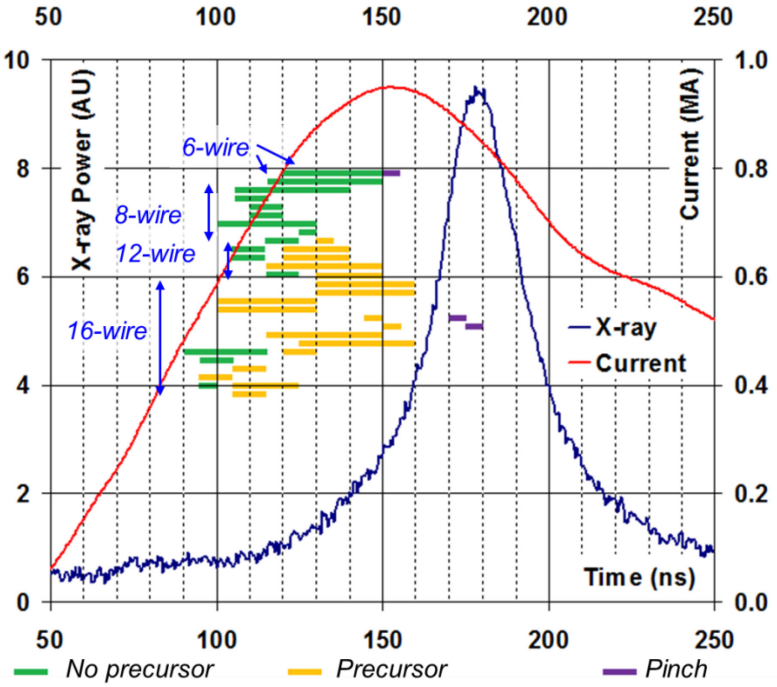

Figure 51. Presence of precursor in shadowgram frames. Green lines signify no precursor seen on shadowgrams, yellow signifies precursor present, and purple signifies the stagnating pinch. Current and soft x-ray pulse is average for shots #2385-2400.

4.7. X-ray yield of closely spaced arrays

In the first set of shots, regular nested arrays were compared to closely spaced nested and regular cylindrical arrays. Array mass was close to optimal for the Zebra generator, between 33 and 40 μg/cm, as uniform as possible given the constraints of available wire diameters. Data from over 70 shots are presented in this section, and groups of similar loads are analyzed.

Nested wire arrays produced the highest total x-ray yields of the investigated configurations (Fig. 52), an average 9.0 kJ for 6-wire, 10.7 kJ for 8-wire and 9.8 kJ for 16-wire loads. KeV-range (Al and Mg K-shell) x-ray yields for nested 16/8mm arrays with 6, 8 and 16 wires were 880 J, 830 J and 640 J in average, respectively. 8-wire regular cylindrical loads generated 7.4 kJ total and 295 J keV X-ray energies.

Closely spaced arrays with 6 wires and ΔR=1 mm (imploding without a precursor) had the worse yield of 5.0 kJ total and 305 J keV x-ray energies. 8-wire loads with ΔR=0.4 mm and 1 mm had similar total energy of 5.5 kJ, but a keV energy of 815 J.

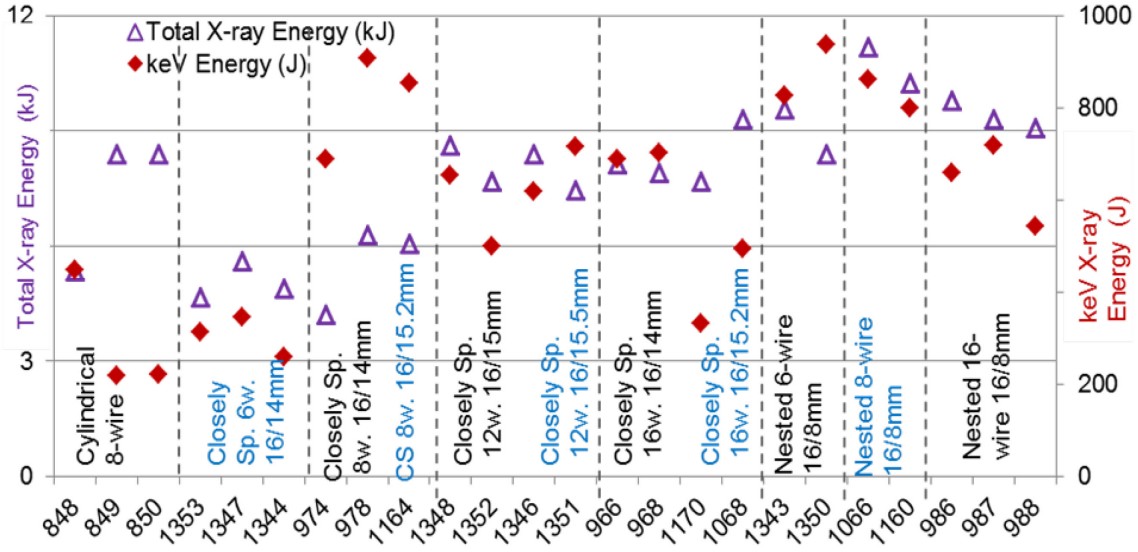

Figure 52. X-ray yields for cylindrical, nested (ΔR=4mm) and closely spaced (CS) loads (ΔR=0.25-1mm).

The 12-wire arrays with ΔR=0.25-1 mm had similar yields, average total x-ray energies of 8.0kJ, and keV energies of 620J. For both the 8 and 12 wire closely spaced loads, the wire pair spacing ΔR had no discernible effect on the investigated x-ray characteristics. 16-wire arrays with ΔR=1mm had 8kJ total, 700J keV energy and 34GW k-shell power. 16-wire arrays with ΔR=0.4mm had 8.5kJ total, 410J keV energy and 20GW k-shell power - the keV yield and power was reduced for the smaller wire gap. Closely spaced arrays had worse x-ray energy than corresponding regular nested arrays of ΔR=4mm. Replacing the single wires in 8-wire regular cylindrical load with the closely

spaced wire pairs resulted in a 10% increase in soft x-rays energies and an average 70% increase in keV x-ray energies.

In the second series of shots, 8 and 16-wire closely spaced arrays were compared, with inner diameters of 14 and 15 mm. All arrays had the same mass of 53 µg/cm, heavier than required for optimal implosion time (around 36 µg/cm). Results are displayed in Fig.53.

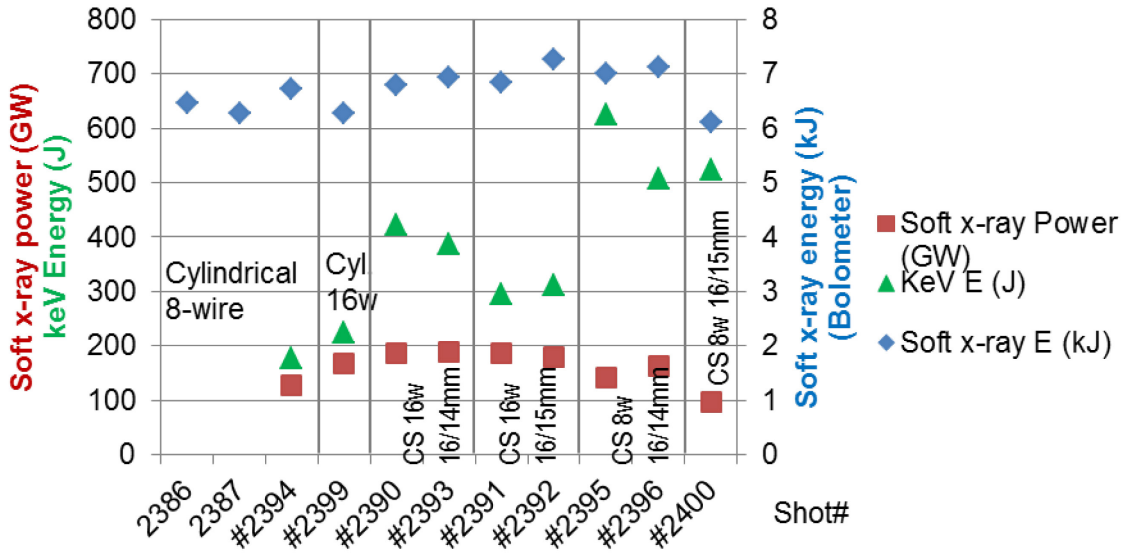

Figure 53. X-ray yields for 53µg/cm closely spaced (CS) and cylindrical arrays; 'w' stands for wire

Total soft x-ray energies were similar for these shots for 8 and 16-wire loads with an average of 10.1kJ. 16-wire closely spaced arrays had 40% higher total x-ray power compared to similar 8-wire arrays. The average keV x-ray energy and power for the 16-wire arrays with ΔR=0.5mm was 300J and 13GW. For 16-wire arrays with ΔR=1mm the keV x-ray energy and power was 400J and 19GW. For the 8-wire arrays, average keV x-ray energy was 570 J, a 50-90% improvement in energy over the 16-wire arrays, better

than the corresponding 40% improvement in the lighter loads. Varying the wire spacing for 8-wire loads at ΔR=0.5 and 1 mm had no discernible effect.

In the third set of shots, loads with 8, 12 and 16 wires at 16/14mm diameters were studied. Nominal load masses were 37.3, 35.8 and 33.2 μg/cm, respectively. The keV range energy yield for 8 and 12-wire loads were identical, averaging both at 805 J. 16-wire loads had an average keV energy yield of 470 J. 12-wire loads in this third series had keV yields similar to 8-wire loads, while in the first series yields were similar to the 16-wire loads. The highest keV power was produced by 6-ray stars, with an average maximum peak of 38GW (Fig. 50). Regular 8-wire cylindrical loads with 16mm diameter and a mass of 37.3 μg/cm, produced keV x-ray yield of 820 J in average, with an average peak power of 26GW – higher K-shell yield unlike in the first series of shots. There were two significant differences between the first and third series, the wire pair spacing in closely spaced arrays (1 mm vs. 0.4-0.5 mm) and the modified current return configuration.

4.8. Comparison of precursor and non-precursor implosions in star arrays

In star wire arrays, the direction of j×B forces on the inner wires is in agreement with the presence of the precursor. Non-precursor and precursor star array configurations, described above, were designed and tested to determine the effect of the precursor on the x-ray yield. Star arrays with different number of rays and wires were investigated in 6-ray 18-wire, 4-ray 12-wire and 3-ray 9-wire arrays with a mass of 34-36 μg/cm (Table 3).

The difference between precursor and non-precursor configuration was only the position of the middle wires in each ray (Fig.54, Table 3), so direct comparison could be made.

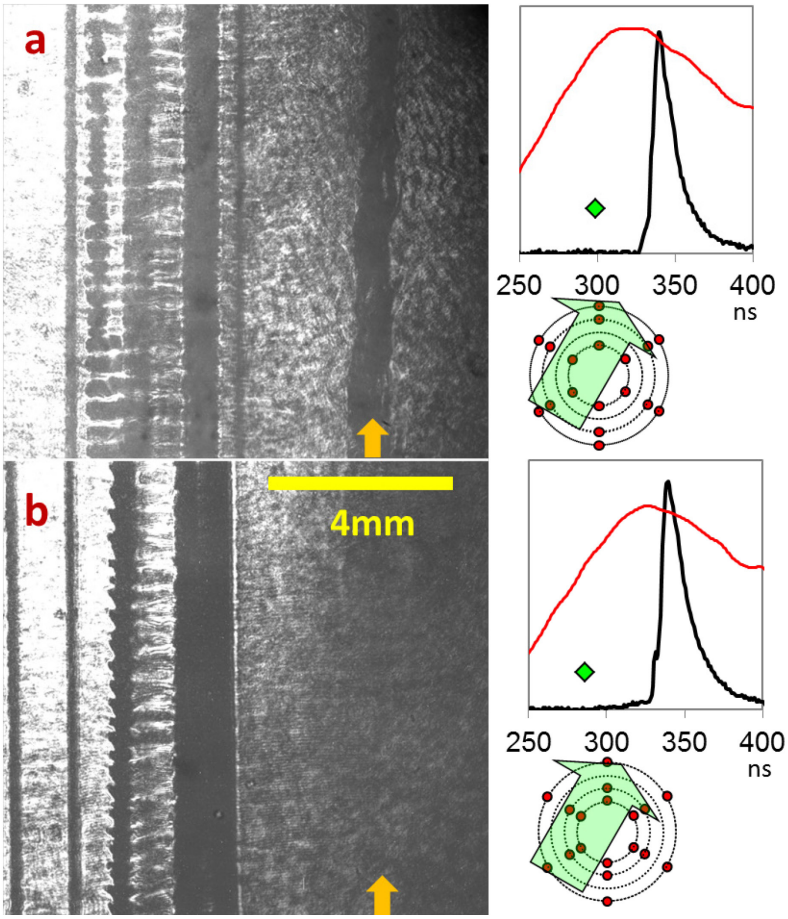

Figure 54. 532nm shadowgrams of star wire array implosions, with respective probing directions and frame timing. Shot #2629, 18-wire 6-ray star with precursor (a), wires at 16/14/10mm diameters. Shot #2626, 18-wire 6-ray star, non-precursor (b), 16/12/10mm dia. Array axes denoted by arrows [Papp2012].

The presence of precursor was in agreement with the calculations from current distribution in 6-ray [Fig. 54] and 4-ray [Fig.55] stars. The outward ablative forces on the inner wires prohibited plasma accumulation on the axis, or at least delayed it significantly. Fig. 54 and 55 shows that in similar 4 and 6-ray star-like loads, the position of the middle wires in each ray can be chosen to direct the ablating plasma flow from the

inner wires to the center or outward. 3-ray wire arrays were also tested, but in those cases the shadowgrams were not available to determine the presence of precursor, so they were used only for comparing x-ray yields.

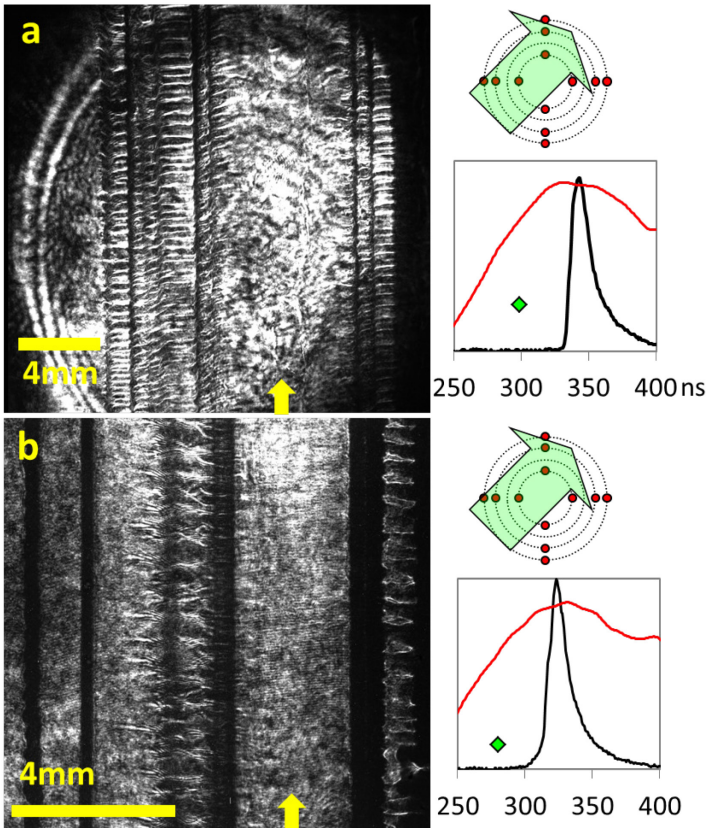

Figure 55. Shadowgrams of 4-ray star wire array implosions, with respective probing directions and frame timing. 266nm shadowgram shot #2636, 12-wire 4-ray star with precursor (a), wires at 16/14/10mm diameters. 532nm shadowgram of shot #2633, a 12-wire 4-ray star, non-precursor (b), 16/12/10mm dia. Array axes denoted by arrows.

Load configurations without a precursor had higher x-ray yields than precursor configurations [Fig. 56(a)]. Bolometer energies and total x-ray powers were slightly, but consistently higher (3-8%). Except for shot #2632, the keV x-ray energy and maximum power were 7-15% higher for non-precursor loads. The three-ray stars also had twice the keV yield of 6-ray stars, the highest yield belonging to shot #2685 with 1.42kJ and a

maximum power of 73 GW. This improvement in keV x-ray energy by reducing the number of rays is consistent with results for nested and closely spaced arrays. It must be noted that the radial mass distribution was different in 3, 4 and 6-ray star arrays, so direct comparison cannot be made. The implosion of the non-precursor arrays was also ~5 ns earlier than in precursor arrays for the investigated 3, 4 and 6-ray stars arrays, which might be attributed to the middle wire placed closer to the axis of the array.

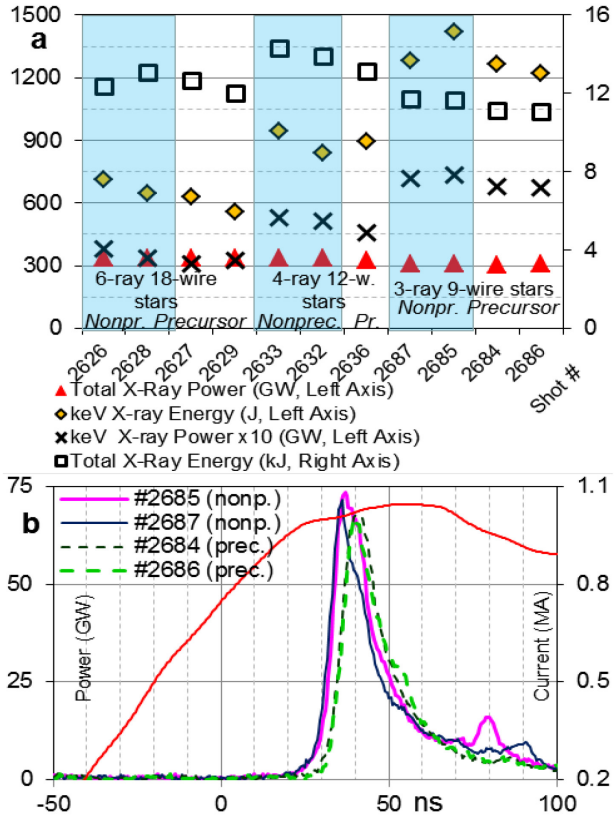

Figure 56. X-ray yields for star arrays in precursor (P) and non-precursor (NP) configurations (a). "Total X-Ray energy (kJ)" values for shots #2684- #2687 are inferred and not directly comparable with shots #2626- #2636. KeV x-ray signals in GW (b) for nonprecursor (solid) and precursor (dashed) 3-ray stars

Fig. 56(b) shows the timing of the keV-range X-ray pulse for 3-ray 12-wire star arrays; the pulse is earlier for nonprecursor arrays. Pulse timing for the 4 and 6-ray stars are similar. The 3-ray nonprecursor arrays also have a secondary peak that accounts for

some of the extra energy. Such second peak is not present in 4-ray and 6-ray star arrays. The 3-ray arrays are also faster than the 4- and 6-ray star arrays, but that also can be attributed to the radial wire mass distribution.

4.9. X-ray spectroscopy for closely spaced and star arrays

Some information of the plasma parameters of the stagnating pinch can be derived from x-ray spectroscopic measurements. Electron temperature and density can be inferred by comparing experimental spectra to theoretic predictions. As discussed in chapter 3, time-integrated measurement of the x-ray emission spectra was recorded by bent-crystal KAP spectrometer with different filters, imaged by a slit on a Kodak Biomax photographic film. The film was scanned by a calibrated photoscanner and x-ray intensity was derived from filter absorption, film and spectrometer sensitivity. To determine the plasma temperature, a wider spatial section of the spectrum was used, as compared to "hotspots" of the pinch [Ivanov2012PRE].

Fig. 57 shows the 1st order Al-Mg K-shell spectrum of shot #2693, an Al 5056 linear array. The second and third orders were also observable on the film. A slit provides axial resolution of the pinch along the lines, showing "hotspots" with strong continuum radiation as dark areas. The bending of the spectral lines is caused by the shape of the pinch, an effect of the same origin as the source broadening due to finite plasma size. Due to this effect, the whole height of the pinch cannot be processed, but a section it has to be selected instead.

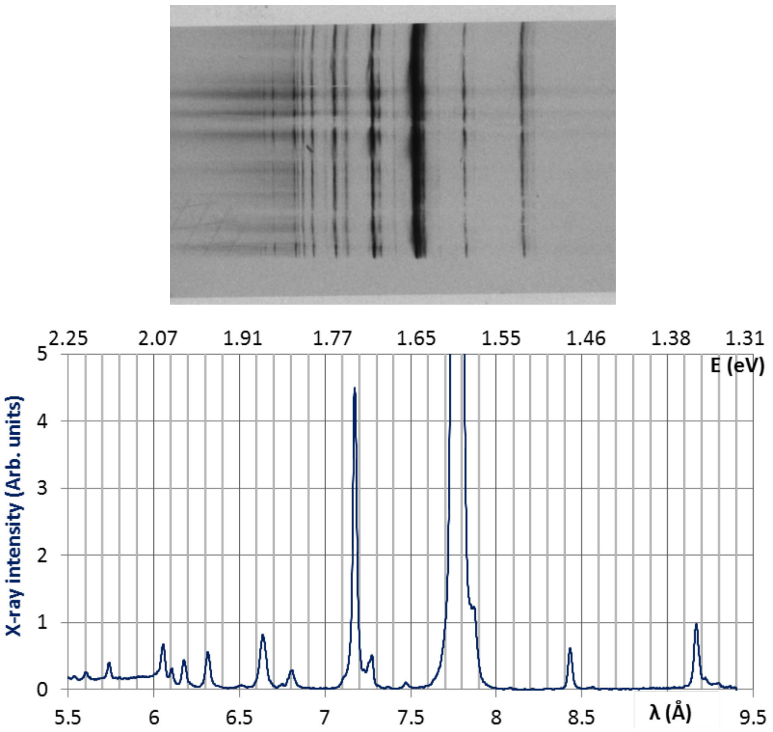

Figure 57. First-order spectrum of Shot #2693, an Al-Mg (alloy 5056) linear array (top), and calibrated spectral intensity (bottom). The spectraon the left, shows the Ly-α recombination continuumthe Al Ly-ε line at 5.5Å to the Mg He-α line at 9.2 Å. Al He-α line at 7.7Å is oversaturated on the film, and is clipped on the spectrum.

4.9.1. Theoretical model

The atomic physics code PRISMSPECT was used to determine theoretical baselines used in the comparison. This software is a 0D collisional-radiative spectral analysis code with direct configuration accounting, and calculates the population of atomic levels and their radiative properties given specified constraints, and accounts for opacity effects by through plasma thickness. For the purpose of simulating z-pinch plasmas, the code default K-shell emission spectroscopy model was modified. This default model contains H and He-like states of Al and Mg, and Li-like states of $1s^2nx^1$ (n=1-10, x=s,p,d,f) and $1s^12x^12y^1$ (n=1-10, x,y=s,p). Added levels include (for both Al and Mg) the ground states of C-, B- and Be-like states, and Li-like states $1s^1nx^1my^1$ (n=2-3, x=s,p,d, m=3-5,

y=s,p,d,f). To speed up running time, the fine structure of the atomic levels was collapsed for the population calculations, but was included in the spectroscopic model. Furthermore, steady-state and non-local thermal equilibrium options of the code were used.

1D slab geometry was used to model the pinch, as the code model use cylindrical geometries. To limit the parameter space, it was assumed that 75% of the nominal array mass of 36μg/cm, i.e. plasma of 27μg/cm takes part in the stagnation. This plasma was assumed to occupy a square column with sides *b*, and this column width *b* was assumed to be the slab thickness.

The shortcomings of this model are obvious. The pinch plasma is strongly non-uniform and irregular, with a colder outer shell surrounding the pinch, with very strong time dependence. Still, temperature, even if derived from such a strongly homogenized steady-state model, is an important property of the pinch.

4.9.2. Determining temperature from line ratios

The most intense lines of the spectrum, the He-α and Ly-α lines cannot be used to estimate the temperature of the plasma. These lines can saturate the film, leading to large experimental error. Furthermore, according to PrismSPECT simulations, these lines have a large optical depth, in the order of several hundreds at the best fit temperatures, and correspondingly high opacities [Ivanov 2009PRE]. Due to the low resolution of the experimental setup, the ratios for Mg lines and their satellites, like in [Ivanov2009PRE], could not be used to gain information on the pinch. Instead, the dependence of line ratios

on the electron temperature T_e and density (and thickness) was determined. It was found that the most unambiguous data could be derived using Mg and high-energy Al lines.

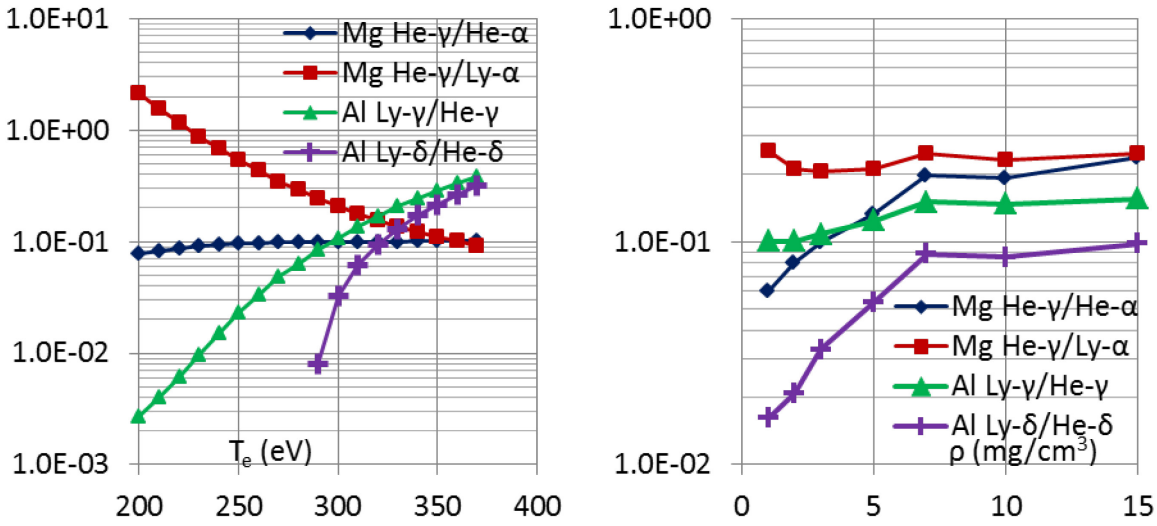

Figure 58. Al and Mg line intensity ratio dependence on electron temperature at 3mg/cm^3 density (left); plasma density dependence at 300eV (right)

Fig.58 shows the temperature and density-dependence of the ratios of the Al Mg line intensities, derived from PRISMSPECT simulations. The ratio He-γ/Ly-α has relatively flat density dependence between 1 and 15 mg/cm^3, and strong T_e-dependence, and can be used to approximate the temperature of the plasma. Conversely, the ratio He-γ/He-α has flat T_e-dependence, which can be used to derive the density of the plasma. The opacity of the Mg lines is low due to the low (5%) Mg content of these plasma. For the Al lines, the ratio of the Ly-γ and He-γ lines provides the best insensitivity for density and good sensitivity to temperature. No Al line ratios were found that could provide information on the plasma density, howerver. It should be noted that the He-β line of Mg cannot be used in these calculations, as it is spoiled by the overlapping Al He-α line, which is the strongest line in the emmission spectra.

The electron temperature for closely spaced arrays is displayed in Fig.59. The 8-wire 4-ray stars have higher electron temperatures, while 12- and 16-wire arrays are about the same temperature. The K-shell yields for 8- and 12-wire loads were similar, so the higher temperature alone cannot explain the higher yields, but it is consistent with the higher implosion speed of these low wire-number arrays. It should also be noted that the uncertainty of the determined temperatures are quite high, and the experimental error is high due to the low intensity of the Mg He-γ line.

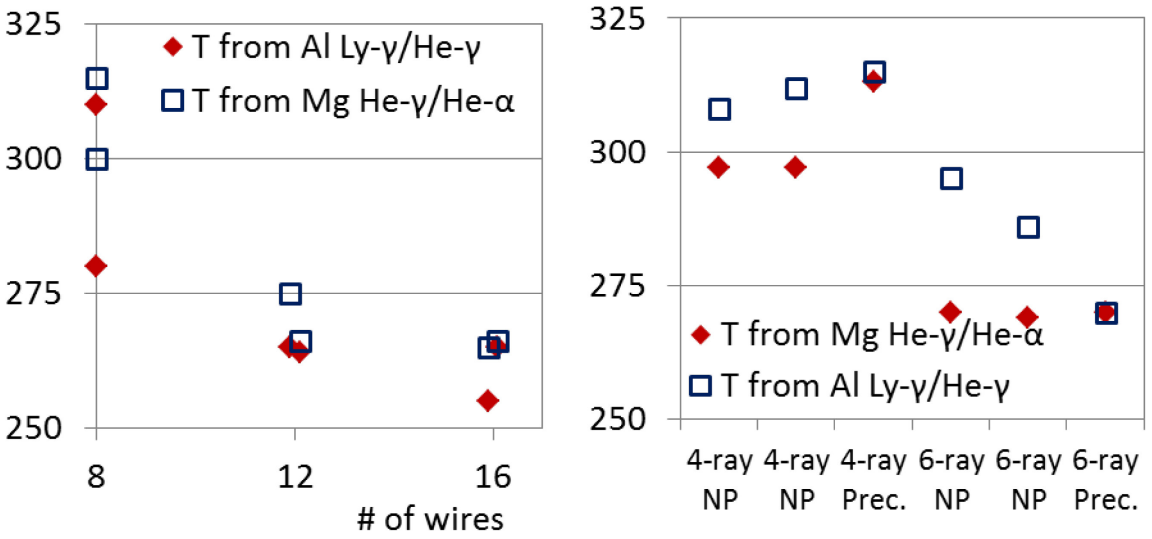

Figure 59. Electron temperature determined by Mg and Al line ratios for closely spaced loads with different wire numbers (left). Electron temperature determined by Al and Mg line ratios for star wire arrays with ('Prec.') or without ('NP') precursor (right).

The mass density determined from the He-γ/He-α line ratio varied 1.5-2.5mg/cm^3, which corresponds to a pinch radius of 0.6-0.8mm. This value is larger than pinch diameters seen in x-ray pinhole images, which might be attributed to the radiation before and after the pinch reaches its smallest diameter, or to absorption in the slightly colder plasma surrounding the pinch. At the temperatures of 250-400eV the average ionization

of the Al plasma is between 11 and 12, corresponding to electron densities of $n_e = 3\text{-}6\times10^{20}$ cm^{-1}.

An anomaly of the spectra was that the Al He-β line was much stronger in the experimental spectra than the simulations would suggest. The Al He-β/He-γ and He-β/Ly-α ratios were about 2× larger. This also suggests contribution from colder plasmas to the time integrated spectrum. Colder plasmas also have a strong He-α line, which was the strongest line in the K-shell spectrum. This could not be quantified, however. The lines are highly opaque, so errors in the atomic database would be amplified. The high intensity of the line also saturated the x-ray film, and thus the x-ray intensities could not be determined. High-order H-like Al transitions, like the Ly-γ at 5.74Å and the Ly-δ at 5.60Å, however, higher temperatures (exceeding 250eV) are needed.

4.9.3. Spectra comparison by least squares-method

The electron temperature of the plasma can also be determined by the comparison of the experimental and simulated spectra over a given wavelength range. The 5.5-6.55Å range, including higher-order He- and H-like lines and the recombination continuum, offers information about the "hot" plasma emission. Simulation parameters were the same as used in the comparison of Mg line ratios. A numerical resolution of $\lambda/\Delta\lambda=200$ was applied to the simulated spectrum to represent the source broadening of the lines.

Finding the best agreement between the experimental and simulated spectra over the given spectra range was done by a χ^2-method. The spectra were normalized over the range (so their integral would be equal), and the minimum of the sum

$$\chi^2 = \sum(I_{exp} - I_{Prism})^2 \quad (4\text{-}4)$$

was sought over the parameter space. It was found that the best temperature agreements were almost independent of the density (and thickness) of the plasma. Best temperature fits for all the investigated densities were within 10eV. Figs.60 and 61 display the best fit over the "hot" spectra between experimental and theoretical values. The summary can be seen in Fig.62 (left). The low-wire number arrays have higher temperatures than the higher-wire number arrays, as when the temperature was determined from the Mg line ratios. Determining the density is much less reliable, as the best fits suggest a very broad spread of densities, over 15mg/cm^3 in some cases, and below 2mg/cm^3 in some star arrays.

For star arrays with three wires in a ray (Fig.62, right), while the 6-ray stars had the lowest temperature, the hottest were the 4-ray stars, not the 3-ray stars, even if the latter had the strongest K-shell x-ray yields. On this part of the spectrum there was no discernible difference between precursor and non-precursor arrays.

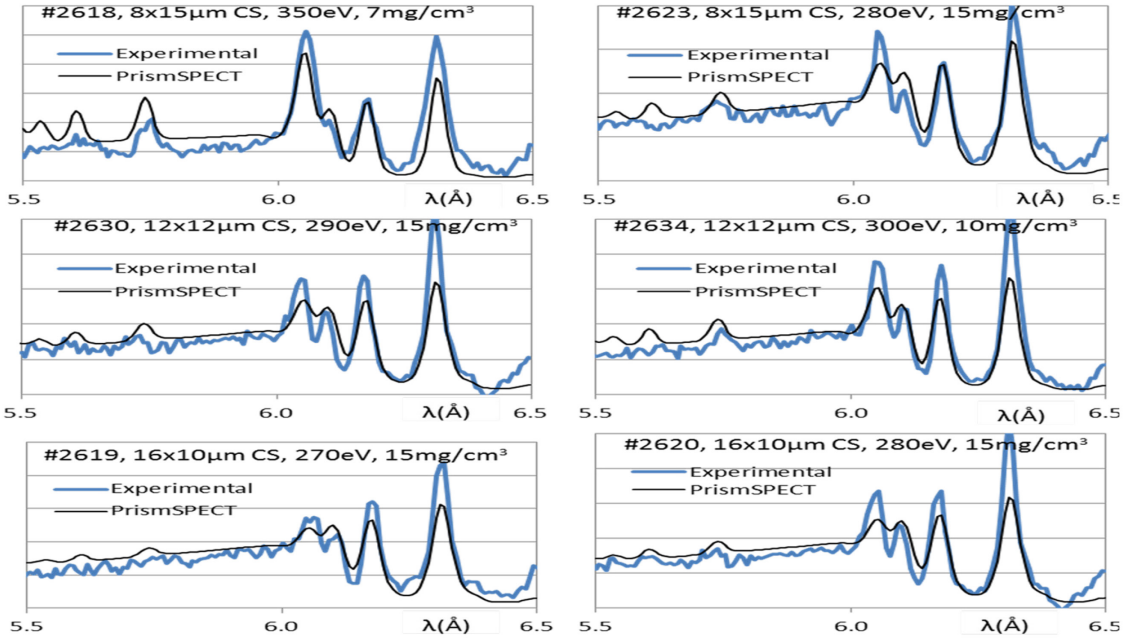

Figure 60. Best χ^2 fits for the 5.5-6.5Å spectral range of closely spaced arrays.

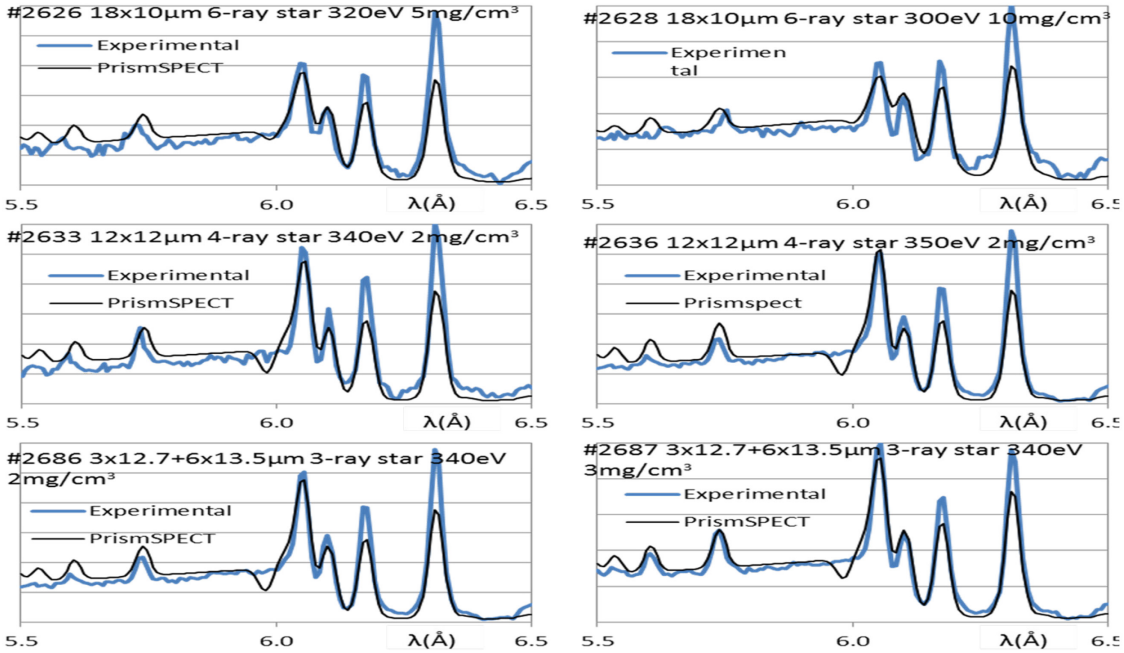

Figure 61. Best χ^2 fits for the 5.5-6.5Å spectral range of star arrays.

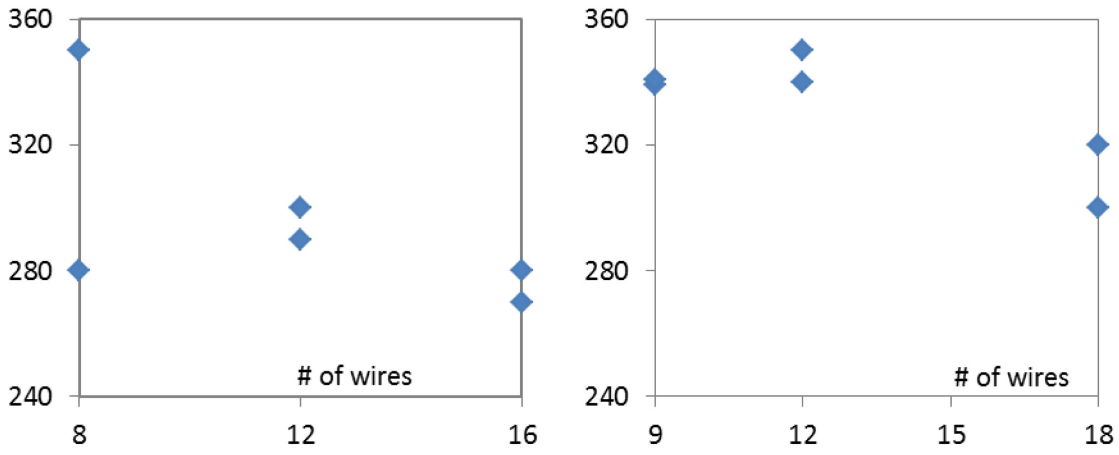

Figure 62. Electron temperature (eV) determined by best χ^2 fit for closely spaced (left) and star-like arrays (right), as a function of wire number.

4.10. Discussion

The control of the **j**×**B** force and plasma flows in closely spaced nested cylindrical and star-like wire arrays is possible during the ablation stage. In star wire arrays, the direction of the **j**×**B** force on the inner wires determined the presence of the precursor. The implosion dynamics for arrays with and without precursor were otherwise similar. Star wire arrays without precursor imploded 5ns faster than corresponding configurations with precursor. It was also found that the presence of the precursor caused a negligible but consistent reduction on the soft x-ray yield in star arrays, and a more pronounced (up to 15%) effect on the Al K-shell yield.

The lowest x-ray yields were observed in 6-wire closely spaced arrays, but similar nested arrays with ΔR=4 mm had high yields, suggesting different implosion dynamics for these loads.. Shadowgraphy of the 6-wire closely spaced loads shows the paired wires forming three plasma columns [Fig44(f)] during the implosion phase, like three pre-

pinches already breaking up from magnetic Rayleigh-Taylor instabilities during the implosion phase, before the formation of the central pinch. This can be analogous to the formation of a pair of plasma columns close to the original wire position, similar to the plasma columns in linear arrays without precursor [Ivanov2007b]. The cause for the column formation is most probably the strong attraction in the wire pairs, stronger than in 8-16-wire arrays, ending in the early merging of wire plasmas. High ablation rates, as discussed below, might also contribute to this.

The formation of plasma columns is absent in 8-wire closely spaced arrays which implode in a cascading regime, with a smooth plasma front. While the reduced-symmetry 8-wire closely spaced arrays with ΔR=0.5-1mm have similarly low soft x-ray yield to 6-wire arrays, their keV x-ray yield is one of the highest. In closely spaced wire arrays, the size of the wire gap ΔR had discernible effect only for 16-wire closely spaced loads, where loads with ΔR=0.4-0.5mm had 40-70% worse keV energy and power than loads with ΔR=1mm.

The cause for increased x-ray yield for low wire-number arrays could be the earlier implosion, and possibly higher implosion speed. In regular cylindrical arrays, the speed of imploding plasma bubbles in 8-wire loads was 200-350 μm/ns, which increased to 200-600 μm/ns in 4-wire arrays [Ivanov2007a]. However, when all $\mathbf{j}\times\mathbf{B}$ forces were summed up for all wires in these loads, this total **$\mathbf{j}\times\mathbf{B}$ force** decreased in low wire-number load. This effect is analogous to the $\mathbf{B}\sim(N-1)/N$ scaling in cylindrical wire arrays, where N is the number of wires in the array. This would suggest a reduced, not increased,

implosion speed. In Ø16/14mm (ΔR=1 mm) closely spaced arrays, the calculated total force (on all wires) in an 8-wire load is only 77% of the force in a 16-wire load.

Closely spaced arrays displayed cascading implosion dynamics similar to star arrays [Ivanov2009PRL, 2010PoP]. The ablated material from the outer wire hits the corona of the inner wire, as shown on the shadowgrams, with no plasma accumulation between the wires. The ablation starts at the outer wires, where the magnetic fields and currents are higher and both inner and outer wires ablate to the center in the late ablation stage. After the material from the outer wires is depleted, the wire cores break up and implode into the inner wires which are still at their original positions and mostly intact. In contrast, based on direction of the $\mathbf{j}\times\mathbf{B}$ forces, one would have predicted a different behavior - that the ablated plasma should accumulate in the gap between the paired wires and the wires would eventually merge.

The precursor plasma column was absent in closely spaced nested wire arrays with 6-8 wires. Despite the outward ablative forces, however, the ablation was inward on the inner wires (Figs.47, 49), and the precursor was present in closely spaced arrays with 12-16 wires. As the magnetic configuration around the wire pairs is similar in 6-8 and 12-16-wire loads, the direction and magnitude of the forces cannot account for this discrepancy. In 12-16-wire arrays with small wire gap (ΔR=0.25-.05 mm), the $\mathbf{j}\times\mathbf{B}$ forces can be stronger than in 8-wire arrays with ΔR=1 mm, but this does not prevent the formation of the precursor. This suggests a strong interaction between the closely spaced wires, so they should not be treated individually.

Increased mass ablation rate from the increasing wire diameter, as in [Yu2007], may be a possible explanation for the implosion timing and the presence/absence of the precursor. Lower wire number loads have larger wire diameters to keep array mass similar, and the mass ablation rate would be higher. Both the current through the wires and magnetic field at the wires are higher in low-wire loads, as the closest wire carries more current, increasing the local magnetic field and the ablation rate further. This increased ablation rate could explain the earlier exhaustion of the wire cores, shown in Fig49(g) and (h), and could explain the earlier implosion [Fig.44(b)] in 8-wire closely spaced arrays. The increased mass ablation rate could also decrease the ablation velocity, accounting for the absence of the precursor and the late axial plasma accumulation. This might be analogous to the absence of precursor in large diameter arrays on the Z generator [Jones2008]. To clarify the ablation behavior of the wire pairs, MHD simulations would be necessary, with a code that treats the core-corona structure correctly.

The earlier implosion in lower-wire number closely spaced arrays could be attributed to several physical causes. The cores of the larger diameter wires are exhausted earlier due to the higher mass ablation rate, which is enhanced further by the larger local magnetic fields. The implosion speeds may also be larger in lower wire number loads, as discussed above. These effects could have overcome the slight wire mass increase in the 8-, 12- and 16-wire closely spaced arrays to produce faster x-ray peaks in the lower-wire number arrays, as shown in Fig50(a).

The different implosion dynamics of cylindrical, regular nested and closely spaced wire arrays did not allow drawing unambiguous conclusions on the presence of precursor. In star wire arrays, comparable precursor and non-precursor configurations had the same cascading implosion dynamics. In these star arrays, the presence of precursor could be reliably controlled by the direction of $\mathbf{j}\times\mathbf{B}$ forces, which might be attributed to the otherwise similar implosion dynamics of precursor/nonprecursor wire array pairs. A slight decrease in x-ray yield could be attributed to the existence of precursor in star arrays.

Spectral analysis based on the time-integrated K-shell emission spectrum showed that the temperature in these star and closely spaced arrays varied between 270eV and 350eV, depending on the number of wires in the arrays, and with some shot-to-shot variation for similar loads. Lower wire (and ray) number closely spaced and star-like loads had slightly higher temperature. This is in agreement with the increased K-shell x-ray output. However, as the increase in the radiative power can be a factor of two, a temperature increase of 10% cannot account for all of it.

5. STUDY OF THE RADIATIVE PROPERTIES OF TWO-COMPONENT WIRE ARRAY AND LASER PLASMAS

The radiative properties of wire array z-pinches can be modified by the appropriate selection of wire materials. For example, the photon energy range of the K-shell radiation yield was varied in the 1.2-9keV range on the Z accelerator [Coverdale2010]. Two-component z-pinches allows further tailoring of the x-ray radiation. The most common example is the use of Al-Mg alloys with 5% Mg content, where the Mg, besides improving the mechanical strength of the wires, is providing low-opacity lines for spectroscopic analysis, e.g. in [Ivanov2009]. Incompatible material pairs, which do not form alloys of the desirable composition, cannot be studied with this method, for example refractory elements (like Ta, Mo and W) mixed with low melting-point metals like Al. AS ablation behavior is strongly material dependent, as discussed in Chapter 1, if wires of different materials are used in a pinch, further complications arise due to the improper mixing of elements. Such single and nested cylindrical wire arrays were studied previously [Deeney1995, Lebedev2002, Williamson2010, Weller2012]. Implosions dynamics in mixed wire arrays strongly depends on the actual load configuration, wire diameter and position, and it could lead to a layered pinch with different materials being dominant in the core of the pinch and surrounding it [Williamson2009].

Star and planar wire arrays, on the other hand, implode in the cascading mode. In this chapter, it will be demonstrated that this cascading implosion can be used to mix different materials. Radiative properties of the mixed z-pinch plasmas of different compositions

would be studied by spectroscopic methods. The spectrum of two-component z-pinch plasma would be compared to the spectrum of laser-produced plasmas of similar composition.

5.1. Mixing of wire materials in the cascading process

As discussed in Chapter 1, star-like and planar wire arrays implode in a cascading mode, where the plasma from the outer wires implode to the next wires to the inside, then the combined mass implodes into the net wire, and so on. The collisions in this cascading process mitigate the bubble-like implosion instability, and in star wire arrays allow the formation of a homogeneous Z-pinch [Ivanov2008].

To achieve cascading implosion in two-component star and linear arrays, some care must be taken in designing the array configuration. Low-Z wires ablate faster, and a lighter wire mass would also be depleted earlier, leading to an earlier implosion. As a simple rule, the low-mass low-Z wires should be put on the outside of the array, and a heavier, high-Z wires on the inside. Fig. 63 shows what happens if the wires are reversed in an Al-Ti planar array, with the Ti wires placed on the outside. The Al wires, despite being on the inside of the array, break up earlier and implode earlier than the Ti wires on the outside. Because of the earlier implosion of the Al wires, the x-ray pulse duration Δt is twice as long compared to a configuration where the Ti wires were on the inside. The maximum x-ray power and the keV x-ray yield were also reduced in this load.

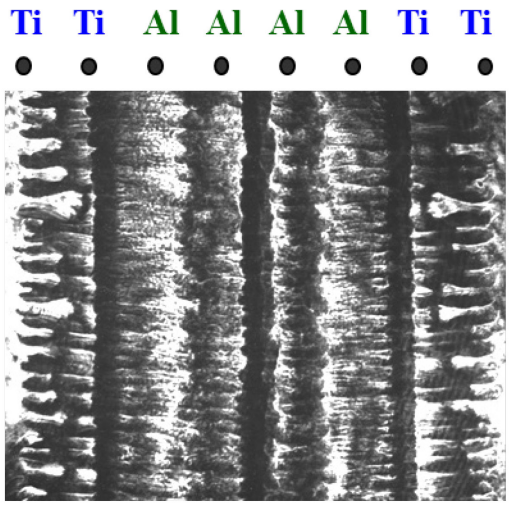

#	1691	1700
	Al-Ti	Ti-Al
E_{tot} kJ	8.5	8.6
P_{max} arb.u.	39.3	27.2
Δt ns	20	39.5
E_{keV} a.u.	71	43

Figure 63. 266nm UV shadowgram of Ti (outside) and Al (inside) imploding simultaneously in a planar array, Zebra shot #1700. Shot parameters are displayed on the right.

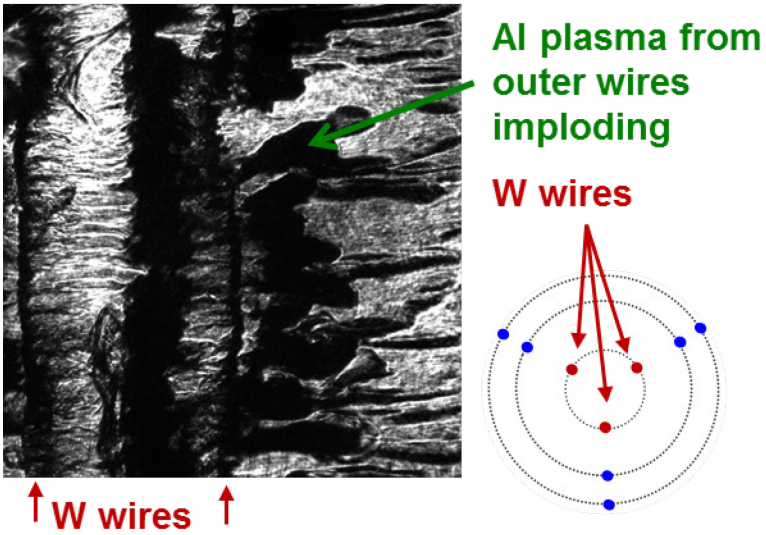

Figure 64. Shadowgram of a Al-W 9-wire star array, Zebra shot #1736, showing how the cascading implosion can mix the wire materials.

The cascading implosion allows the mixing of materials, as demonstrated in the shadowgram in Fig.64. In a 9-wire star array, the Al plasma from the outer wires implode to the plasma columns formed of the inner W wires, arriving at the central pinch together – with some Al left in the trailing mass. Getting a similar mix of Al-W from an alloy wire

is not possible (at least very impractical), given the huge discrepancy in the melting temperature of the components.

5.2. X-ray yield and x-ray spectroscopy of two-component z-pinches

Two-component wire arrays of Al and a heavier element have two distinct radiative signature. The total (mostly soft) x-ray yield, measured by the unfiltered bolometer, and the keV-range yield, measured through a PCD with a Be filter (Chapter 2, Fig. 6.) The keV-range radiation is dominantly from the K-shell line and continuum radiation of Al, with some contribution from the heavier element. These x-ray yields for two multicomponent plasmas are displayed in Fig.65, as a function of atomic composition. In Al-Ni plasmas, both of the x-ray yields have a linear dependence on the composition. Similar dependence was observed in Al-stainless steel and Al-Cu wire arrays. This dependence can be explained by a simple linear mixing of the component plasma, and a linear addition of the radiation of the components. The radiation dependence of Al-W arrays displays a departure from this behavior. The total x-ray yield of the mixed arrays is almost the same as the pure W arrays, only smaller. The presence of 7-25% W, however, almost completely suppresses the Al K-shell radiation, dropping it down to 20% of the value in pure Al-Mg loads. This effect could be explained assuming that the Al-W plasmas did not achieve as high temperatures as the pure Al plasmas, and so less energy was radiated in the keV range.

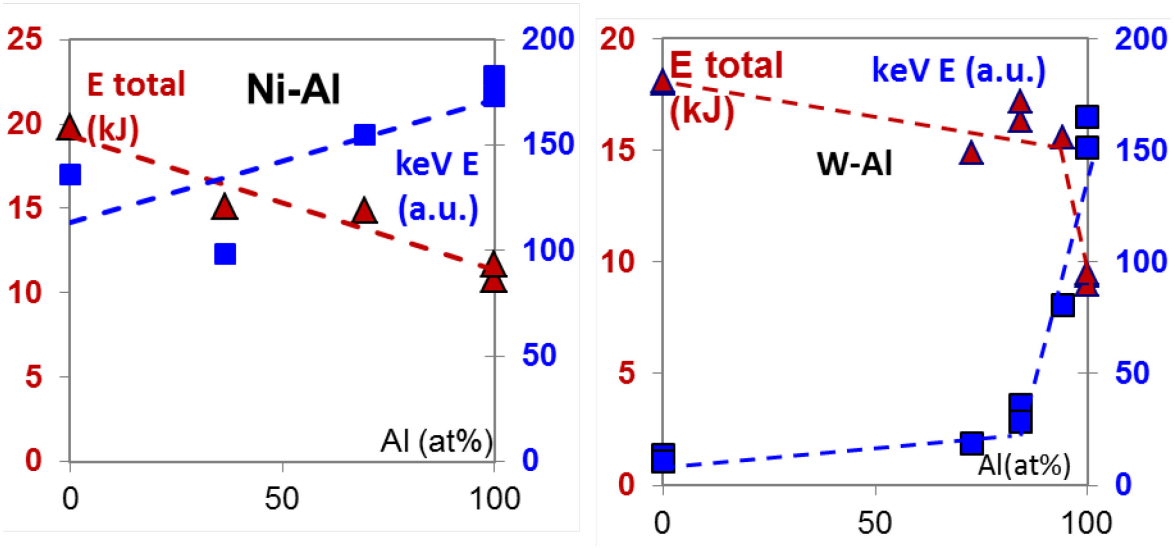

Figure 65. Soft and K-shell (keV range) x-ray yields of different two-component arrays, as a function of composition. The yields have a linear dependence on composition in the arrays with Ni, but not in the loads with W.

The cooling effect is supported by the K-shell Al spectra of the mixed star wire arrays. As seen in Fig. 66, the K-shell radiation from the tungsten-containing load has lower intensity than in Al loads, which is a qualitative indication of a colder plasma. High-energy lines are also weaker. The Mg Ly-α and the Al He-δ lines are barely discernible, while in the case of the Al-Mg plasma, higher-order lines are present. Analysis of the Al lines in these multi-component spectra used a χ^2-comparison in a parametric study [Hakel2009], where a distinct cooling effect was determined for Al-W plasmas, compared to Al plasmas.

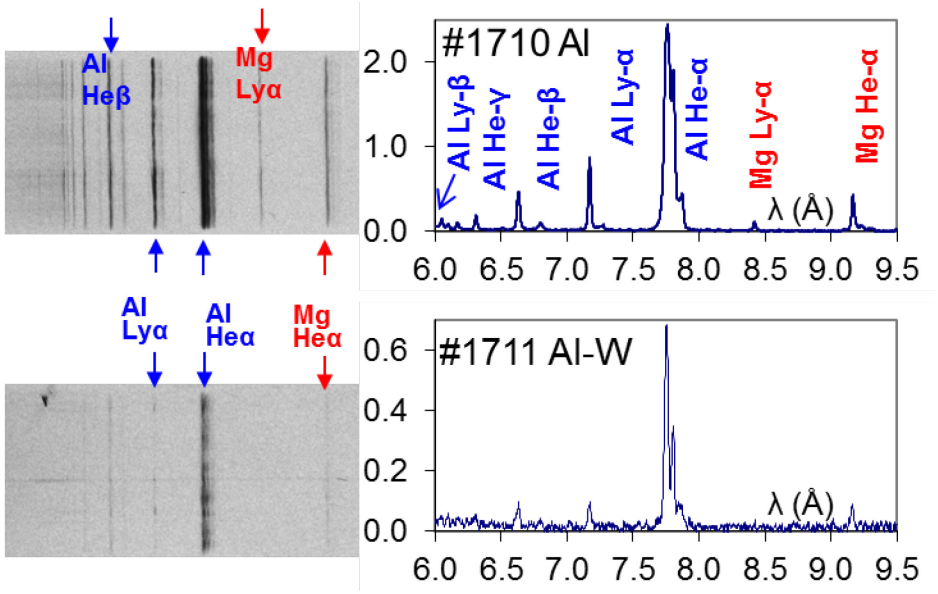

Figure 66. Time-integrated spectra recorded on the film (left) and calibrated spectra (right) for Al and Al-W star arrays. Shot #1710, Al-Mg (top), and #1711 Al-W (16at%W) on the bottom.

5.3. Spectroscopy of Al-Au Z-pinch plasmas

The effect of high-Z element in Al plasma was also investigated in linear arrays of a mass of 82-92μg/cm. The heavy mass of Au wires available precluded using star array configuration for the experiment. X-ray yields and pulse shapes for investigated arrays are shown in Fig.67. The mixed arrays displayed some reduction in K-shell yield, and stronger soft x-ray yield, more than in mid-Z elements but not to the same extent as in W arrays. This could be attributed to the difference in the mixing of planar and star-like wire arrays.

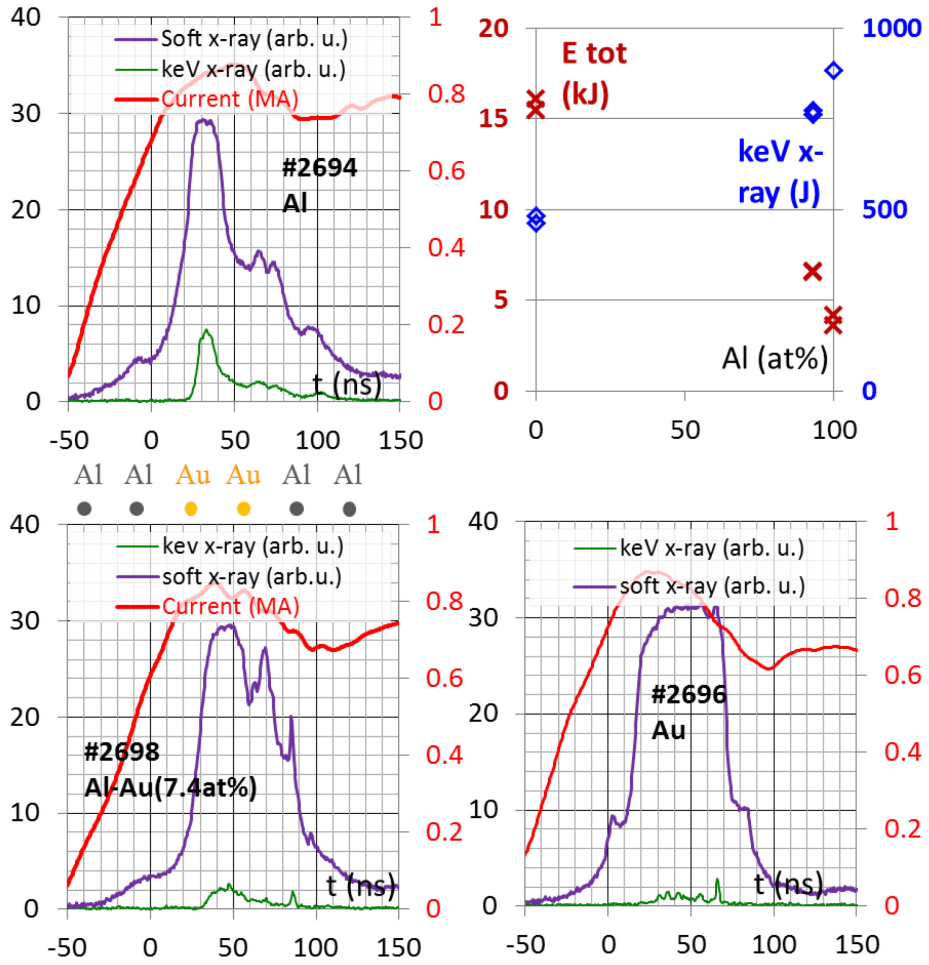

Figure 67. Pulse shapes of Al, Al-Au and Au linear arrays, and their x-ray yields.

In the time-integrated spectra of mixed Al-Au arrays, a reduction in the Al/Mg K-shell line intensity can be seen compared to Al arrays, shown in Fig.68, although not to the same extent as in the case of Al-W arrays (Fig. 66). To limit the investigated parameter space, constraints were determined based on the Z-pinch configuration. The pinch diameter was in the order of 1mm based on pinhole MCP images. The spectrometer was placed in-line with the array, so the radiation had to pass through a large plasma mass. Assuming 50-75% of the array mass imploding into the pinch, this suggests a plasma thickness around 2mm, and a density of 3mg/cm^3, so the best fits should be

sought close to these parameters. A uniform $\lambda/\Delta\lambda=250$ resolution was also applied within the PrismSPECT code, representing the source broadening, to reproduce line broadening in the spectra.

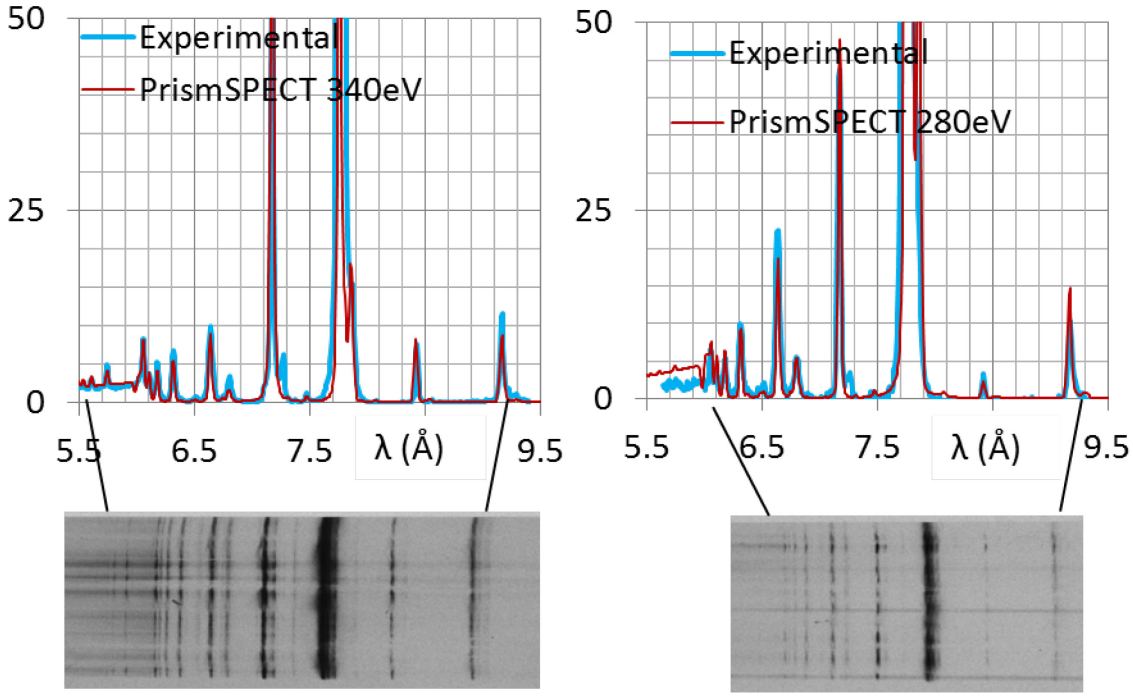

Figure 68. Calibrated experimental and synthetic spectra for Al(Mg) planar load (left), shot #2693, 80µg/cm mass, PrismSPECT fit parameters 340eV, 2mg/cm^3, 2mm thickness, $n_e=2\times10^{19}$ cm^{-3}; Al(Mg)-Au load, 80µg/cm mass, 7.4at% Au (right), shot #2397, PrismSPECT fit parameters 280eV, 280eV, 1mg/cm^3, 2mm, $n_e=1\times10^{19}$ cm^{-3}.

The "best fit" synthetic spectra were not unambiguous, however. While not that significant for Al loads, for the Al-Au loads, using different regions for a χ^2 fit resulted in electron temperatures in the range of 200-300eV. The recombination continuum on the Au-Al spectra suggests even lower Al densities, i.e. 25% of the Al-Mg loads, not only half of it.

Some further features were noticeable on the Al spectra. The Al He-α line, even when not oversaturating the film, was a factor of 2-3 stronger than the synthetic spectra would suggest. The Al He-β line was similarly stronger compared to the higher-order lines, or the Al Ly-α. These features agree with the points to inhomogeneous pinch. The spectra in Fig.68 show several hotspots, with strong continuum radiation displayed in dark horizontal lines. This might be similar to the strong blackbody radiation present in X-pinches [Shelkovenko2002]. Those hot spots and colder regions alternate along the pinch. There is also colder plasma surrounding the hot, denser core – or the colder plasma before/after the peak of the implosion phase. The satellite lines were also stronger than the simulations would suggest, especially the satellites of the Al Ly-α line. While a possible explanation for this is colder radiating regions in the pinch, this could be caused by e-beam effects in the pinch, which beams might modify the population balance of the ionization levels.

The Al He-like recombination edge is present on the synthetic spectra, but not in the experimental one – the continuum should be separated from the high-order lines despite the low spectral resolution. Continuum edge shift due to electron density is taken into account by the PrismSPECT code, and it would be in the order of only 5-10eV at these densities.

A more consistent way to compare the temperatures in these loads is by using ratios of selected lines, ones that do not have a large dependence on the plasma density. The ratio of Mg and Al satellites to the main lines, like in [Ivanov2009] could not be used, as the lower spectral resolution (~150 compared to ~350) did not resolve the satellite lines

from each other or the spectrum, so main line ratios had to be used. The T_e-dependence of line ratios, determined using PrismSPECT, and temperatures determined are shown in Fig.69. The sensitivity to density of applicable line ratios, however, was very low, in general - below 40% over the investigated density regime (0.5-5mg).

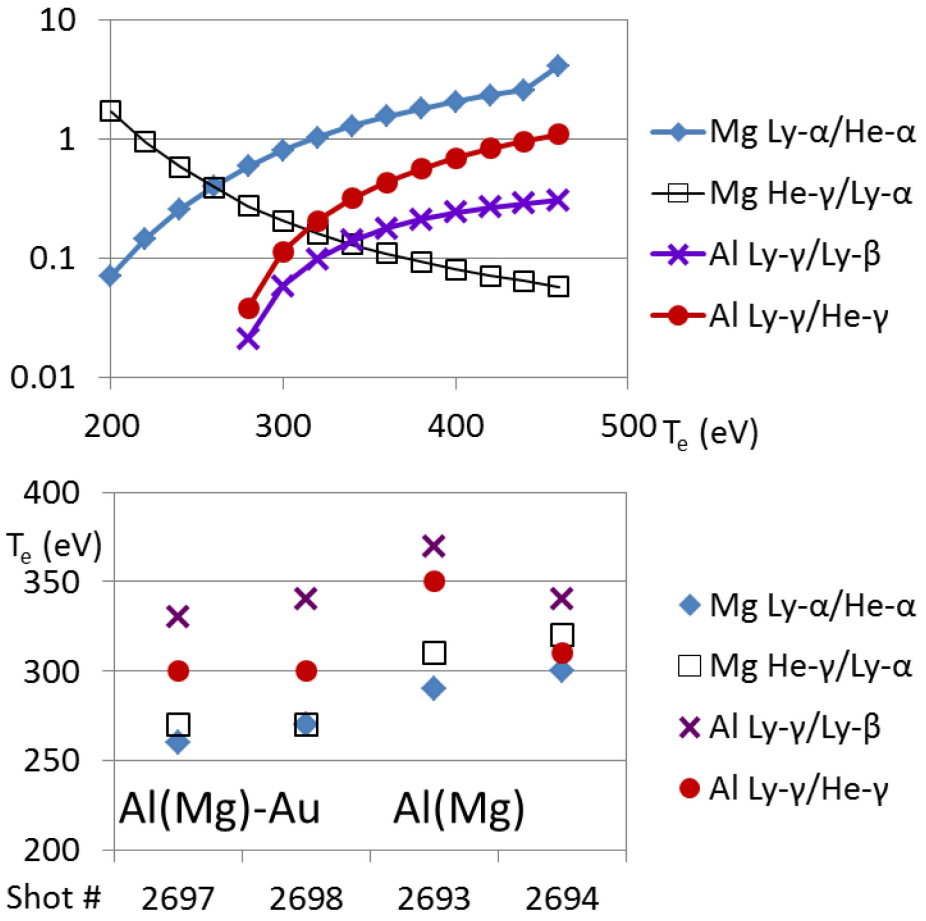

Figure 69. Ratios of selected Al/Mg lines (semilog plot) as a function of temperature (top). Temperatures corresponding to the experimental ratios for these line ratios (below).

While the temperatures determined for a given shot varied up to 100eV for different line ratios, the plasmas that contained Au were consistently colder for each line ratio, than the Al-Mg plasmas, with an average cooling of 40eV. Temperatures determined from the Mg lines were consistently lower than from Al lines. This can be explained by

that all Al lines were of higher energy (over 2keV), they would not be excited to the same extent in a colder plasma, thus are more representative of the hot regions of the pinch. The lower-energy (1.3 to 1.7keV) Mg lines, however, would also be excited in the lower-temperature parts of the pinch, and are more global indicators.

5.4. K-shell spectroscopy of two-component laser-produced plasmas

To complement the two-component Z-pinch study, similar experiments were done with the Leopard laser in the Phoenix target chamber (Chapter 2, Fig.13). The Al plasmas produced by Z-pinch and by the Leopard laser (in the ns regime) are similar, with electron temperatures of 200-500eV and an average ionization of Z~9-11, depending on the laser energy and focusing conditions. The L-shell electrons are almost fully ionized, but as the ionization energy of Al^{11+} is 2086eV, much larger than the plasma temperatures.

A schematic of the experimental arrangement is shown in Fig.70. The laser beam was focused on the target with a 50cm lens, and the spectrum was recorded by a convex KAP crystal spectrometer, and a cylindrical von Hamos spectrometer – the latter did not provide good quality data due to resolution limits (~150-200) of the low-quality mica crystal used in the spectrometer.

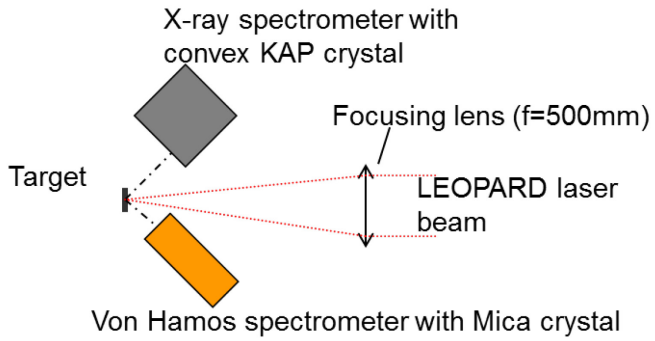

Figure 70. The schematics of the laser plasma spectroscopy experiment

To produce the two-component laser plasma, Al alloys with Cu and Au were produced at the Materials Science lab with the help of Dr. Tim Darling. These were bulk targets, made to different material compositions, then polished. In the target that was manufactured with 5:3 Al:Au mass ratio, an intermetallic Al_2Au compound precipitated, resulting in a gold-rich part with ~30at% Au content, and a gold-depleted part with ~3at% gold.

To constrain the plasma size and density to construct the synthetic spectra, an energy balance calculation was made to determine the number of atoms, assuming 25% absorption, in accordance with [Price1995]. The plasma size, assuming a hemispheric expansion, was determined from the source broadening of the lines (eqn. 2-13) to be around 280μm in radius and thickness with a density of about 0.1mg/cm^3, and was in agreement with plasma simulations [Sawada2012]. These parameters were used in the PrismSPECT calculations. Density and thickness dependence of the (synthetic) spectra was not studied, as these parameters adequately reproduced the experimental spectra, including the satellite lines. A uniform $\lambda/\Delta\lambda=350$ resolution was also applied to the

synthetic spectra to represent source broadening. It should be noted, however, that the source broadening is not strictly uniform for the whole spectra.

In comparing the experimental and synthetic spectra for the different target materials, only the four strongest Al lines were present in all of the spectra, i.e. the He-α, He-β, He-γ and Ly-α lines. Some of the satellite lines and higher-order He-like lines were resolvable on the pure Al targets, but not in the alloys. In the "best fit" over the experimental pure Al spectra, when the higher-order lines were considered, T_e~460-480eV was determined (Fig.71). The optical depth even of the He-α line was below 5 for these parameters, compared to an optical depth of ~500 in Z-pinch plasmas, so the line could be used in the comparison.

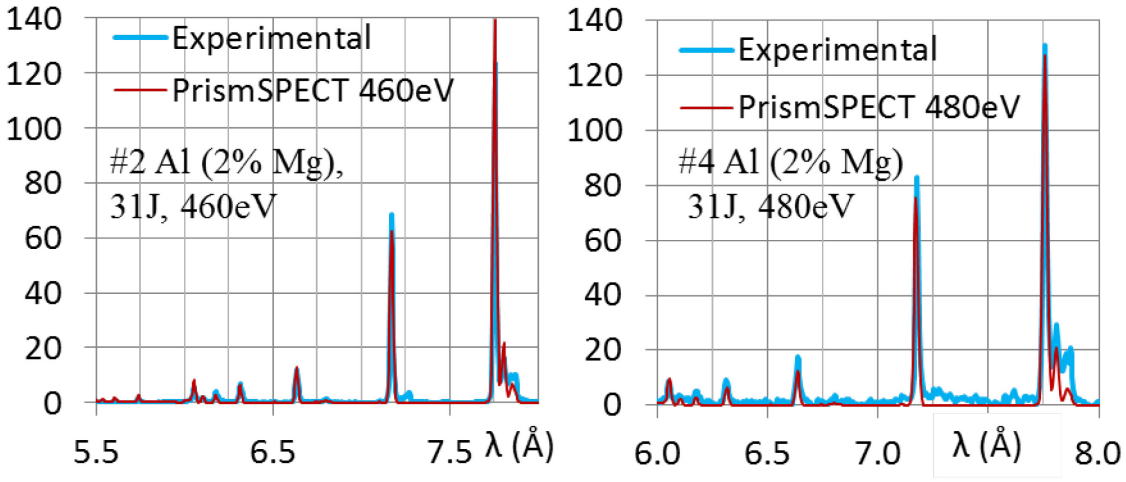

Figure 71. Calibrated experimental and best-fit synthetic spectra for Al (2%Mg) laser targets. Shot energies and simulation temperatures are displayed. Temperatures determined from line ratios were 440eV for both loads.

The satellite lines were not discernible in some of the shots (e.g. Shot #13 Fig. 72), so another consistent method was used to determine the electron temperatures. The ratios of the four main lines (without satellites) were used, of which four 'cyclic' line ratios (He-α

/He-β, He-β/He-γ, He-γ/Ly-α and Ly-α/He-α) were selected to provide equal weight to each lines. The fitting criterion was that the sum of the divergence between the experimental and theoretical value would be minimal:

$$\sum \left(\frac{Exp.ratio}{Theo.ratio} - 1\right)^2.$$

At the best fit of these lines, the sum was below 0.06, suggesting less than 20% difference between the experimental and simulated line ratios. For both Al targets displayed in Fig. 71, the temperature determined by this method was 440eV.

The experimental and simulated spectra at the temperatures determined by this method for multicomponent targets are shown in Fig.72. The temperatures were in the 430-460eV range, even for alloys that contained 30at% Au. As similar temperatures were determined for the Al(Mg) targets, we can conclude that no cooling effect was observed in laser produced multicomponent plasmas with high-Z elements.

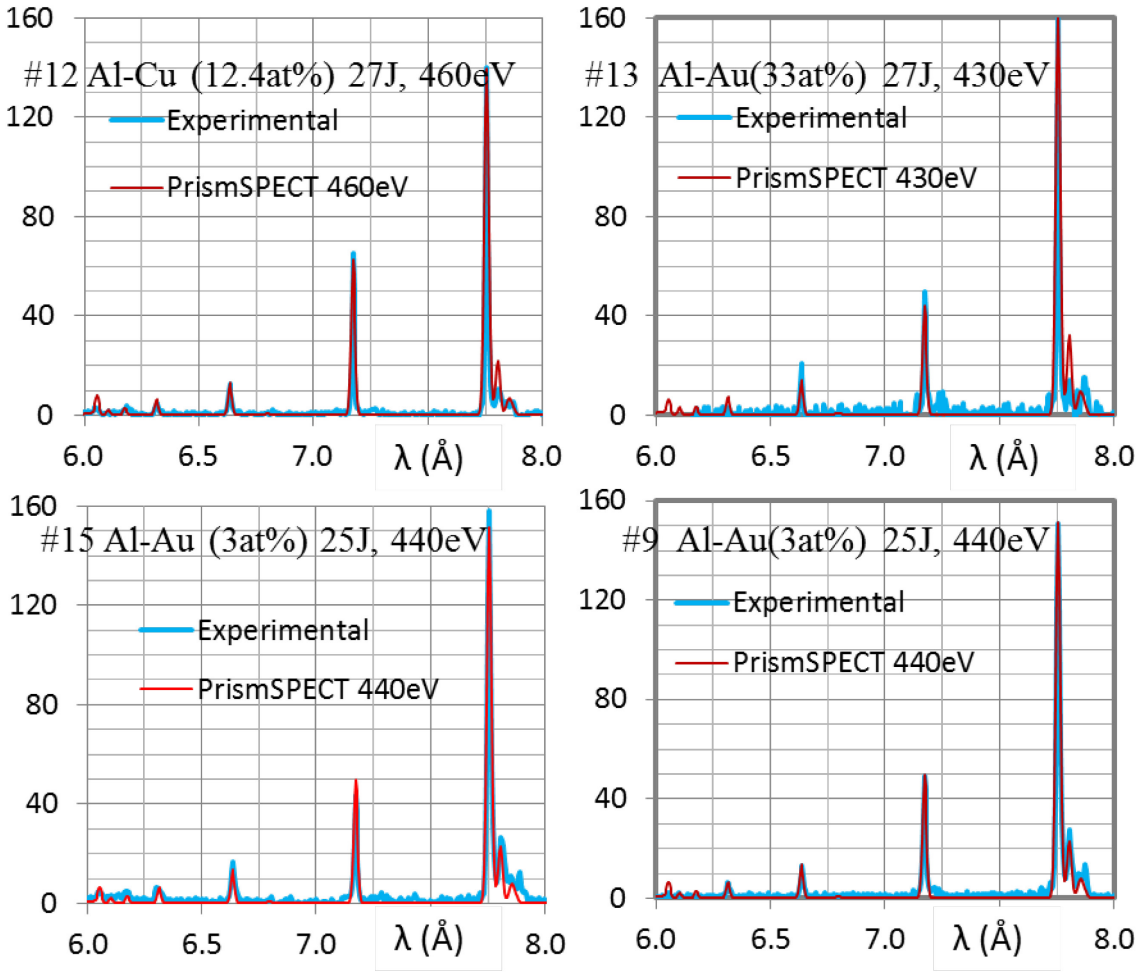

Figure 72. Calibrated experimental and synthetic spectra for Al alloyed laser targets. Shot energies and simulation temperatures are displayed. Temperatures were determined form line ratios.

5.5. Comparison of two-component Z-pinch and laser-produced plasmas

X-ray K-shell emission spectra of Al was recorded and analyzed for both Z-pinch and laser-produced plasmas, where the Al was mixed with higher-Z elements. The calibrated experimental spectra were compared with synthetic spectra using the PrismSPECT code. Using the ratio of selected lines, it was determined that a cooling effect in the order of 40eV exists in Au-Al Z-pinch plasmas. One other study showed a more significant

cooling in Al-W plasmas. Comparing the soft and keV-range x-ray yield of different material compositions, only Al plasmas with high-Z elements (Au and W) displayed a disproportionate decrease of the Al K-shell radiation which was not observed for mid-Z elements (Fe, Ni, Cr and Cu) mixed with Al.

Other features of the z-pinch spectra were also observed, like strong He-α and He-β lines, most probably from the lower temperature plasmas, in agreement with the inhomogeneous nature of the pinch. Satellite lines of Al were also strong, which might be attributed to e-beams in the pinch, or colder radiating regions.

Laser-produced Al-Au plasmas, however, showed similar temperatures to Al(Mg) plasmas, so the cooling effect is not pronounced in laser-produced plasmas, only in Z-pinches. The reason for this discrepancy might be found in the different heating mechanisms. In laser plasmas, the electrons are heated by the electromagnetic radiation. In Z-pinch plasmas, however, besides Ohmic heating, a significant portion of the heating comes from plasma imploding into the pinch, converting the kinetic energy of the ions to thermal energy.

6. CONCLUSIONS

The ablation and implosion phase of nested cylindrical and star wire arrays were studied with a variety of optical, laser-probing and x-ray diagnostics. To study the azimuthal development of the implosion, a 532nm end-on probing setup was implemented. The setup was modified for the use of 266nm end-on probing. A polarization-separated two-frame delay system was built for the UV beampath to study the temporal evolution of the pinch. This UV two-frame end-on probing was able to fully penetrate a stagnating Al pinch – a 1cm-tall column with an estimated electron density of $n_e \sim 10^{20}$ cm^{-3}.

A numerical scheme was implemented in MATLAB to calculate the current distribution in wire arrays, based on inductive current division, and to determine the magnitude and direction of the ablative $\mathbf{j} \times \mathbf{B}$ forces. The scheme allowed a more proper qualitative description of wire array ablation, and also allowed the design of wire arrays where the presence of the precursor plasma column was controlled.

A modified, “gated” star wire array configuration was used to simulate the implosion modes of nested cylindrical arrays, the transparent and nontransparent regimes. Gated arrays with regular-length wires implode in the nontransparent mode, where the gate wires trap the imploding plasma. To simulate the nontransparent implosion, the current through the gate wire was decreased using longer gate wires, and higher-Z wire materials. The imploding plasma passing between the gate wires was resolved by using 266nm UV laser probing, which improved plasma penetration.

Star arrays were also used in experiments with the aim to produce a rotating pinch, where offsetting the inner wires azimuthally adds a radial component to the magnetic field. The rotation would increase the stability of the pinch. Side-on probing showed an atypical bent pinch that suggested some rotation. End-on UV probing of such loads, however, did not offer any conclusive evidence.

Nonprecursor implosions were created using closely spaced nested arrays with 6-8 wires, in which the direction of magnetic field at the inner wires was reversed, and ablative forces pointed outward. In 12-16-wire closely spaced arrays, however, the precursor was present despite the outward ablative forces on the inner wires. Centerward ablation was present on the inner wires, despite the outward **j**×**B** forces. The discrepancy in the presence of precursor in closely spaced nested arrays could possibly be explained by difference in the ablation speed. Larger-diameter wires in lower-wire number loads broke up earlier than smaller-diameter wires in arrays of the same mass, suggesting faster mass ablation rate for larger wires. As the ablative forces are similar, the velocity of the ablating plasma in the low-wire number arrays would be lower, and the plasma would not reach the array axis before the main implosion.

The keV-range Al K-shell radiation in investigated nested arrays was dependent on the number of wires (and rays), and was the largest for 6-8-wire regular nested arrays and 8-wire closely spaced arrays. The pulse shape of closely spaced arrays was reproducible. The low-wire number arrays also had earlier implosions for similar array mass.

To study the stabilization effect of the precursor, star-like wire arrays were designed to implode with or without a precursor. The direction of the **j**×**B** forces on the inner

arrays agreed with the presence or absence of the precursor in star arrays. Arrays without a precursor showed an improvement of 3-15% in x-ray yield parameters, particularly keV-range x-ray yield, suggesting that the precursor degrades the quality of the pinch. Low-wire number star arrays produced higher keV-range x-ray yield, agreeing with the results for nested arrays. Spectroscopic analysis of star and closely spaced arrays showed generally higher electron temperatures for low-ray number arrays.

The radiative properties and x-ray spectra of mixed plasmas were investigated in both Z-pinch and laser-produced plasmas. In Z-pinch plasmas with mid-Z elements, no cooling was observed. In Al-W and Al-Au arrays a reduction of K-shell yield and cooling effects were observed compared to Al(Mg) plasmas, which cooling was quantified as approximately 40eV for Al-Au plasmas. In Mixed Al-Au laser plasmas produced by the Leopard laser the temperature did not decrease. This discrepancy could possibly be attributed to the different heating mechanisms in Z-pinch and laser plasmas.

The developed end-on probing provides unique opportunity to study the azimuthal evolution in wire array (and also liner) implosions. With a higher-quality laser probing beam, interferometry and laser absorption could be used to determine plasma parameters. Higher frequency lasers, e.g. 5ω Nd:Glass at 211nm, would permit the investigation of even denser plasmas. Faraday rotation imaging could be used to study the axial fields created by the final pinch, or the evolution of externally applied axial magnetic fields. The azimuthal magnetic field could be studied using the Voigt (Cotton-Mouton) effect. These methods would enable the study of magnetic field convection in dense plasmas. Such diagnostics may also be implemented on higher-current generators.

To better describe the complex ablation behavior in the closely spaced nested arrays, 2D and 3D MHD simulations would be necessary, as simple models do not explain the observed behavior. The trends observed in the keV-range yield for Al arrays could be used to optimize K-shell production in wire arrays. On the Zebra generator, large diameter, light 3-ray star Al arrays without precursor might provide improvement in keV x-ray yield.

The x-ray spectroscopy methods used to study Z-pinch and laser plasmas could be developed into a routine technique for axially-resolved determination of electron temperature in Al-Mg Z-pinches. The measured properties of the Al He-like recombination continuum might also provide an alternative method for electron density measurements.

TABLE OF NOTATIONS

This section contains the notations generally used in the text, unless specified otherwise.

a	pulse shape-dependent generator parameter
B	magnetic field vector
B	mangitude of mangetic field
B_0	0^{th} order (constant) component of B
B_θ	azimuthal component of magnetic field
B_z	magnetic field parallel to wave propagation
β	Faraday rotation angle
c	speed of light in vacuum
C	convergence ratio, r_0/r_{min}
d	crystal lattice constant
e	elementary electric charge
ϵ_0	electry permittivity of free space
f	focal length
φ	phase shift of a wave
Φ	magnetic flux
h	array height
I	electric current
I	maximum electric current
I_{PB}	Pease-Braginskii current
I_{exp}	x-ray intensity, experimental
I_{Prism}	x-ray intensity, theoretical
j	current density
k	wave number
κ	absorption coefficient
l	plasma thickness
L	magnetic inductance
ln Λ	Coulomb logarithm
λ	wavelength
$\delta\lambda$	wavelength resolution
m	mode/order number
$\hat{m}$	linear mass
$\dot{m}$	mass ablation rate
μ	magnetic permeability
μ_0	magnetic permeability of space
N	number of wires in a Z-pinch
n_c	critical electron density
n_e	electron density
n_i	ion density
Ø	diameter
$P_{x\text{-}ray}$	incident x-ray power
p_{kin}	kinetic pressure
p_{mag}	magnetic pressure
Π	scaling parameter for Z-pinches
R	array outer radius
R_W	wire radius
ΔR	array spacing in nested arrays
r_{wire}	wire radius
r	radius
r_0	initial array radius
r_{min}	minimum pinch radius
ρ	normalized radius
ρ_0	plasma density
T_e	electron temperature
T_i	ion temperature
t	time
t_0	current rise-time
θ	refraction/incidence angle
V	voltage
v_a	Alfvén speed of plasma
W_{kin}	kinetic energy (per unit length)
x	spatial coordinate
y	spatial coordinate
z	spatial coordinate along axis or direction of wave propagation
Z	(average) ion charge
ω	angular frequency
ω_p	angular plasma frequency

BIBLIOGRAPHY

[Ampleford2007] D. J. Ampleford, S. V. Lebedev, S. N. Bland, S. C. Bott, J. P. Chittenden, C. A. Jennings, V. L. Kantsyrev, A. S. Safronova, V. V. Ivanov, D. A. Fedin, P. J. Laca, M. F. Yilmaz, V. Nalajala, I. Shrestha, K. Williamson, G. Osborne, A. Haboub, and A. Ciardi, "Dynamics of conical wire array Z-pinch implosions", Physics of Plasmas **14**, 102704 (2007)

[Alexandrov2002] V. V. Alexandrov, I. N. Frolov, M. V. Fedulov, E. V. Grabovsky, K. N. Mitrofanov, S. L. Nedoseev, G. M. Oleinik, I. Yu. Porofeev, A. A. Samokhin, P. V. Sasorov, V. P. Smirnov, G. S. Volkov, M. M. Zurin, and G. G. Zukakischvili, "Prolonged Plasma Production at Current-Driven Implosion of Wire Arrays on Angara-5-1 Facility", IEEE Transactions on Plasma Science **30**, 559 (2002)

[Bennett1934] W. H. Bennett, "Magnetically Self-Focusing Streams", Physical Review **45**, 890 (1934)

[Bland2003] S. N. Bland, S. V. Lebedev, J. P. Chittenden, C. Jennings, and M. G. Haines, "Nested wire array Z-pinch experiments operating in the current transfer mode", Physics of Plasmas **10**, 1100 (2003)

[Bland2004] S. N. Bland, S. V. Lebedev, J. P. Chittenden, D. J. Ampleford, and G. Tang, "Use of linear wire array Z pinches to examine plasma dynamics in high magnetic fields", Physics of Plasmas **11**, 4911 (2004)

[Bland2009] S. N. Bland, personal communication, 2009

[Bott2007] S. C. Bott, S. V. Lebedev, D. J. Ampleford, S. N. Bland, J. P. Chittenden, A. Ciardi, M. G. Haines, C. Jennings, M. Sherlock, G. Hall, J. Rapley, F. N. Beg, and J. Palmer, "Dynamics of cylindrically converging precursor plasma flow in wire-array Z-pinch experiments", Physical Review E **74**, 046403 (2007)

[deBroglie1914] M. de Broglie and F-A. Lindemann, "Sur un nouveau procédé permettant d'obtenir très rapidement les spectres des rayons de Röntgen", Comptes rendus hebdomedaires des Académie des sciences **158**, 944 (1914)

[Chandler1999] G. A. Chandler, C. Deeney, M. Cuneo, D. L. Fehl, J. S. McGurn, R. B. Spielman, J. A. Torres, J. L. McKenney, J. Mills, and K. W. Struve, "Filtered x-ray diode diagnostics fielded on the Z accelerator for source power measurements," Review of Scientific Instruments **70**, 561 (1999)

[Chuvatin2006] A. S. Chuvatin, L. I. Rudakov, A. L. Velikovich, J. Davis, and V. I. Oreshkin, "Heating of on-axis plasma heating for keV x-ray production with z-pinches", IEEE Transactions on Plasma Science **33**, 739 (2006)

[Chuvatin2009] A. S. Chuvatin, V. L. Kantsyrev, L. I. Rudakov, M. E. Cuneo, A. L. Astanovitskiy, R. Presura, A. S. Safranova, A. A. Esaulov, W. Cline, K. M. Williamson, I. Shrestha, M. F. Yilmaz, G. C. Osborne, M. Weller, T. Jarrett, B. LeGalloudec, V.

Nalajala, T. D. Pointon, and K. A. Mikkelson, "Design and Testing of a Load Current Multiplier on Zebra Facility", AIP Conference Proceedings **1088**, 253 (2008)

[Coverdale2002] C. A. Coverdale, C. Deeney, M. R. Douglas, J. P. Apruzese, K. G. Whitney, J. W. Thornhill, and J. Davis, "Optimal wire-number range for high x-ray power in long implosion-time aluminum z pinches", Physical Review Letters **88**, 065001 (2002)

[Coverdale2010] C.A. Coverdale, B. Jones, D.J. Ampleford, J. Chittenden, C. Jennings, J.W. Thornhill, J.P. Apruzese, R.W. Clark, K.G. Whitney, A. Dasgupta, J. Davis, J. Guiliani, P.D. LePell, C. Deeney, D.B. Sinars, and M.E. Cuneo, "K-shell x-ray sources at the Z Accelerator", High Energy Density Physics, Vol. **6**, 143 (2010)

[Cuneo2001] M. E. Cuneo, R. A. Vesey, J. L. Porter, Jr., G. A. Chandler, D. L. Fehl, T. L. Gilliland, D. L. Hanson, J. S. McGurn, P. G. Reynolds, L. E. Ruggles, H. Seamen, R. B. Spielman, K. W. Struve, W. A. Stygar, W. W. Simpson, J. A. Torres, D. F. Wenger, J. H. Hammer, P. W. Rambo, D. L. Peterson and G. C. Idzorek, "Development and characterization of a Z-pinch-driven hohlraum high-yield", Physics of Plasmas **8**, 2257 (2001)

[Cuneo2005] M. E. Cuneo, E. M. Waisman, S. V. Lebedev, J. P. Chittenden, W. A. Stygar, G. A. Chandler, R. A. Vesey, E. P. Yu, T. J. Nash, D. E. Bliss, G. S. Sarkisov, T. C. Wagoner, G. R. Bennett, D. B. Sinars, J. L. Porter, W. W. Simpson, L. E. Ruggles, D. F. Wenger, C. J. Garasi, B. V. Oliver, R A. Aragon, W. E. Fowler, M. C. Hettrick, G. C. Idzorek, D. Johnson, K. Keller, S. E. Lazier, J. S. McGurn, T. A. Mehlhorn, T. Moore, D. S. Nielsen, J. Pyle,S. Speas, K. W. Struve, and J. A. Torres, "Characteristics and scaling of tungsten-wire-array z-pinch implosion dynamics at 20 MA," Physical Review E, **71**, 046406 (2005)

[Davis1997] J. Davis, N. A. Gondarenko, and A. L. Velikovich, "Fast commutation of high current in double wire array Z-pinch loads", Applied Physics Letters **70**, 170 (1997)

[Deeney1991] C. Deeney, T. Nash, R. R. Prasad, L. Warren, K. G. Whitney, J.W. Thornhill, and M. C. Coulter, "Role of the implosion kinetic energy in determining the kilovolt x-ray emission from aluminum-wire-array implosions", Physical Review A **44**, 6762 (1991)

[Deeney1995] C. Deeney, P. D. LePell, B.H. Failor, S. L. Wong, J. P. Apruzese, K. G. Whitney, J. W. Thornhill, J. Davis, E. Yadlowsky, R. C. Hazelton, and J. J. Moschella, T. Nash, and N. Loter, "Increased kilo-electron-volt x-ray yields from Z-pinch plasmas by mixing elements of similar atomic numbers", Physical Review Letters **51**, 4823 (1995)

[Deeney1998] C. Deeney, M. R. Douglas, R. B. Spielman, T. J. Nash, D. L. Peterson, P. L'Eplattenier, G. A. Chandler, J. F. Seamen, and K. W. Struve, "Enhancement of X-Ray Power from a *Z* Pinch Using Nested-Wire Arrays", Physical Review Letters **81**, 4883 (1998)

[Fedin2004] D. A. Fedin, "Experimental characterization of high-current X-pinch plasma source and study of the influence of an energetic electron beam on source parameters", PhD Thesis, University of Nevada, Reno, Reno, NV, 2004.

[Gilfrich1975] J. V. Gilfrich, D. B. Brown, and P. G. Burkhalter, "Integral reflection coefficient of x-ray spectrometer crystals", Applied Spectroscopy **29**, 322 (1975)

[Gourdain2010] P.-A. Gourdain, I. C. Blesener, J. B. Greenly, D. A. Hammer, P. F. Knapp, B. R. Kusse, and P. C. Schrafel, "Initial experiments using radial foils on the Cornell Beam Research Accelerator pulsed power generator", Physics of Plasmas **17**, 012706 (2010)

[Haines2006] M. G. Haines, P. D. LePell, C. A. Coverdale, B. Jones, C. Deeney, and J. P. Apruzese, "Ion Viscous Heating in a Magnetohydrodynamically Unstable Z Pinch at Over 2×10^9 Kelvin", Physical Review Letters **96**, 075003 (2006)

[Haines2011] M. G. Haines, "A review of the dense Z-pinch", Plasma Physics and Controlled Fusion, **53**, 093001 (2011)

[Hakel2009] P. Hakel, V. Ivanov, T. Durmaz, R. C. Mancini, J. M. Kindel, A. L. Astanovitskiy, A. Haboub, S. D. Altemara, and D. Papp, "X-Ray Spectroscopy of Z-pinches in Implosions of Wire Arrays with Combined Materials", presented at ICOPS 2009, San Diego CA (unpublished)

[Hammer1996] J. H. Hammer, J. L. Eddleman, P. T. Springer, M. Tabak, A. Toor, K. L. Wong, G. B. Zimmerman, C. Deeney, R. Humphreys, T. J. Nash, T. W. L. Sanford, R. B. Spielman, and J. S. DeGroot, "Two-dimensional radiation-magnetohydrodynamic simulations of SATURN imploding Z pinches", Physics of Plasmas **3**, 2063 (1996)

[Harvey-Thompson2012] J. Harvey-Thompson, S.V. Lebedev, S. Patankar, S. N. Bland, G. Burdiak, J. P. Chittenden, A. Colaitis, P. De Grouchy, H.W. Doyle, G. N. Hall, E. Khoory, M. Hohenberger, L. Pickworth, F. Suzuki-Vidal, R. A. Smith, J. Skidmore, L. Suttle, and G. F. Swadling, "Optical Thomson Scattering Measurements of Plasma Parameters in the Ablation Stage of Wire Array Z Pinches", Physical Review Letters **108**, 145002 (2012)

[Hu2005] M. Hu and B. R. Kusse, "Study of plasma dynamics affected by a global magnetic field in linear wire array Z pinches", Physics of Plasmas **12**, 102701 (2005)

[Hutchinson2002] I. H. Hutchinson, Principles of Plasma diagnostics, 2nd. ed. (Cambridge University Press, Cambridge, UK, 2002)

[Ivanov2006a] V.V. Ivanov, G.S. Sarkisov, P.J. Laca, V.I. Sotnikov, V.L. Kantsyrev, B. Jones, C.A. Coverdale, P.D. LePell, C. Deeney, K.W. Struve, A.L. Astanovitskiy, D.A. Fedin, B. Le Galloudec, V. Nalajala, I. Shrestha, and T.E. Cowan, "Investigation of Magnetic Fields in 1-MA Wire Arrays and X-Pinches", IEEE Transactions on Plasma Science **34**, 2247 (2006)

[Ivanov2006b] V. V. Ivanov, V. L. Kantsyrev, V. I. Sotnikov, D. A. Fedin, A. L. Astanovitskiy, B. Le Galloudec, V. Nalajala, I. Shrestha, T. E. Cowan, B. Jones, C. A. Coverdale, C. Deeney, and P. D. LePell, "Investigation of regimes of wire array implosion on the 1 MA Zebra accelerator", Physics of Plasmas **13**, 012704 (2006)

[Ivanov2006c] V. V. Ivanov, V.I. Sotnikov, G.S. Sarkisov, T.E. Cowan, S.N. Bland, B. Jones, C.A. Coverdale, C. Deeney, P.J. Laca, A.L. Astanovitskiy, and A. Haboub,

"Dynamics of Mass Transport and Magnetic Fields in Low-Wire-Number-Array Z Pinches", Physical Review Letters **97**, 125001 (2006)

[Ivanov2007a] V.V. Ivanov, V.I. Sotnikov, G.S. Sarkisov, A.L. Astanovitskiy, P.J. Laca, T.E. Cowan, B. Jones, C. Deeney, B.V. Oliver, T.A. Mehlhorn, and J.G. Leboeuf, "Experimental study of the dynamics of large- and small-scale structures in the plasma column of wire array z-pinches", IEEE Transactions on Plasma Science **35**, 1170 (2007)

[Ivanov2007b] V. V. Ivanov, V. I. Sotnikov, A. Haboub, G. E. Sarkisov, R. Presura, and T. E. Cowan, "Investigation of ablation and implosion dynamics in linear wire arrays", Physics of Plasmas **14**, 032703 (2007)

[Ivanov2008a] V.V. Ivanov, V. I. Sotnikov, A. Haboub, A. P. Shevelko, A. L. Astanovitskiy, A. Morozov, E. D. Kazakov, and S. D. Altemara, "Mitigation of the Plasma-Implosion Inhomogeneity in Starlike Wire-Array Z Pinches", Physical Review Letters **100**, 025004 (2008)

[Ivanov2009] V. V Ivanov, V. I. Sotnikov, J. M. Kindel, P. Hakel, R. C. Mancini, A. L. Astanovitskiy, A. Haboub, S. D. Altemara, A. P. Shevelko, E. D. Kazakov, and P. V. Sasorov, "Implosion dynamics and x-ray generation in small-diameter wire-array Z pinches", Physical Review E **79**, 056404 (2009)

[Ivanov2010a] V. V. Ivanov, A. L. Astanovitskiy, D. Papp, J. P. Chittenden, S. N. Bland, B. Jones, and S. D. Altemara, "Study of transparent and nontransparent regimes of implosion in star wire arrays", Physics of Plasmas **17**, 102702 (2010)

[Ivanov2010b] V. V. Ivanov, S. D. Altemara, A. A. Astanovitskiy, G. S. Sarkisov, A. Haboub, D. Papp, and J. M. Kindel, "Development of UV laser probing diagnostics for 1-MA z-pinches", IEEE Transactions on Plasma Science **38**, 574 (2010)

[Ivanov2011a] V. V. Ivanov, P. Hakel, R. C. Mancini,1 J. P. Chittenden, A. A. Anderson, T. Durmaz, P. Wiewior, D. Papp, S. D. Altemara, A. L. Astanovitskiy, and O. Chalyy, "Measurement of the Ionization State and Electron Temperature of Plasma during the Ablation", Physical Review Letters **106**, 225005 (2011)

[Ivanov2011b]. V. Ivanov, J. P. Chittenden, S. D. Altemara, N. Niasse, P. Hakel, R. C. Mancini, D. Papp, and A. A. Anderson, "Study of the Internal Structure and Small-Scale Instabilities in the Dense Z Pinch", V Physical Review Letters **107**, 165002 (2011)

[Jackson1999] J. D. Jackson, Classical Electrodynamics, 3rd. ed. (John Wiley and Sons, Inc., Hoboken, NJ, 1999), p. 321

[Johnston1973] T. W. Johnston and J. M. Dawson, "Correct values for high-frequency power absorption by inverse bremsstrahlung in plasmas", Physics of Fluids, **16**, 722 (1973)

[Jones2005] B. Jones, C. Deeney, J. L. McKenney, C. J. Garasi, T. A. Mehlhorn, A. C. Robinson, S. E. Wunsch, S. N. Bland, S.V. Lebedev, J. P. Chittenden, S. C. Bott, D. J. Ampleford, J. B. A. Palmer, J. Rapley, G. N. Hall, and B.V. Oliver, "Study of Three-Dimensional Structure in Wire-Array Z Pinches by Controlled Seeding of axial modulations in wire radius", Physical Review Letters **95**, 225001 (2005)

[Jones2008] B. Jones, C. A. Coverdale, C. Deeney, D. B. Sinars, E. M. Waisman, M. E. Cuneo, D. J. Ampleford, P. D. LePell, K. R. Cochrane, J. W. Thornhill, J. P. Apruzese, A. Dasgupta, K. G. Whitney, R. W. Clark, and J. P. Chittenden, "Implosion dynamics and K-shell x-ray generation in large diameter stainless steel wire array Z pinches with various nesting configurations", Physics of Plasmas **15**, 122703 (2008)

[Kalantar1993] D. H. Kalantar and D. A. Hammer, "Observation of a Stable Dense Core within an Unstable Coronal Plasma in Wire Initiated Dense Z-Pinch Experiments", Physical Review Letters **71**, 3806 (1993)

[Kantsyrev2006] V. V. Kantsyrev, A. S. Safranova, D. A. Fedin, V. V. Ivanov, A. A. Esaulov, V. Nalajala, I. Shrestha, S. Pokala, K. Williamson, N. D. Ouart, M. F. Yilmaz, P. Laca, T. E. Cowan, L. I. Rudakov, B. Jones, C. A. Coverdale, C. Deeney, P. D. LePell, A. L. Velikovich, and A. S. Chuvatin, "Radiation properties and implosion dynamics of planar and cylindrical wire arrays, assymetric and symmetric, uniform and combined X-pinches on the UNR 1-MA Zebra Generator", IEEE Transactions on Plasma Science **34**, 194 (2006)

[Kantsyrev2008] V. L. Kantsyrev, L. I. Rudakov, A. S. Safronova, A. A. Esaulov, A. S. Chuvatin, C. A. Coverdale, C. Deeney, K. M. Williamson, M. F. Yilmaz, I. Shrestha, N. D. Ouart, and G. C. Osborne, "Double planar wire array as a compact plasma radiation source", Physics of Plasmas **15**, 030704 (2008)

[Kantsyrev2009] V. L. Kantsyrev, A. S. Safronova, A. A. Esaulov, K. M. Williamson, I. Shrestha, M. F. Yilmaz, G. C. Osborne, M. E. Weller, N. D. Ouart, V. V. Shlyaptseva, L. I. Rudakov, A. S. Chuvatin, and A. L. Velikovich, "A review of new wire arrays with open and closed magnetic configurations at the 1.6 MA Zebra generator for radiative properties and opacity effects", High Energy Density Physics **5**, 115 (2009)

[Katzenstein1981] J. Katzenstein, "Optimum coupling of imploding loads to pulse generators", Journal of Applied Physics **52**, 676 (1981)

[Knapp2010] P. F. Knapp, J. B. Greenly, P.-A. Gourdain, C. L. Hoyt, M. R. Martin, S. A. Pikuz, C. E. Seyler, T. A. Shelkovenko, and D. A. Hammer, "Growth and saturation of the axial instability in low wire number wire array Z pinches", Physics of Plasmas **17**, 012704 (2010)

[Lebedev1998a] S. V. Lebedev, I. H. Mitchell, R. Aliaga-Rossel, S. N. Bland, J. P. Chittenden, A. E. Dangor, and M. G. Haines, "Azimuthal Structure and Global Instability in the Implosion Phase", Physical Review Letters **81**, 4152 (1998)

[Lebedev2000a] S.V. Lebedev, F. N. Beg, S. N. Bland, J. P. Chittenden, A. E. Dangor, M.G. Haines, S. A. Pikuz, and T. A. Shelkovenko, "Effect of Core-Corona Plasma Structure on Seeding of Instabilities in Wire Array Z Pinches", Physical Review Letters **85**, 98 (2000)

[Lebedev2000b] S. V. Lebedev, R. Aliaga-Rossel, S. N. Bland, J. P. Chittenden, A. E. Dangor, M. G. Haines, and M. Zakaullah, "Two Different Modes of Nested Wire Array Z-Pinch Implosions", Physical Review Letters **84**, 1708 (2000)

[Lebedev2001a] S. V. Lebedev, F. N. Beg, S. N. Bland, J. P. Chittenden, A. E. Dangor, M. G. Haines, K. H. Kwek, S. A. Pikuz, and T. A. Shelkovenko, "Effect of discrete wires on the implosion dynamics of wire array Z pinches", Physics of Plasmas **8**, 3734 (2001)

[Lebedev2001b] S. V. Lebedev, F. N. Beg, S. N. Bland, J. P. Chittenden, A. E. Dangor, M. G. Haines, S. A. Pikuz, and T. A. Shelkovenko, "Plasma formation and the implosion phase of wire array z-pinch experiments", Laser and Particle Beams **19**, 355 (2001)

[Lebedev2001c] J. P. Chittenden, S. V. Lebedev, S. N. Bland, A. Ciardi, and M. G. Haines, "The different dynamical modes of nested wire array Z pinches", Physics of Plasmas **8**, 675 (2001)

[Lebedev2002] S. V. Lebedev, F. N. Beg, S. N. Bland, J. P. Chittenden, A. E. Dangor, and M. G. Haines, "Snowplow-like behavior in the implosion phase of wire array Z pinches", Physics of Plasmas **9**, 2293 (2002)

[Lebedev2005a] S. V. Lebedev, A. Ciardi, D. J. Ampleford, S. N. Bland, S. C. Bott, J. P. Chittenden, G. N. Hall, J. Rapley, C. A. Jennings, A. Frank, E. G. Blackman, and T. Lery, "Magnetic tower outflows from a radial wire array Z-pinch", Monthly Notices of the Royal Astronomical Society, **361**, 97 (2005)

[Lebedev2005b] S. V. Lebedev, D. J. Ampleford, S. N. Bland, S. C. Bott, J. P. Chittenden, J. Goyer, C. Jennings, M. G. Haines, G. N. Hall, D. A. Hammer, J. B. A. Palmer, S. A. Pikuz, T. A. Shelkovenko, and T. Christoudias, "Physics of wire array Z-pinch implosions: experiments at Imperial College", Plasma Physics and Controlled Fusion **47**, A91 (2005)

[Lemke2009] R.W. Lemke, D. B. Sinars, E. M. Waisman, M. E. Cuneo, E. P. Yu, T.A. Haill, H. L. Hanshaw, T. A. Brunner, C. A. Jennings, W. A. Stygar, M. P. Desjarlais, T. A. Mehlhorn, and J. L. Porter, "Effects of Mass Ablation on the Scaling of X-Ray Power with Current inWire-Array Z Pinches", Physical Review Letters **102**, p. 025005 (2009)

[Liberman1999] M. A. Liberman, J. S. De Groot, A. Toor, and R. B. Spielman, Physics of High-Density Z-pinch Plasma (Springer, New York, NY, 1999)

[Lovberg1993] R. H. Lovberg, R. A. Riley, and J. S. Shlachter, "Instability Heating of the HDZP", AIP Conference Proceedings **299**, 59 (1993)

[Marshall2006] F. J. Marshall,J. P. Knauer, D. Anderson, and B. L. Schmitt, "Absolute calibration of Kodak Biomax-MS film response to x-rays in the 1.5- to 8-keV energy range", Review of Scientific Instruments **77**, 10F308 (2006)

[Martinez2010a] D. Martinez, R. Presura, S. Stein, C. Plechaty, and S. Neff, "Reduction of instabilities in wire arrays Z-pinches", High Energy Density Physics **6**, 237 (2010)

[Martinez2010b] D. Martinez, "Experimental investigation of sheared flow stabilization of z-pinches", PhD Thesis, University of Nevada, Reno, Reno, NV, 2011.

[Papp2012] D. Papp, V. V. Ivanov, B. Jones, A. Haboub, A.A. Anderson, S. D. Altemara, and B.R. Talbot, "Study of the precursor and non-precursor implosion regimes in wire array Z-pinches", Physics of Plasmas **19**, 092704 (2012)

[Pease1957] R. S. Pease, “Equilibrium Characteristics of a Pinched Gas Discharge Cooled by Bremsstrahlung Radiation”, Proceedings of the Physical Society B **70**, 11 (1957)

[Pikuz1999] S. A. Pikuz, T. A. Shelkovenko, D. B. Sinars, J. B. Greenly, Y. S. Dimant, and D. A. Hammer, ”Multiphase Foamlike Structure of Exploding Wire Cores”, Physical Review Letters **83**, 4313 (1999)

[Pikuz2004] S. A. Pikuz, T. A. Shelkovenko, K. M. Chandler, M. D. Mitchell, D. A. Hammer, I. Y. Skobelev, A. S. Shlyaptseva, and S. B. Hansen, “X-ray spectroscopy for high energy-density X pinch density and temperature measurements”, Review of Scientific Instruments **75**, 3666 (2004)

[Price1995] D. F. Price, R. M. More, G. Guethlein, R. I. Shepherd, R. E. Stewart, and W. E. White, “Absorption of Ultrashort Laser Pulses by Solid Targets Heated Rapidly to Temperatures 1—1000 eV”, Physical Review Letters **75**, 252 (1995)

[Ryutov2000] D. D. Ryutov, M. S. Derzon, and M. K. Matzen, “The physics of fast Z pinches”, Reviews of Modern Physics **72**, 167 (2000)

[Sanford1996] T. W. L. Sanford, G. O. Allshouse, B. M. Marder, T. J. Nash, R. C. Mock, R. B. Spielman, J. F. Seamen, J. S. McGurn, D. Jobe, T. L. Gilliland, M. Vargas, K. W. Struve, W. A. Stygar, M. R. Douglas, and M. K. Matzen, “Improved Symmetry Greatly Increases X-Ray Power from Wire-Array Z-Pinches”, Physical Review Letters **77**, 5063 (1996)

[Sanford2007] T. W. L. Sanford, C. A. Jennings, G. A. Rochau, S. E. Rosenthal, G. S. Sarkisov, P. V. Sasorov, W. A. Stygar, L. F. Bennett, D. E. Bliss, J. P. Chittenden, M. E. Cuneo, M. G. Haines, R. J. Leeper, R. C. Mock, T. J. Nash, and D. L. Peterson, “Demonstrated transparent mode in nested wire arrays used for dynamic hohlraum Z pinches”, Physics of Plasmas **14**, 052703 (2007)

[Sarkisov1996] G. S. Sarkisov, “Shearing interferometer with an air wedge for the electron density diagnostics in a dense plasma”, Instruments and Experimental Techniques **39**, 727 (1996)

[Sarkisov2007] G. S. Sarkisov, S. E. Rosenthal, K.W. Struve, T. E. Cowan, T. Presura, A. L. Astanovitskiy, A. Haboub, and A. Morozov, “Initiation of aluminum wire array on the 1-MA ZEBRA accelerator and its effect on ablation dynamics and x-ray yield”, Physics of Plasmas **14**, 112701 (2007)

[Sawada2012] H. Sawada, Personal communication, 2012 October

[Schlachter1990] J. S. Shlachter, “Solid D2 Fiber experiments on HDZP-II”, Plasma Physics and Controlled Fusion **32**, 1073 (1990)

[Shelkovenko2002] T. A. Shelkovenko, S. A. Pikuz, D. B. Sinars, K. M. Chandler, and D. A. Hammer, Physics of Plasmas, “Time-resolved spectroscopic measurements of ~1 keV, dense, subnanosecond X-pinch plasma bright spots”, **9**, 2165 (2002)

[Shelkovenko2007] T. A. Shelkovenko, S. A. Pikuz, J. D. Douglass, I. C. Blesener, J. B. Greenly, R. D. McBride, D. A. Hammer, and B. R. Kusse, “Wire core and coronal

plasma expansion in wire-array Z pinches with small numbers of wires", Physics of Plasmas **14**, 102702 (2007)

[Shevelko2002] A. P. Shevelko, Yu. S. Kasyanov, O. F. Yakushev, and L. V. Knight, "Compact focusing von Hamos spectrometer for quantitative x-ray spectroscopy", Review of Scientific Instruments **73**, 3458 (2002)

[Sinars2006] D. B. Sinars, M. E. Cuneo, E. P. Yu, S. V. Lebedev, K. R. Cochrane, B. Jones,J. J. MacFarlane, T. A. Mehlhorn, J. L. Porter, and D. F. Wenger, "Measurements and simulations of the ablation stage of wire arrays with different initial wire sizes", Physics of Plasmas **13**, 042704 (2006)

[Slutz2010] S. A. Slutz, M. C. Herrmann, R. A. Vesey, A. B. Sefkow, D. B. Sinars, D. C. Rovang, K. J. Peterson, and M. E. Cuneo, "Pulsed-power-driven cylindrical liner implosions of laser preheated fuel", Physics of Plasmas, **17**, 056303 (2010)

[Sotnikov2002] V. I. Sotnikov, I. Paraschiv, V. Makhin, B. S. Bauer, J. N. Leboeuf, and J. M. Dawson, "Linear analysis of sheared flow stabilization of global magnetohydrodynamic instabilities based on the Hall fluid model", Physics of Plasmas **9**, 913 (2002)

[Spielman1988] R. B. Spielman, W. W. Hsing, D. L. Hanson, "Photoconducting x-ray detectors for z-pinch experiments", Review of Scientific Instruments **59**, 1804 (1988)

[Spielman1992] R. B. Spielman, "A five-channel, diamond photoconducting x-ray detector array for z-pinch experiments", Review of Scientific Instruments **63**, 5058 (1992)

[Spielman1995] R. B. Spielman, "Diamond photoconducting detectors as high power z-pinch diagnostics",Review of Scientific Instruments **66**, p. 867 (1995)

[Stickler2005] T. Stickler, Y. Y. Lau, M. Gilgenbach, M. Cuneo, and T. A. Mehlhorn, "Azimuthal clumping instabilities in a Z-pinch wire array", Physics of Plasmas, **12**, 052701 (2005)

[Swartz1971] M. Swartz, S. Kastner, E. Rothie, and W. Neupert, "Soft x-ray spectra of Cr, Mn, Fe, Co, Ni, Cu; classifications in Ne I, F I, 0 I, N I, and C I isoelectronic sequences", Journal of Physics B **4**, 1747 (1971)

[Velikovich1995] A. L. Velikovich and J. Davis, "Implosions, equilibria, and stability of rotating, radiating Z pinch plasmas", Physics of Plasmas **2**, 4513 (1995)

[Velikovich1996] A. L. Velikovich, F. L. Cochran, and J. Davis, "Suppression of Rayleigh-Taylor Instability in Z-Pinch Loads with Tailored Density Profiles", Physical Review Letters, **77**, 853 (1996)

[Velikovich2000] A. L. Velikovich, J. Davis, J. W. Thornhill, J. L. Giuliani Jr., L. I. Rudakov, and C. Deeney, "Model of enhanced energy deposition in a Z-pinch plasma", Physics of Plasmas **7**, p. 3265 (2000)

[Velikovich2002] A. L. Velikovich, I. V. Sokolov, and A. A. Esaulov, "Perfectly conducting incompressible fluid model of a wire array implosion", Physics of Plasmas **9**, 1366 (2002)

[Wiewior2010] P. P. Wiewior, V. V. Ivanov, and O. Chalyy, "Development of the 50 TW laser for joint experiments with 1MA z-pinches", Journal of Physics: Conference Series **244**, 032013 (2010)

[Weller2012] M.E. Weller, A.S. Safronova, V.L. Kantsyrev, A.A. Esaulov, C.A. Coverdale, A.S. Chuvatin, N.D. Ouart, K.M. Williamson, I. Shrestha, G.C. Osborne, V.V. Shlyaptseva, S.F. Keim and A. Stafford, "Radiative properties of mixed nested cylindrical wire arrays on Zebra at UNR", High Energy Density Physics **8**, 184 (2012)

[Williamson2009] K. M. Williamson, V. L. Kantsyrev, A. A. Esaulov, A. S. Safronova, N. D. Ouart, F. M. Yilmaz, I. K. Shrestha, V. Shlyaptseva, R. D. McBride, D. A. Chalenski, J. D. Douglass, J. B. Greenly, D. A. Hammer, and B. R. Kusse, "Ablation dominated implosion dynamics of aluminum and stainless steel nested cylindrical wire arrays", Physics of Plasmas **16**, 012704 (2009)

[Yu2007] E. P. Yu, B. V. Oliver, D. B. Sinars, T. A. Mehlhorn, M. E. Cuneo, P. V. Sasorov, M. G. Haines, and S. V. Lebedev, "Steady-state radiation ablation in the wire-array Z pinch", Physics of Plasmas **14**, 022705 (2007)

[Zier2009] J. C. Zier, J. D. Douglass, I. C. Blesener, K. S. Blesener, D. A. Chalenski, R. M. Gilgenbach, J. B. Greenly, D. A. Hammer, P. F. Knapp, B. R. Kusse, Y. Y. Lau, R. D. McBride, W. Syed, and E. P. Yu, "Azimuthally correlated ablation between *z*-pinch wire cores", Physics of Plasmas **16**, 102702 (2009)